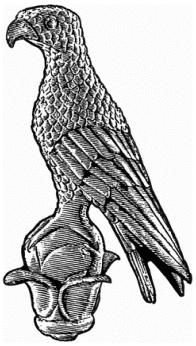

SCHOOL OF SCIENCES

DEPARTMENT OF PHYSICS

UNIVERSITY OF IOANNINA

DEVELOPMENT OF HIGH CONDUCTION BAND PHOTOACTIVE NANOSTRUCTURES, INTERFACED WITH SINGLE ATOMS

CHRISTOS SIDIROPOULOS

SUPERVISOR: PROFESSOR YIANNIS DELIGIANNAKIS

MASTER'S THESIS

IOANNINA 2023

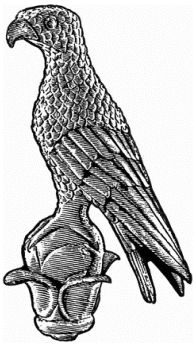

ΣΧΟΛΗ ΘΕΤΙΚΩΝ ΕΠΙΣΤΗΜΩΝ

ΤΜΗΜΑ ΦΥΣΙΚΗΣ

ΠΑΝΕΠΙΣΤΗΜΙΟ ΙΩΑΝΝΙΝΩΝ

ΑΝΑΠΤΥΞΗ ΦΩΤΟΕΝΕΡΓΩΝ ΝΑΝΟΔΟΜΩΝ ΜΕ ΥΨΗΛΗ ΖΩΝΗ ΑΓΩΓΙΜΟΤΗΤΑΣ, ΣΥΖΕΥΓΜΕΝΕΣ ΜΕ ΜΟΝΑΔΙΑΙΑ ΑΤΟΜΑ

ΧΡΗΣΤΟΣ ΣΙΔΗΡΟΠΟΥΛΟΣ

ΕΠΙΒΛΕΠΩΝ: ΚΑΘΗΓΗΤΗΣ ΙΩΑΝΝΗΣ ΔΕΛΗΓΙΑΝΝΑΚΗΣ

ΜΕΤΑΠΤΥΧΙΑΚΟ ΔΙΠΛΩΜΑ ΕΙΔΙΚΕΥΣΗΣ

ΙΩΑΝΝΙΝΑ 2023

Acknowledgments

I am deeply grateful to **Professor Yiannis Deligiannakis** for his continuous scientific and moral support throughout my thesis. Through his supervision and numerous stimulating discussions, he opened for me the door to professionalism and high-quality research. His tireless passion and his deep knowledge became a motivating force for me to love even more the scientific research and I will always be grateful for this. I would also like to express my gratitude to the other two members of my 3-member advisor committee, **Professor Alexios Douvalis** and **Associate Professor Athanasios Bourlinos**, for their interest in my work and access to their laboratory.

I feel much appreciation towards **Professor Georgios Evangelakis**, for his kind provision to operate the X-ray Photoelectron Spectroscopy equipment installed in his laboratory. I would like, also, to thank **Dr. Constantinos Moularas** for his contribution to the experimental process.

This work was carried out at the Laboratory of Physical Chemistry of Materials and Environment at the University of Ioannina, and I would like to thank all of its members and all the members of the Lab of Biomimetic Catalysis and Hybrid Materials and its Head **Professor Maria Louloudi,** for creating such a nice atmosphere to work in, as well as for many fruitful discussions. Special thanks to **Ph.D. candidate Loukas Belles** who, from day one, helped me familiarize myself with the multitude of techniques applied in the laboratory. I especially thank him for his interest in my work and his provision of scientific support in electrochemistry. Many thanks go to **Ph.D. candidate Areti-Konstantina Zindrou** for the knowledge she provided me about copper-based materials.

I would like to thank **Ph.D. candidate Pavlos Psathas** for his great contribution to the synthesis of the perovskite structures, but also during the experimental process of the photocatalytic measurements. Many thanks to **Ph.D. candidate Christos Dimitriou** and **Master's student Sokratis Soutzios** for their help in technical parts and during my integration in the laboratory.

Finally, this work would not have been accomplished without the support of my parents, **Theodoros** and **Anastasia**, and their unconditional love and support for every step that I make. Their sacrifices have made my dreams possible to be chased, and for this, they will always be a crucial part of my life.

Abstract

In this Master Thesis, we have developed high-conduction band photoactive nanostructures, interfaced with single atoms. Through Flame Spray Pyrolysis (FSP) technology we have synthesized, in a one-step process, sodium tantalate ($NaTaO_3$) perovskite structures with a high degree of crystallinity, and high Specific Surface Area (SSA). Furthermore, these flame-made nanoparticles were in-situ interfaced with Copper (Cu) single atoms, using a novel deposition method and thus, resulting in the enhancement of the hydrogen production yield via the water-splitting reaction.

The crystal phase composition and nanoparticles' size of the flame-made materials were evaluated by powder X-Ray Diffraction (pXRD). X-Ray Photoelectron Spectroscopy (XPS) was used to study the surface chemical compositions and states of the samples. The pore analysis and the evaluation of the specific surface area were carried out by the Nitrogen Adsorption-Desorption method (B.E.T analysis). The vibrational modes of $Ta-O$ were determined via Raman spectroscopy. UV-Vis Diffuse Reflectance Spectroscopy (DRS) was used to estimate the band gap energy (E_g) and investigate the optical properties of the semiconductors. The electronic properties of the materials were investigated by Electron Paramagnetic Resonance (EPR). EPR, also, provided detailed structural information, e.g., the coordination environment of Cu atoms, and the estimation of the $Cu-Cu$ distance. Nanoparticles were deposited as drop-casted films by spin-coating method on FTO substrates and their conductivity was investigated by Electrochemical Impedance Spectroscopy (EIS) versus different environments, which can indicate their performance in some electrocatalytic reactions.

Among the key results are: [1] The development of high conduction band photoactive ($NaTaO_3$) nanostructures, interfaced with Cu single atoms in a single step using FSP. [2] The nanoparticles' high crystallinity and surface area values. [3] The successful single atom deposition validation using EPR spectra. [4] The mechanism that correlates single atoms with enhanced photocatalytic performance. [5] The high conductivity and electrocatalytic activity of single atom deposited $NaTaO_3$ nanoparticles via Electrochemical Impedance Spectroscopy.

Περίληψη

Στην παρούσα Μεταπτυχιακή Διπλωματική Εργασία αναπτύξαμε φωτοενεργές νανοδομές με υψηλή ζώνης αγωγιμότητας, συζευγμένες με μοναδιαία άτομα. Μέσω της τεχνολογίας Πυρόλυσης Ψεκασμού Φλόγας (FSP) έχουμε συνθέσει σε διαδικασία ενός βήματος περοβσκιτικές δομές ($NaTaO_3$) με υψηλό βαθμό κρυσταλλικότητας και υψηλή τιμή ειδικής επιφάνειας (SSA). Επιπλέον, τα παραχθέντα νανοσωματίδια συζεύχθηκαν επί τόπου με μοναδιαία άτομα χαλκού (Cu), χρησιμοποιώντας μια νέα μέθοδο εναπόθεσης, με αποτέλεσμα την ενίσχυση της απόδοσης παραγωγής υδρογόνου μέσω της αντίδρασης διάσπασης του νερού.

Η αναγνώριση της κρυσταλλικής φάσης και του μεγέθους των νανοσωματιδίων που παράγονται από φλόγα αξιολογήθηκε μέσω της Περίθλασης Ακτίνων Χ σκόνης (pXRD). Η Φασματοσκοπία Φωτοηλεκτρονίων Ακτίνων Χ (XPS) χρησιμοποιήθηκε για τη μελέτη των επιφανειακών χημικών συνθέσεων και καταστάσεων των δειγμάτων. Η ανάλυση πόρων και η αξιολόγηση της ειδικής επιφάνειας πραγματοποιήθηκε με τη μέθοδο προσρόφησης-εκρόφησης αζώτου (ανάλυση B.E.T). Οι δονητικοί τρόποι ταλάντωσης του δεσμού $Ta-O$ προσδιορίστηκαν μέσω φασματοσκοπίας Raman. Η φασματοσκοπία διάχυτης ανάκλασης UV-Vis (DRS) χρησιμοποιήθηκε προκειμένου να υπολογιστεί το ενεργειακό χάσμα (E_g) και να διερευνηθούν οι οπτικές ιδιότητες των νανοδομών. Οι ηλεκτρονιακές ιδιότητες των υλικών διερευνήθηκαν μέσω της φασματοσκοπίας Ηλεκτρονιακού Παραμαγνητικού Συντονισμού (EPR). Μέσω του EPR, επίσης, παρήχθη λεπτομερείς δομικές πληροφορίες, όπως το περιβάλλον αλληλεπίδρασης των ατόμων Cu και έγινε εκτίμηση της απόστασης $Cu-Cu$. Κατασκευάστηκαν, επίσης, λεπτά υμένια με μέθοδο επικάλυψης σπιν από νανοσωματίδια σε υποστρώματα FTO και η αγωγιμότητά τους διερευνήθηκε μέσω της Φασματοσκοπίας Ηλεκτροχημικής Εμπέδησης (EIS) έναντι διαφορετικών περιβαλλόντων, που μπορεί να υποδείξει την απόδοσή τους σε ορισμένες ηλεκτροκαταλυτικές αντιδράσεις.

Μεταξύ των βασικών αποτελεσμάτων είναι: [1] Η ανάπτυξη φωτοενεργών νανοδομών υψηλής ζώνης αγωγιμότητας ($NaTaO_3$), συζευγμένες με μοναδιαία άτομα Cu σε ένα βήμα χρησιμοποιώντας την τεχνολογία FSP. [2] Η υψηλή κρυσταλλικότητα και ειδική επιφάνεια των νανοσωματιδίων. [3] Η επιτυχής επικύρωση εναπόθεσης μεμονωμένων ατόμων χρησιμοποιώντας την φασματοσκοπία EPR. [4] Η βελτιωμένη φωτοκαταλυτική απόδοση των νανοσωματιδίων. [5] Η υψηλή αγωγιμότητα και ηλεκτροκαταλυτική δραστικότητα των νανοδομών μέσω της Φασματοσκοπίας Ηλεκτροχημικής Εμπέδησης

Chapter 1

Introduction

1.1 Historical Elements of Nanotechnology

Nanotechnology refers to the science and engineering of materials at the nanoscale level. The concept of nanotechnology started with a seminar lecture entitled ‘‘There's Plenty of Room at the Bottom’’ given by physicist Richard Feynman at a conference in 1959. He discussed the possibility of manipulating and controlling matter at the atomic and molecular scale [1,2]. This lecture is considered the birth of nanotechnology. Though Feynman's work was theoretical, it set the stage for the eventual development of nanotechnology.

The formal emergence of nanotechnology as a field, however, dates back to the 1980s. During this time, researchers began to develop more advanced tools and techniques for manipulating materials at the nanoscale level, such as scanning probe microscopes, which were able to image individual atoms [3–6]. This allowed for the exploration of nanotechnology to accelerate and led to discoveries in physics, chemistry, and engineering.

Since then, nanotechnology has had a profound impact on our daily lives. One of the most well-known examples of the use of nanotechnology is in electronics [7–10]. Silicon chips [11–13], the backbone of our digital devices, are composed of transistors that are only a few nanometers in size. This allows for a greater number of transistors to be packed onto a single chip, increasing processing power and storage capacity.

Nanotechnology has also revolutionized the fields of medicine [14–18], energy storage [19–22], optical engineering [23–25], communications [26–29], biomedical, and drug delivery [30–34]. Nanomaterials such as liposomes and dendrimers are increasingly used to deliver drugs to specific parts of the body, allowing for precise targeting and greater effectiveness.

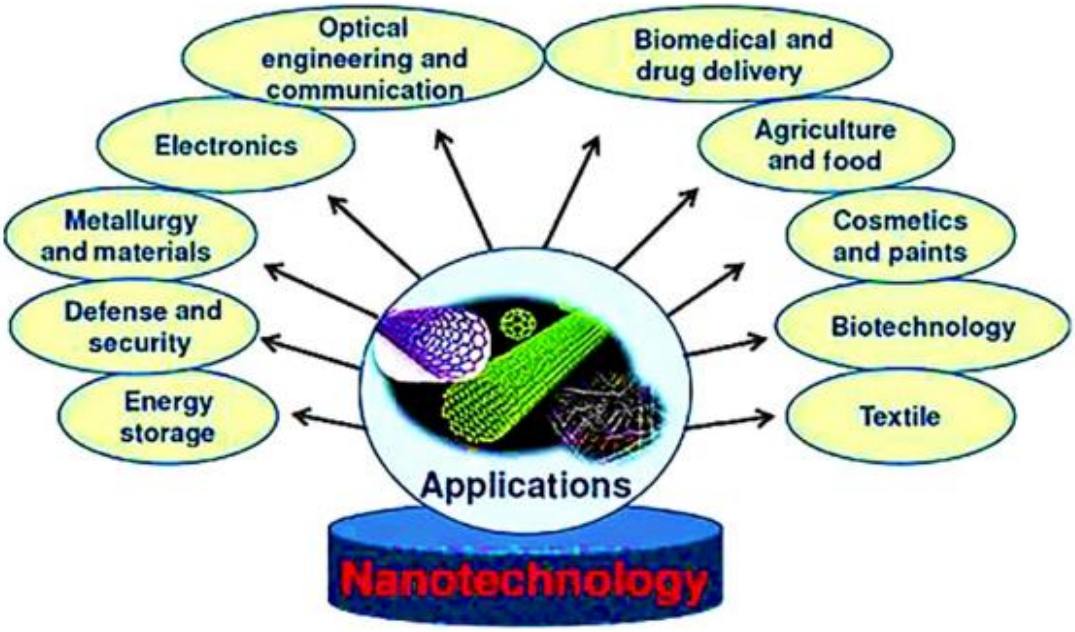

Figure 1.1: Applications of nanotechnology in daily life [39].

The development of nanotechnology has been a tale of rapidly advancing technology. From theoretical concepts to the ability to directly manipulate materials at the atomic and molecular level, the field has grown and developed at an incredible pace. With its ability to revolutionize electronics, medicine, and many other fields, nanotechnology is sure to continue to shape our lives in the years to come.

Nanomaterials are characterized as those that have at least one dimension in the nanometer range, typically between 1 and 100 nanometers. These materials exhibit unique physical, chemical, and biological properties that are different from their bulk counterparts, making them attractive for a wide range of applications.

In the 1980s, the invention of the Scanning Tunneling Microscope (STM) by Gerd Binnig and Heinrich Rohrer allowed scientists to visualize and manipulate individual atoms and molecules for the first time. This breakthrough led to the development of new nanomaterials, such as fullerenes [35–37], nanotubes [38–41], and quantum dots [42,43]. Since then, the field of nanomaterials has grown rapidly, with new materials and applications being discovered and developed every day. However, there are also concerns about the potential risks associated with these materials, such as toxicity and environmental impact.

1.2 Perovskites

1.2.1 Overview of Perovskites

Perovskites are a class of materials that have a unique crystal structure resembling that of the mineral perovskite $CaTiO_3$ [44]. This structure has a general formula of ABX_3, where A and B are cations and X is an anion. This complex structure allows a wide range of chemical compositions as *most elements of nature* can be found in such structures. Perovskites have become the focus of intense research due to their unique and tunable properties, including excellent physicochemical, photovoltaic, and optoelectronic properties, high mobility, low defect formation energies, and high selectivity and reactivity towards some gases. These properties make perovskites promising candidates for a range of applications, including solar cells, LEDs, sensors, and catalysts [45–47].

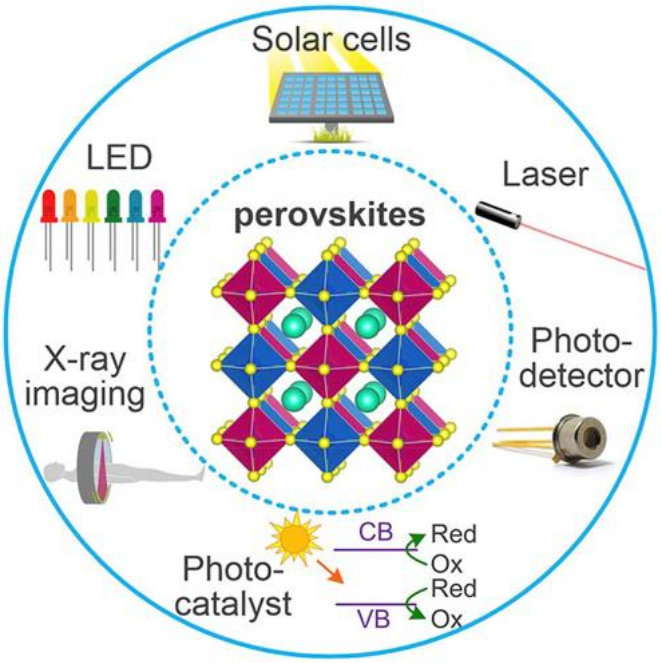

Figure 1.2: Current and potential applications of perovskites, including solar cells, lasers, photodetectors, photocatalysis, X-ray imaging, and LEDs [46].

1.2.2 Requirements for Perovskites

Of great importance for perovskite materials is the requirement to be highly pure, which is critical for both fundamental studies and practical applications. *High-purity perovskite structures* are necessary to achieve consistent and reproducible properties across different samples. Another important requirement is the *control of stoichiometry* [48], as variation in chemical composition can greatly affect the physical properties of perovskites [49–51]. Additionally, *high crystallinity* is needed to ensure good carrier transport properties and minimize defects [52–54].

Another key requirement for perovskite materials is the ability to process them into thin films [55,56]. Thin films are important for device applications and require materials with good solubility and easy, inexpensive processing techniques. The use of solution-based methods, such as spin coating, and inkjet printing, has allowed for the fabrication of thin films with high quality, control, and homogeneity [57].

1.2.3 Physical Properties of Perovskites

Perovskites exhibit a range of desirable physical and chemical properties that are important for various applications. One of the most notable properties is their *high efficiency in solar cell devices* [58,59], which is attributed to their high absorption coefficients and long carrier lifetimes. Moreover, perovskites exhibit exceptional *optoelectronic properties* [60,61], including high mobility, low recombination rates, and high photoconductivity, which make them highly desirable for use in optoelectronics devices such as LEDs and photodetectors. Furthermore, perovskites also have *high dielectric constants* [62,63], *strong piezoelectricity* [64], and are *ferroelectric* [65], making them promising for use in sensors and actuators. In combination with their easy processability, perovskites hold great potential for a range of applications in the fields of electronics and energy.

1.2.4 The $NaTaO_3$ perovskite structure

Sodium tantalate ($NaTaO_3$) is a member of the perovskite oxide family of materials that have a general formula of ABO_3, where A and B are metal cations and X is an anion. Sodium tantalates exhibit unique properties and have promising applications in various fields such as *photocatalysis* [66,67], *photoluminescence* [68], and *dielectric spectroscopy* [69,70]. These compounds have garnered significant research interest due to their remarkable stability, optical properties, and catalytic activity. $NaTaO_3$ has a perovskite-type crystal structure, which is characterized by a cubic unit cell with lattice constants of approximately 3.9 Å. The crystal structure of $NaTaO_3$ can be described as a network of TaO_6 octahedra sharing corners and edges, with a sodium ion located in a large cavity at the center of the octahedra.

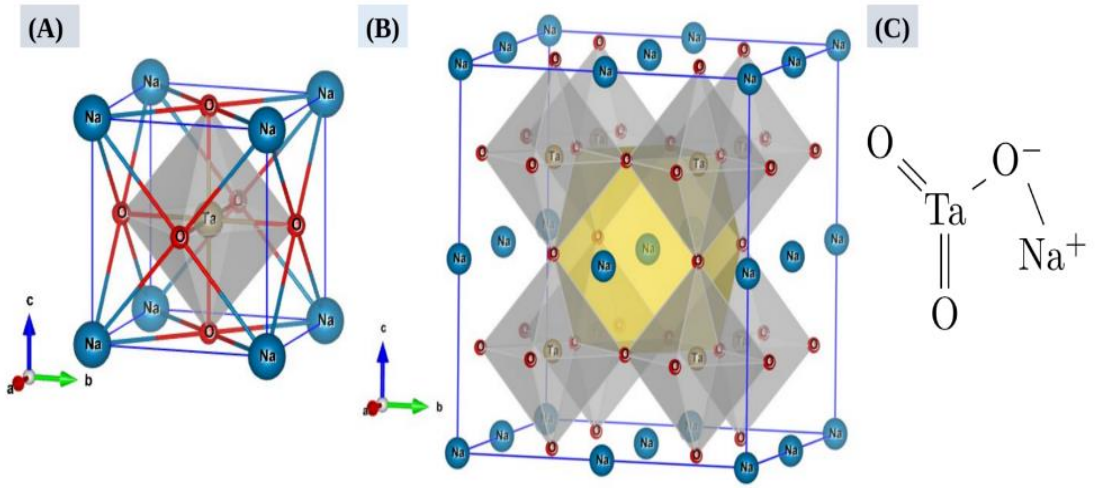

Figure 1.3: Perovskite crystal structure of $NaTaO_3$. (A) a 3D framework of corner sharing TaO_6 octahedra with Na^+ ions in the twelve-fold cavities in between the polyhedral (B), and its molecular structure (C) [80].

The crystal structure of $NaTaO_3$ has been extensively studied due to its unique and desirable properties. One of the most significant properties is its *high dielectric constant* [71], which is attributed to the polarizability of the $Ta-O$ bonds in the TaO_6 octahedra. In addition to its high dielectric constant ($\varepsilon' \sim 147$ at 25 °C, 1 kHz), $NaTaO_3$ also exhibits a *high degree of ferroelectricity*, which makes it promising for use in ferroelectric memory devices.

The crystal structure of $NaTaO_3$ also plays an important role in determining its electronic properties. The network of TaO_6 octahedra results in a band gap $(E_g \approx 4\ eV)$ that is dependent on the octahedral distortion. This has been heavily researched for the potential use of $NaTaO_3$ in various types of electronic devices, particularly in photocatalytic and photoelectrochemical applications.

Overall, the crystal structure of $NaTaO_3$ is crucial in determining its unique physical and electronic properties. Further exploration of its crystal structure and the effects of different synthetic methods on the structure can provide insight into potential applications in various fields, particularly in energy conversion and storage, where perovskites have shown great potential.

1.2.5 Synthesis Methods of Sodium Tantalates

The experimental techniques that sodium tantalate can be synthesized are a few, but none of them except one has achieved not only one-step synthesis but also the production of nanostructured particles. In each technique are highlighted the key advantages and challenges associated with it.

i) Solid-State Reaction Method

The solid-state reaction method [72,73] is one of the most widely used techniques for synthesizing sodium tantalates. Kudo et al [74,75] have contributed greatly to the production of sodium tantalates and searched extensively for their catalytic properties including heterojunctions of them with other metal oxides e.g. NiO or/and La [76,77]. The method involves thoroughly mixing the precursor powders, typically sodium carbonate (Na_2CO_3) and tantalum pentoxide (Ta_2O_5), followed by calcination at high temperatures (usually between 800 and 1200 ℃). The reaction process can be facilitated by employing a suitable flux or by optimizing the heating process. Although this method is relatively simple, it often results in inhomogeneous products and requires high reaction temperatures to achieve complete conversion. The products of this method are usually microscopic.

ii) Sol-Gel Method

The sol-gel method [78,79] is an effective and versatile technique for synthesizing sodium tantalates with controlled particle size and morphology. This method involves the hydrolysis and polycondensation of alkoxide precursors (e.g., tantalum ethoxide) in the presence of a sodium source, such as sodium hydroxide or sodium acetate. The resulting gel is then dried and calcined to obtain the desired $NaTaO_3$ product. The sol-gel method can produce highly homogeneous materials with well-dispersed particles and offers better control over the crystallinity and phase purity compared to solid-state reactions.

iii) Hydrothermal Synthesis

Hydrothermal synthesis [80,81] is a widely used method for the preparation of sodium tantalates under relatively milder conditions compared to the solid-state reaction method. This technique involves the reaction of sodium and tantalum precursors in a closed, high-pressure vessel filled with water or a suitable solvent. The hydrothermal process allows for precise control of particle size and morphology, and it can yield highly crystalline and pure $NaTaO_3$ products. However, the method can be time-consuming and requires specialized equipment for handling high pressures.

iv) Soft Chemical Methods

Soft chemical methods [82], such as co-precipitation and ion exchange, are attractive alternatives for synthesizing sodium tantalates due to their low-temperature requirements and environmentally friendly nature. In the co-precipitation method, a homogeneous solution containing sodium and tantalum precursors is mixed with a precipitating agent, leading to the formation of a solid precipitate. The precipitate is then washed, dried, and calcined to obtain the desired $NaTaO_3$ product. Ion-exchange methods involve the substitution of sodium ions with tantalum ions in a host material, followed by thermal treatment to form the sodium tantalate product.

v) Flame Spray Pyrolysis (FSP)

The latest advances and novel approaches in the synthesis of sodium tantalates come from this process route. Flame Spray Pyrolysis [83,84] is a versatile technique for the synthesis of highly homogenous and crystalline nanoparticles. In this process, sodium salt and tantalum precursors are atomized and introduced into the high-temperature flame that is maintained by a fuel and oxidizing agent mixture. Within the flame, the precursor droplets evaporate and react to form complex intermediates before pyrolytic decomposition and condensation into highly crystalline nanoparticles. The size and morphology of the nanoparticles can be controlled by adjusting the conditions of the flame, such as temperature, reactant concentration, and precursor selection. More about the FPS process is described in Chapter 2.

1.3 High Conduction Band Alkali Tantalates

1.3.1 The importance of high conduction band nanoparticles

Nanoparticles with high conduction band energy are vital in improving the efficiency of catalytic reactions. When used as catalysts, nanoparticles act as electron acceptors or donors [85], facilitating the conversion of chemical compounds. The conduction band energy of nanoparticles plays a crucial role in determining the rate of these reactions. High conduction band energy nanoparticles can accept electrons more easily, allowing a higher rate of electron transfer and therefore, increased efficiency in catalytic reactions.

One of the most significant benefits of using high-conduction band energy nanoparticles in catalysis is their ability to activate molecules that are typically difficult to react. For instance, the use of high-conduction band TiO_2 nanoparticles in the photodegradation of environmental pollutants such as dyes [86] has proven to be highly effective. The high conduction band energy helps to initiate the generation of reactive oxygen species, which are crucial in the degradation of pollutants.

Nanoparticles with high conduction band energy also exhibit excellent redox properties, which can be utilized in various catalytic applications. The redox properties of these nanoparticles can be attributed to their ability to accept or donate electrons during catalytic reactions. This property is of great importance in several catalytic reactions, such as Oxygen Reduction Reactions (ORR) [87–89], and Hydrogen Evolution Reactions (HER) [90,91] in fuel cells. Metal nanoparticles with high conduction band energy are commonly employed as catalysts in fuel cells, where they help to lower the energy requirements for the Oxygen Reduction Reaction.

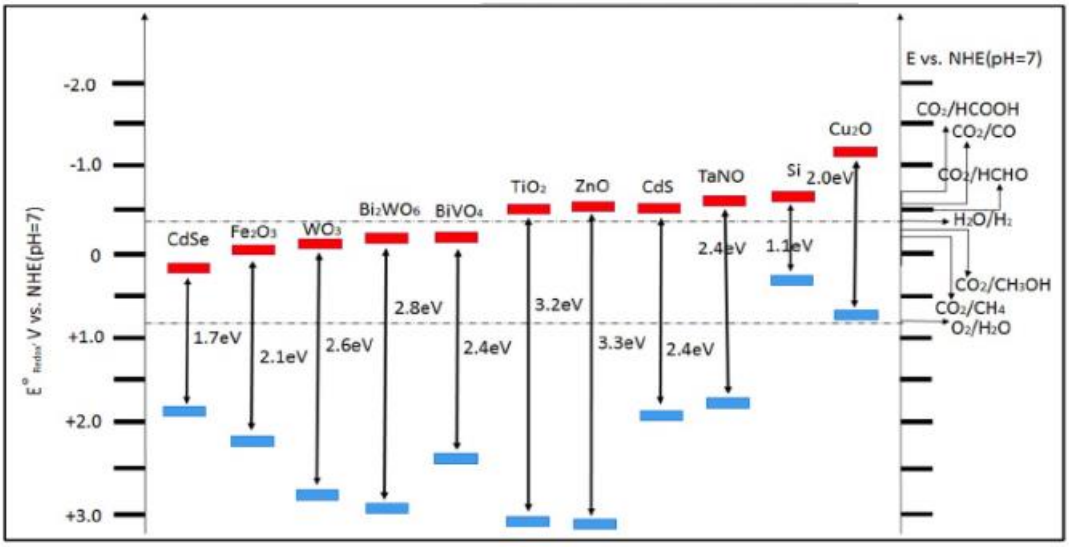

Figure 1.4: Schematic representation of conduction band, valence band potentials, and band gap energies of various semiconductor photocatalysts and relative redox potentials of the compounds involved in at $pH = 7$ [89].

High-conduction band nanoparticles also offer *stability advantages* compared to traditional catalysts. *Because nanomaterials have a higher surface area, the number of active sites is significantly higher*. This abundance of sites enables the nanoparticles to better tolerate higher levels of reactants without degrading the catalyst. Additionally, thicker layers of high-conduction band nanoparticles can be more stable under exposure to corrosive environments, making them ideal candidates for catalysis in harsh conditions.

In conclusion, the importance of high-conduction band nanoparticles in catalysis is well established. These nanoparticles offer numerous benefits, such as their ability to activate molecules that are typically difficult to react, their redox properties, and their stability advantages. These properties make them promising candidates for a wide range of catalytic applications and provide an avenue for the design of novel catalytic

materials. The investigation and optimization of nanomaterials with high conduction band energy are critical in the quest for more efficient and stable catalysts for industrial applications.

1.3.2 High conduction band in Ta-based perovskite oxides

Perovskite oxides with Tantalum (Ta) as the basic cation have gained significant attention as promising catalysts due to their unique electronic properties. The $NaTaO_3$ possesses a higher conduction band edge, i.e., $E_{CB} = -1.06\ vs\ NHE$ [92,93]. The high conduction band energy of these materials has been identified as one of the most significant factors contributing to their *high catalytic activity*. This subunit highlights the correlation between the high conduction band and the unique properties of Ta-based perovskite oxides that make them excellent catalysts.

The high conduction band energy of Ta-based perovskite oxides can be attributed to the characteristics of Ta. Tantalum has a high number of valence electrons (Ta: $[Xe]\ 4f^{14}\ 5d^3\ 6s^2$), which gives rise to a high conduction band energy for the perovskite oxide structure. They also have been found to exhibit unique oxygen vacancies, which further enhance their catalytic activity. The high conduction band energy of these materials makes the oxygen vacancies more energetically favorable, leading to a higher concentration of oxygen vacancies. These oxygen vacancies are known to be of service as actives site during catalytic reactions [94], contributing to the high activity of Ta-based perovskite oxides.

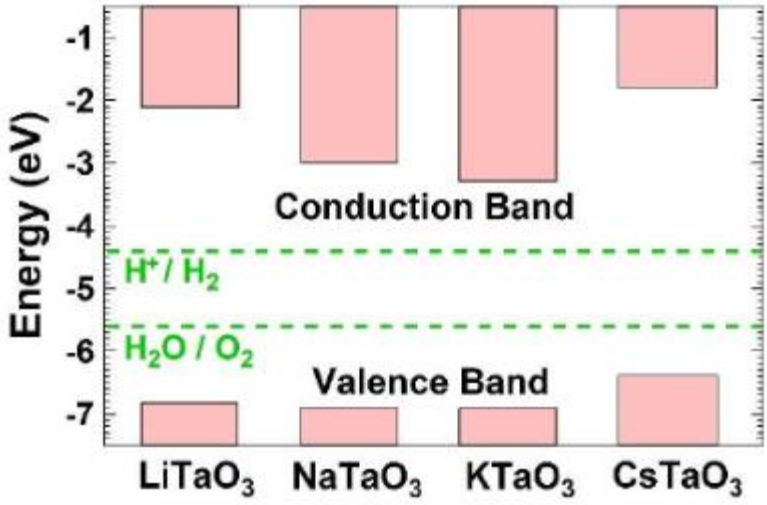

Figure 1.5: Comparison of band structure of alkali tantalate perovskites $LiTaO_3$, $NaTaO_3$, $KTaO_3$ and $CsTaO_3$ [94].

The high conduction band energy of Ta-based perovskite oxides also aids in the adsorption of reactant molecules, leading to higher catalytic activity. The unique electronic properties of these materials enable them to form molecular adsorbates with high stability, which enhances the adsorption of reactant molecules. The high adsorption of reactant molecules on the surface of Ta-based perovskite oxides facilitates easier electron transfer between the catalyst and reactant.

1.4 Single-Atom Deposition

The single-atom deposition has gained significant attention in recent years due to its potential in the field of catalysis. It involves the deposition of individual atoms of a specific element in a controlled manner on a support material, which offers unique properties for catalytic reactions. The deposition of single atoms on a substrate has the potential for improved catalytic properties, higher efficiency, and lower costs.

The concept of single-atom deposition involves the use of advanced technologies such as Atomic Layer Deposition [95], Chemical Vapor Deposition [96], and Molecular Beam Epitaxy [97] to deposit individual atoms of a specific element on a support material. The choice of the support material is critical as it affects the catalytic properties of the resulting material. The deposition of single atoms on a substrate has the potential to improve the activity and selectivity of the catalytic reaction, reduce the amount of waste generated, and improve the lifetime of the catalyst.

The single-atom deposition has numerous applications in catalysis. The unique properties of single atoms make them an ideal candidate for catalytic reactions, especially for those processes that require precise control over the reaction conditions. The use of single-atom catalysts has the potential for higher efficiency and lower costs, as they require less catalyst material, which leads to lower costs for large-scale production [98]. Moreover, the use of single-atom deposition has shown significant improvements in the selectivity and activity of catalytic reactions.

Recent advancements in the field of single-atom deposition have been focused on the development of new materials, improvement of deposition techniques, and understanding of the fundamental properties of single atoms. Researchers have been working on developing new support materials that offer improved catalytic properties, such as zeolites, metal-organic frameworks (MOFs), and graphene. Additionally, there have been significant improvements in the understanding of the fundamental properties of single atoms, such as their electronic structure, reaction kinetics, and site-specificity. Furthermore, the development of advanced characterization techniques, such as Scanning Transmission Electron Microscopy (S.T.E.M.), has allowed for the visualization and characterization of single-atom catalysts with unprecedented resolution.

Copper-based catalysts have been extensively studied for their catalytic properties in a variety of reactions [99]. Recently, the deposition of single Cu atoms on sodium tantalate perovskite has attracted attention due to its potential applications in various catalytic reactions. There are several advantages of depositing a single Cu atom on sodium tantalate perovskite.

Firstly, the interaction between Cu and $NaTaO_3$ perovskite is significantly enhanced, leading to improved catalytic activity. The deposition of a single Cu atom generates new active sites that can facilitate catalytic reactions, leading to improved selectivity and efficiency [100]. Secondly, the deposition of single Cu atoms on sodium tantalate perovskite leads to better stability of the catalyst. The single Cu atom sits on the perovskite surface in a highly dispersed form, promoting a stable and robust catalyst structure. This stability leads to a longer catalyst lifetime and better performance in catalytic reactions. Thirdly, the use of single Cu atoms reduces the need for mass production of Cu-based catalysts, leading to lower costs. The use of Cu-based materials in conventional catalysts requires a high concentration of Cu, and the production process can be costly and energy-intensive. By depositing single Cu atoms on a substrate, the amount of Cu needed is significantly reduced, resulting in a more sustainable and economical approach.

The deposition of single Cu atoms on sodium tantalate perovskite has shown significant potential in various catalytic reactions. For example, it is effective in facilitating CO_2 reduction reactions, leading to improved CO_2 conversion efficiency. Additionally, it has been used in the oxidation of alcohols, and the results indicate a much higher selectivity for the single Cu atom catalyst compared to conventional Cu-based catalysts. Furthermore, recent research has demonstrated that the single Cu atom catalyst can be used in other catalytic transformations, including electrocatalysis, photocatalysis, and oxidation reactions. The use of single-atom deposition has also shown promising results in the development of efficient catalysts for water splitting.

In conclusion, Cu^{2+} single atom deposition on $NaTaO_3$ perovskite offers various advantages over traditional catalysts, including enhanced activity, stability, and lower costs. The use of single Cu atoms has shown significant potential in various catalytic reactions, including CO_2 reduction, alcohol oxidation, and water splitting. Future research in the field of single-atom deposition can lead to the development of more efficient, sustainable, and cost-effective catalysts.

1.5 Today's Environmental and Energy Problems

The world is currently facing a critical situation due to environmental pollution and energy problems. The rise in population, industrialization, urbanization, and technological advancements have drastically affected the environment and energy resources [101,102]. Human activities are degrading the natural environment at an unprecedented rate, leading to climate change, air, and water pollution, and depletion of non-renewable resources.

Environmental problems leading to global warming, rising sea levels, and extreme weather conditions are a threat to human existence. The excessive use of fossil fuels, deforestation, and industrial waste disposal are the leading causes of greenhouse gas emissions. The use of non-renewable resources like coal and oil leads to depletion and rising costs, making it unsustainable in the long run.

Energy problems like the need for alternative and renewable energy sources, energy conservation, and energy-efficient technologies are of crucial importance. Energy consumption is rapidly increasing, and this trend is expected to continue, stressing the need for sustainable and eco-friendly solutions.

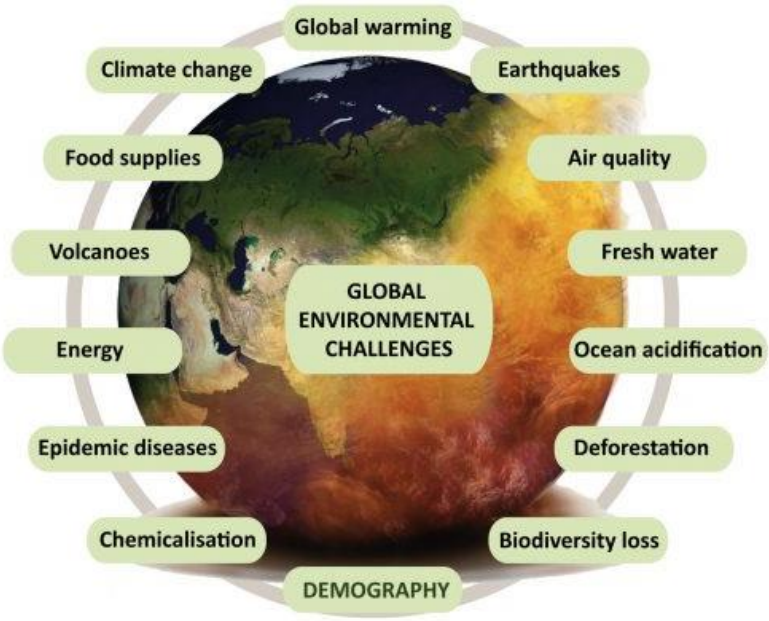

Figure 1.6: Schematic representation of global environmental problems that society is currently facing [102].

1.5.1 The Role of Hydrogen

Hydrogen production has the potential to address many of the environmental and energy-related problems faced by society today. Hydrogen is the most abundant element in the universe, and its production can be achieved using a range of renewable energy sources such as solar, wind, or hydro. There are a few ways in which hydrogen production can address these problems:

i) Reduction of greenhouse gas emissions

Hydrogen fuel produces only water vapor when burned, reducing carbon emissions and greenhouse gas emissions. In industries, hydrogen is used in fuel cells instead of fossil fuels, reducing CO_2 emissions from energy production.

ii) Promote Renewable Energy

Hydrogen can be produced using renewable energy sources, such as solar and wind power, helping to make these sources more economically viable and widespread.

iii) Energy Storage

Hydrogen can be used as a means of storing renewable energy until needed. The excess electricity generated by renewable energy sources can be used to produce H_2, which can be stored and used to produce electricity when the demand exceeds supply, reducing the dependency on non-renewable energy sources.

iv) Transportation

Hydrogen can be used as a low-carbon fuel in transportation, powering vehicles, such as cars, trains, boats, and airplanes. Using H_2 as a green fuel is rapidly establishing one of the major applications of hydrogen production to address environmental concerns.

Due to the many applications of hydrogen as a potential energy source, there are advantages and disadvantages concerning its nature which are summarized below.

Advantages of hydrogen energy

i) It can be produced from abundant energy sources (e.g., water or biomass).

ii) Hydrogen isn't toxic and presents as a clean energy source that has very high specific energy on a mass basis (for example 9.5 kg of H_2 possesses the same energy output as 25 kg of gasoline).

iii) When hydrogen is combusted, it creates a non-toxic exhaust emission. Except for some cases, where the temperature profile is high enough to create NO_x as a byproduct.

Disadvantages of hydrogen energy

i) Hydrogen liquefies at very low temperatures, thus the storage as a compressed gas or low-temperature liquid needs additional costs.

ii) When H_2 encounters the atmospheric air it ignites and that can dramatically impact the safety of the management of the product.

In conclusion, Hydrogen production and storage can provide sustainable solutions to several of the environmental and energy-related problems faced by society today. Additionally, H_2 has significant potential to create a clean, sustainable future for our planet, bringing positive effects on human health, the environment, and the economy.

1.5.2 Photocatalytic Water Splitting

An urgent need to develop a clean and sustainable energy source has emphasized the importance of hydrogen energy storage systems. Hydrogen production through water splitting is considered an attractive and sustainable approach that converts sunlight or electricity into chemical energy. A range of photocatalysts and electrocatalysts e.g., TiO_2, Cu_2O, and NiO have been widely explored to catalyze the water-splitting reaction, which favors the production of hydrogen gas.

Photocatalytic water splitting has been regarded as one of the most promising alternative methods for producing hydrogen with minimum environmental impact. Differently from electrolysis, it involves employing semiconductor materials as photocatalysts for obtaining H_2 and O_2 from H_2O molecules, in a process entirely driven by sunlight.

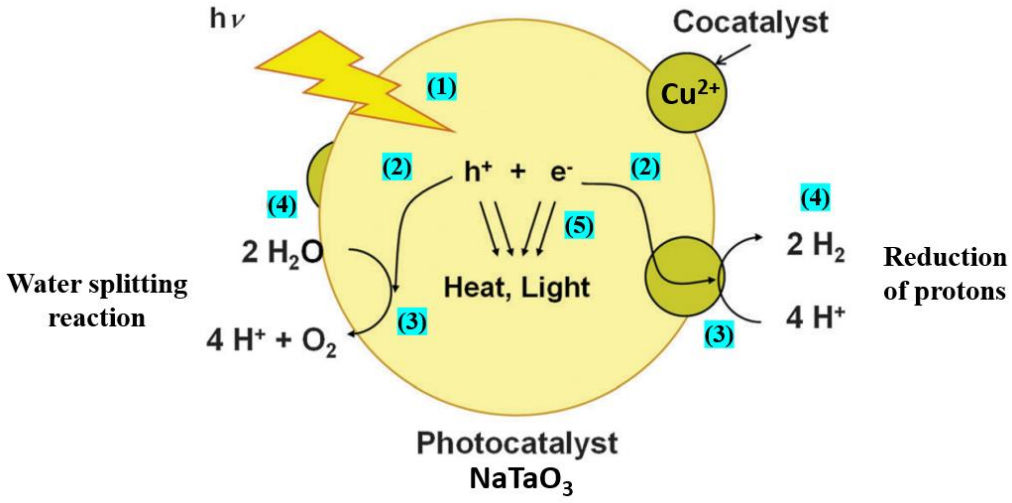

Figure 1.7: Reaction processes of water splitting on a heterogeneous photocatalyst. (1) Light absorption, (2) charge transfer, (3) redox reactions, (4) adsorption, desorption, and mass diffusion of chemical species, and (5) charge recombination

The water-splitting mechanism, illustrated in *Figure 1.7*, ideally involves four fundamental steps. The first step consists of the absorption of photons by the semiconductor, which can excite electrons from the valence band (V.B) to the conduction band (C.B). The collective effect of this process is analogous to the charge separation of an exciton: excitation of an electron (negative charge) to the C.B. and the corresponding hole (positive charge) in the V.B. [103].

Since excited electrons naturally tend to return to lower energy states, electron-hole recombination (step 2) takes place shortly after the excitation, thereby leading to energy release in the form of phonons (non-radiative) or photons (radiative recombination) [104]. This effect imposes a significant constraint on photocatalysis, as it prevents most charge carriers from reaching the material surface, where surface reactions may take place. Therefore, in step 3, electrons and holes must be effectively separated and successfully driven to the semiconductor surface. This charge transfer process is mostly dependent on the structural and electronic properties of the photocatalysts, in order that high mobility of photogenerated charge carriers is essential for the photocatalytic activity. Doping, heterojunction, and single-atom deposition approaches have been considered potential ways to alter the electronic band structure of semiconductors and thus improve their charge transfer properties [105].

Subsequently, in the presence of adsorbed H_2O at the semiconductor surface, electrons can provide a negative potential for the reduction of protons, while holes can oxidize water molecules, as part of step 4. Therefore, this chain of effects may ideally lead to the splitting of H_2O into hydrogen (H_2) and oxygen (O_2) gas, if the photocatalyst material presents adequate properties in terms of electronic structure, charge transport, surface composition, and morphology [106]. However, in a practical application under natural sunlight, this reaction is often limited by rapid electron-hole recombination rates, so the water-splitting reaction may only be observed in the presence of sacrificial reagents or by employing a high irradiation power. For this reason, the development of efficient photocatalysts for overall water splitting on a large scale remains an unaccomplished goal.

In virtue of the described mechanism, the photocatalytic process is only allowed to take place if electrons and holes have enough energy to overcome the redox potentials for each half-reaction of water splitting. Accordingly, the C.B potential must be more negative than the potential for the H^+/H_2 reduction (0 eV vs N.H.E), while the V.B level has to be more positive than 1.23 eV vs N.H.E, which is the redox potential for the O_2/H_2O oxidation. For this reason, only semiconductors with a minimum band gap of 1.23 eV can split water molecules through this method [106]. Therefore, as shown in *Figure 1.8*, only photons with energies 1.23 eV (near IR) and approximately 3.79 eV (near UV) can be utilized as the energy source for photocatalytic water splitting under natural sunlight.

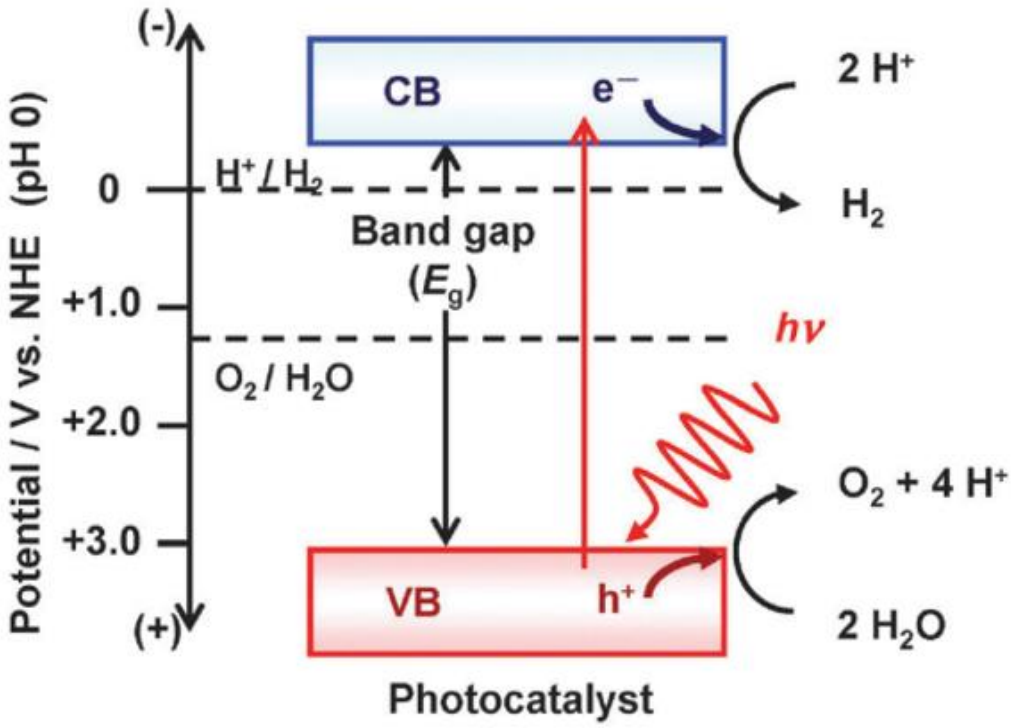

Figure 1.8: Schematic representation of the prerequisites for the valence and conduction band energies in order to overcome the redox potential of each half-reaction of water splitting [104].

The current study is focused on the development of a novel nanoparticle material, *$NaTaO_3$ perovskite oxide interfaced with Cu^{2+} atoms*, that effectively catalyzes the water-splitting reaction for efficient and sustainable hydrogen production. The nanoparticles' high conduction band, size, and large specific surface area play a critical role in the catalytic performance of the material. The thesis aims to investigate the effect of the size, shape, and chemical composition of the nanoparticles on the catalytic activity and the overall efficiency of hydrogen production.

1.6 Scope of the Master's Thesis

The main aim of the present Master's Thesis is to develop a method for controlled synthesis of $NaTaO_3$ perovskite nanomaterials, interface with Cu^{2+} single atoms using Flame Spray Pyrolysis Technology. In this context, we have screened in a systematic way the *concentration of the precursor* containing Cu atoms. The scope of the present thesis is:

i) The successful development of $NaTaO_3$ perovskite nanostructures, interfaced with Cu^{2+} single atoms via our novel synthesis method.
ii) The validation of the photoactivity, the high degree of crystallinity, and the high specific surface through physicochemical characterization techniques.
iii) The validation via Electron Paramagnetic Resonance of the successful single Cu atom deposition on the perovskite matrix.
iv) The enhancement of the photocatalytic H_2 production yield of the flame-made nanostructures.
v) The optimization of the performance of these catalysts compared to existing literature.
vi) The enhancement of the electrochemical performance of the nanostructure and their potential use in electrocatalytic Hydrogen Evolution Reaction.

Chapter 2

Experimental Methods

In this section, the focus will be on the experimental method that was used to develop the nanoparticles, along with the experimental techniques that characterized and defined their physicochemical properties.

2.1 Flame Spray Pyrolysis (FSP)

Flame Spray Pyrolysis (FSP) is a versatile one-step continuous process for the production of nanopowders [107,108] at a high rate [109] with controlled particle characteristics [110].

2.1.1 Basic Principles of Flame Spray Pyrolysis Process

A typical FSP reactor is generally comprised of three main parts [111]: an *atomizer*, a *burner*, and a *collecting system*. As shown in *Fig. 2.1* the liquid precursor must be atomized into micron-sized droplets.

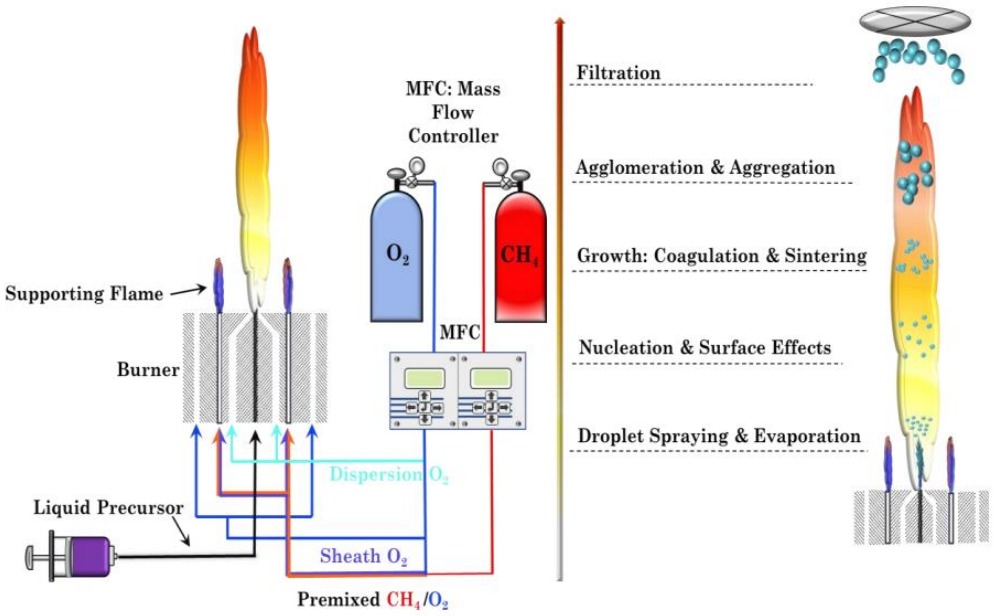

Figure 2.9: Schematic representation of a typical Flame Spray Pyrolysis apparatus.

Atomization can be achieved with different techniques like ultrasonic [112], electrostatic [113], or even air blasts [114]. The droplet size, velocity, and rate of atomization are very important for the whole FSP process. The droplet is sprayed on the flame environment at the burner. The burner comes in two types: a diffusion burner where the fuel (CH_4) and the oxidant (O_2) are not mixed before entering the flame zone, and a premixed burner where the oxidant (O_2) and the fuel (CH_4) are mixed before entering the flame zone. The premixed fuel and oxidant comprise the pilot flame where the dispersion gas (O_2) is responsible for the nebulization angle of the droplet, the conversion of the precursor into micron-sized droplets and acts as an additional oxidant for the flame environment. An additional O_2 gas flow termed sheath O_2 creates an upward stream for protection of the flame environment and assistance in the nanoparticle's collection. The liquid precursor is injected into the flame environment in the form of droplets, the droplets are combusted, and the particles are then collected in a glass fiber filter.

2.1.2 Particle Formation Process

In FSP there are two possible routes leading to particle formation, droplet-to-particle [115–117] or gas-to-particle [118–120]. A clarification must be made at this point, that even though the precursor is sprayed in micron-sized droplets into the flame environment, that doesn't mean that particle formation occurs only through the droplet-to-particle pathway.

In the particle formation process, there are two basic criteria affecting the final product. These are the combustion enthalpy density and the fraction $T_{bp,s}/T_{dp,mp}$, where $T_{bp,s}$ refers to the boiling point of the solvent whereas $T_{dp,mp}$ refers to the decomposition point of the metal precursor. It has been found [121] that high combustion enthalpies ($> 4.7\ kJ/g_{gas}$) and $T_{bp,s}/T_{dp,mp} > 1.05$ leads to homogenous powders. The liquid precursors used are usually metalorganic compounds which account for only a small fraction of the total combustion enthalpy. Most of the combustion enthalpy comes from the solvents, where high enthalpy solvents like xylene are used.

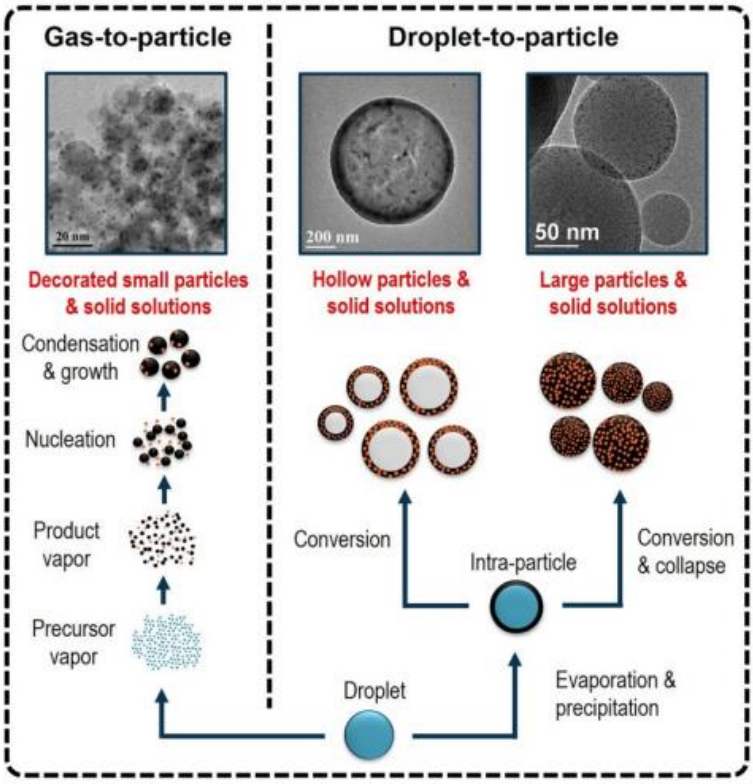

Figure 10.2: Schematic representation of particle nucleation and growth mechanisms in FSP process. Gas-to-particle (left) and droplet-to-particle (right) pathways for particle formation in aerosol synthesis [115].

In the gas-to-particle route, $T_{bp,s}/T_{dp,mp} > 1.05$ and thus the precursor decomposes before the solvent evaporates. The precursor spray ignites and reacts exothermically resulting in the decomposition of the precursor leaving a metal vapor in the hot flame environment $(2000 - 3000\ ℃)$. These conditions lead to the formation of molecular nanoclusters by nucleation. These nanoclusters due to *Brownian motion* and differences in their velocities collide with each other, resulting in *coagulation*. Coagulation is the main growth mechanism. During their growth, particles collide and stick together, either retaining their shape or fusing together forming a spherical particle. This sintering process is called *coalescence*. The final particle morphology depends on the temperature profile (cooling rate) and primary particle size and is categorized into single particles, *aggregates* where the primary particles are connected by strong sinter necks, or *agglomerates* where the primary particles are held together by weak Van der Waals bonds. When sintering is faster than coagulation, single particles are formed. When sintering and coagulation are comparable, aggregates are formed, whereas when sintering is negligible agglomerates are formed [122].

In the droplet-to-particle route, $T_{bp,s}/T_{dp,mp} < 1.05$ thus the solvent evaporates before the decomposition of the precursor thus leaving the precursor in the high-temperature zone. *The nanoparticle's size depends on the droplet size*. The precursor is concentrated on the outer layer of the droplet preventing further vaporization of the solvent. In this case, precipitation occurs, and if fast enough, a shell is formed outside the droplet and micron-explosion occurs, which induces shell-like particles. Other products include micron-sized particles.

The residence time and the temperature of the hot zone impact the sintering of particles. So, the size, morphology, and crystallinity of the particles can change depending on the variables that consist of the temperature and the height of the flame. The latter can be controlled through the Precursor flow rate (P) to Dispersion gas flow rate (D) ratio.

Increasing the *Precursor flow rate* means increasing the concentration of the solvent in the flame, which manifests as higher enthalpy content in the flame. Therefore, the time for fuel combustion lengthens, increasing the flame's height. With an increase in the sintering rate, larger particles are formed.

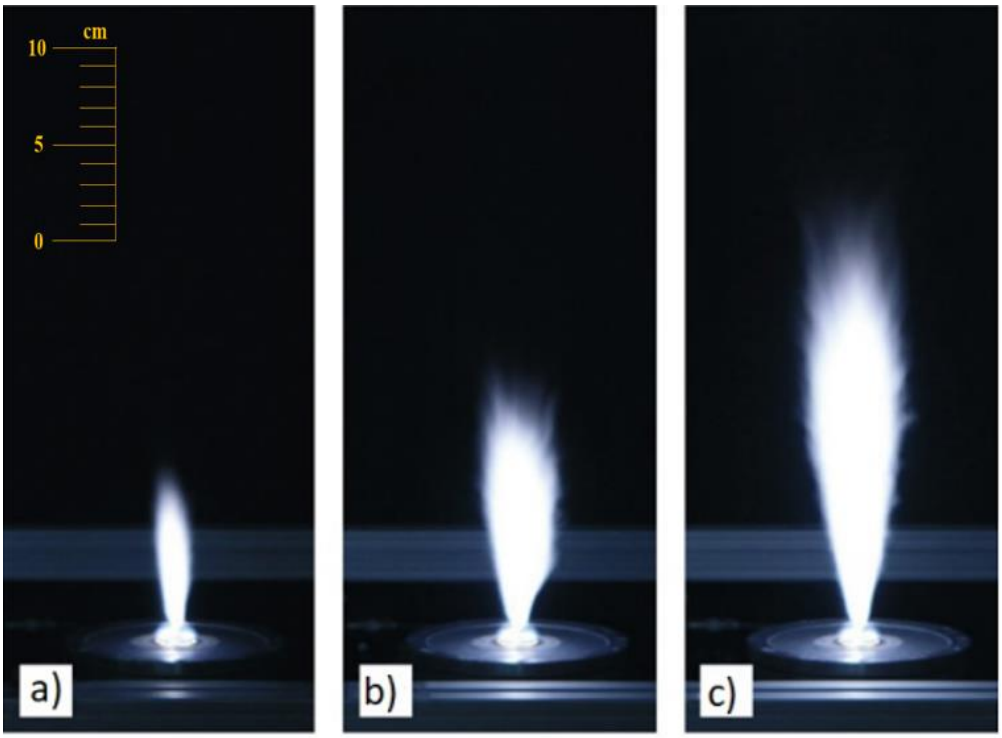

Figure 2.11: Photographs of the spray flames generated by the FSP burner as a function of the P/D ratio. a) Precursor flow rate equals to 2 ml/min and dispersion flow rate equals to 10 L/min, b) Precursor flow rate equals to 3 ml/min and dispersion flow rate equals to 7 L/min, c) Precursor flow rate equals to 5 ml/min and dispersion flow rate equals to 5 L/min.

The changes in the *Dispersion gas flow rate* impact several attributes of the flame and because of this, the flame-made nanoparticle properties change. The logical follow-up for the variables of FSP follows the pattern: increasing the dispersion gas flow rate, enhancing the combustion, intensifying the flame-solution interaction, and thus, the flame height decreases. This results in a smaller residence time, which means less sintering and smaller particle sizes (higher surface area values). Also, it decreases the precursor concentration in the flame, since the presence of oxygen is now overwhelming, so the number of particles that react with each other decreases, thus resulting in smaller particle sizes. Finally, with the increase in dispersion gas flow rate, the flame has a higher maximum temperature (T_{max}), allowing another transition of the chemical bond of the particles, that wasn't previously thermodynamically favorable.

2.1.3 FSP Advantages over other Synthesis Techniques

The main attributes that facilitate the success of Flame Spray Pyrolysis are the *speed*, *scalability*, and *flexibility* of the system.

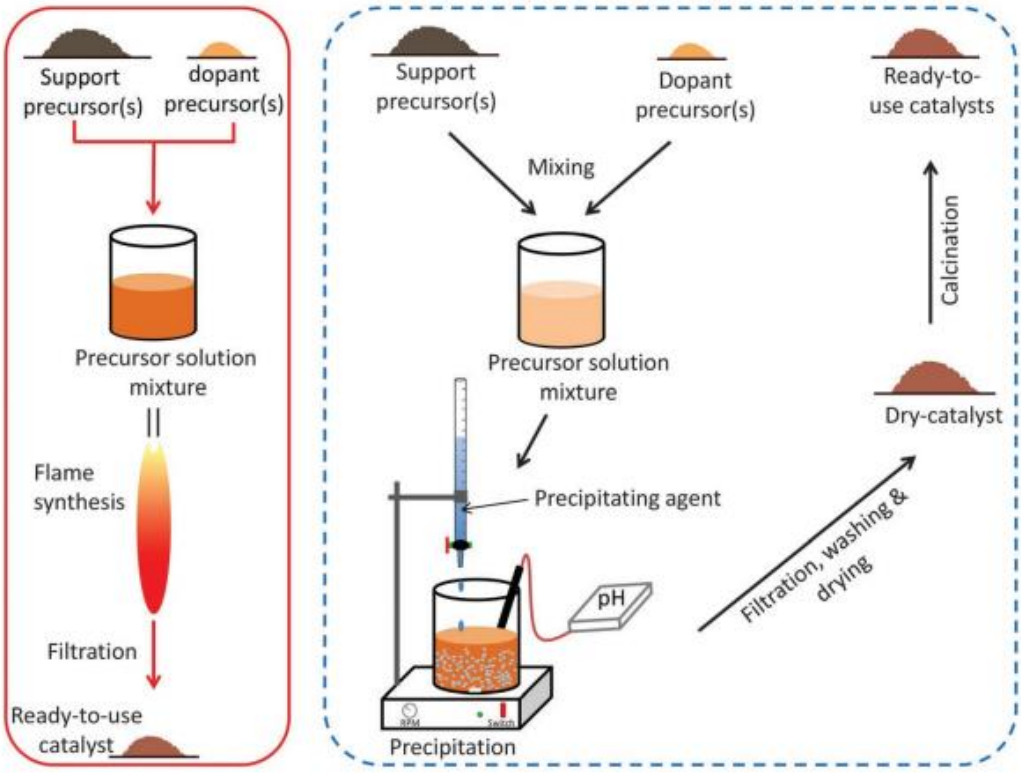

Figure 2.4: The basic steps of Flame Spray Pyrolysis technology (left). The basic steps of a wet preparation method [115] (right).

i) The system's speed

In *Figure 2.4* a schematic representation of the number of steps used for a simple FSP process is shown, compared to a wet-chemistry preparation process. With the precursor dispersed in a solvent, the whole process is accomplished in a single step inside the flame, accompanied by an instant calcination that saves a lot of time and limits the experimental errors. The process can be continuous, simply by fueling the flame with more precursor for as long as necessary. While wet-preparation (or impregnation) methods have multiple post-treatment steps e.g., filtration, washing, drying, and calcination. So, the synthesis process is possible to take days to be completed (just the drying process usually takes a day). With solvent-intensive washing, there is a possibility to alter the catalyst composition. Finally, the technique in order to produce large quantities, big batch samples, and scale-up reactors can be used, a fact which is very common in industrial-scale particle production.

ii) The system's flexibility

With some changes in the process parameters, the resulting nanoparticles can obtain very different Specific Surface Area (SSA), crystallinity, particle size, and phase composition [123]. Thus, the production of a percentage of phases that are not thermodynamically stable, but also the combination of heterostructures with the same and/or different physical properties can be achieved, thus promoting the flexibility of the technique.

iii) The system's scalability

Since the process is continuous, the industrial manufacture of nanoparticles can reach the order of $205\ \text{tons/hour}$. To this day the largest quantities produced by Flame Spray are Titania (TiO_2) and Silica (SiO_2), where Degussa one of the biggest chemical companies in the world produces AEROXIDE P25 and AEROSIL Fumed Silica, respectively. [124].

There are also some important secondary benefits compared to the wet-impregnation methods. The FSP process doesn't produce liquid byproducts that often require expensive cleaning methods. Also due to the rapid heating and quenching of flame-made nanoparticles, there is the possibility of creating metastable phases that can't be produced with wet-chemistry methods [125,126].

FSP has been shown to produce perovskite-type oxides and of course, other nanoparticles, that possess ultra-fine crystallites with primary particles of diameter as low as 5 nm, with a large specific surface area of 100 m^2/g, in contrast to other conventional synthesis routes, like solid-state reaction which is required to use heat treatments many times at high temperatures, to obtain the resulting nanoparticles. This procedure reduces the specific surface area to some tens of m^2/g [127].

Many of the disadvantages of FSP arise from the precursors. Some of them are very expensive, while not all precursors can be mixed effectively or become a homogeneous dispersion in the solvent, with possible precipitates and products of incomplete combustion in the flame [128]. Also, the products of FSP are commonly spherical agglomerated nanoparticles and it is very hard to produce different geometries [129].

2.1.4 Experimental Set-up

The FSP reactor used for the production of nanomaterials is shown in *Figure 2.5*. As discussed above, the FSP reactor comprises of three main parts: an atomizer, a burner, and the collection system.

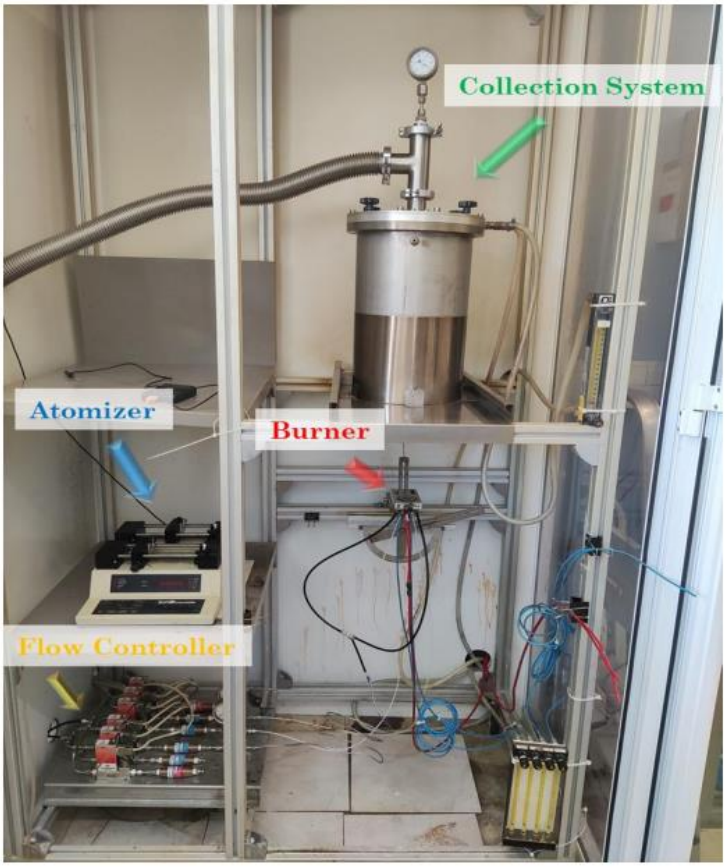

Figure 2.5: The FPS reactor with its main three components noted.

Starting from the basic component of the FSP apparatus the burner, it consists of a gas-assisted single nozzle made from a capillary of 0.5 mm inner diameter and 0.6 mm that lies in an opening of 0.8 mm thus creating an annular gap.

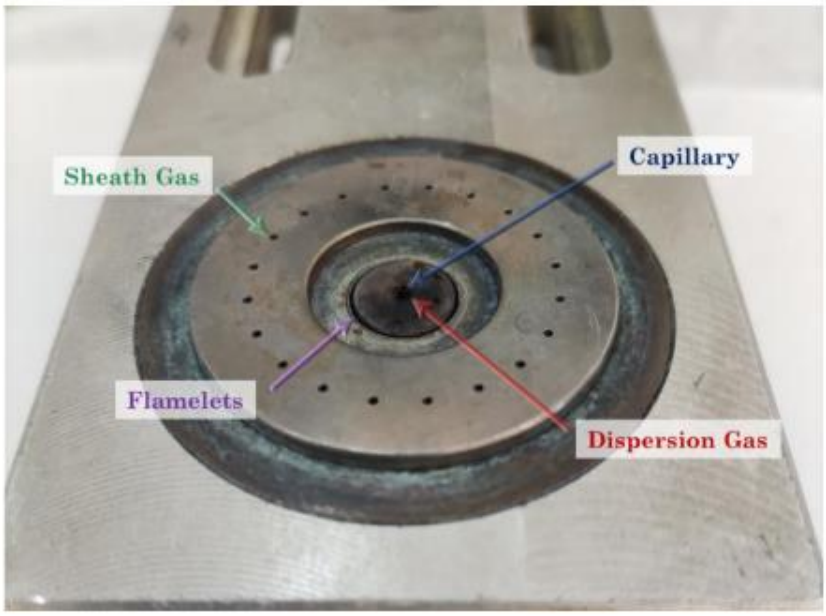

Figure 2.6: FPS nozzle configuration.

Oxygen gas is supplied in the annular gap and acts as the dispersion gas, whereas the flamelets are supplied with premixed O_2 and CH_4, comprising the pilot flame. The spray angle is determined by the height of the capillary above the nozzle opening. As shown in *Figure 2.7*, the precursor is sprayed into the flame environment after it has been converted into micron-sized droplets with the aid of the dispersion gas. The pilot flame is responsible for the initial ignition and the sheath gas protects the flame environment and facilitates particle collection.

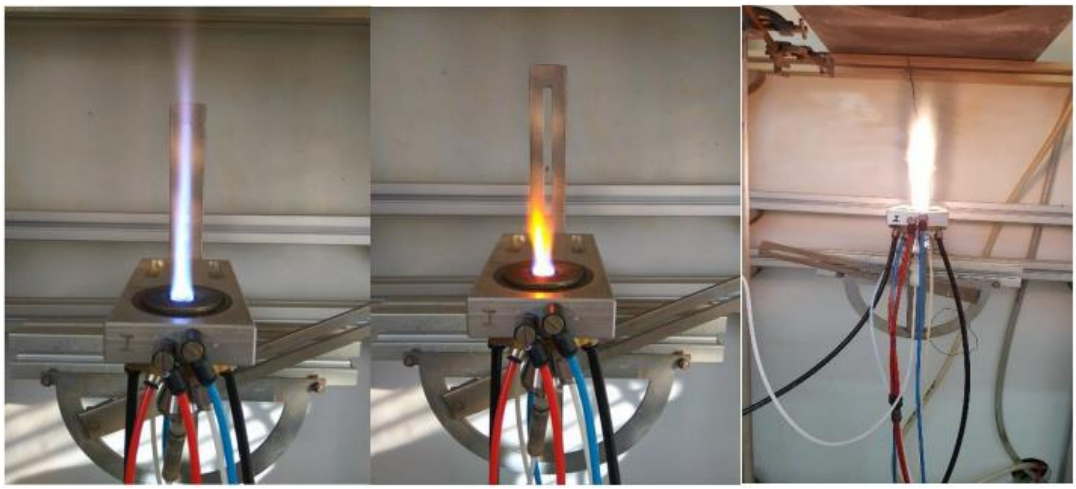

Figure 2.7: Pilot Flame (left), O_2 dispersion (middle), and precursor combustion (right) images.

The precursor is supplied in the form of micron-sized droplets with the aid of a syringe pump (Hamilton Company Inc.). Precursor flow rate can be manually adjusted as shown in *Figure 2.8*. Particle collection is done in a glass-fiber filter (Hahnemühle GF6 filter) with the aid of a vacuum pump.

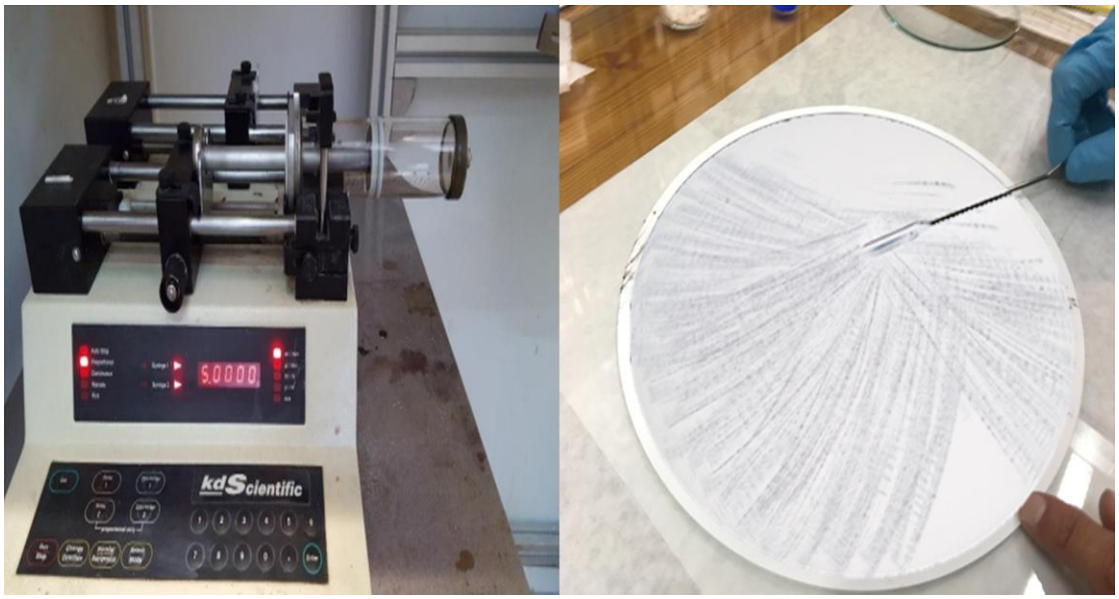

Figure 2.8: The atomization apparatus (left), where the precursor is converted into micron-sized droplets and sprayed with the aid of a syringe pump. The glass-fiber filter (right), where the particles are collected.

2.1.5 Our Novel FSP Method

So far, the successful synthesis of nanocrystalline Ta_2O_5 and $NaTaO_3$ phases has been established using various methods, including sol–gel [130,131], hydrothermal [132–134], and solid-state reactions [135,136]. These methods frequently require lengthy pre- and post-synthesis steps, such as drying and calcination, increasing considerably the synthesis time and energy consumption. Particularly, the stabilization of metal-oxide ABO_3 perovskite phases, such as $NaTaO_3$, requires high-temperature treatment, i.e., over 900 ℃. Crystalline phases are usually classified in low-temperature (L.T) and high-temperature (H.T) forms, in reference to the observed crystallization temperature (T_C) thresholds. The transition from amorphous material to L.T crystal forms occurs at approximately 650 ℃ and reversible transitions from L.T crystal forms to H.T crystal forms occur at approximately 1360 ℃ [137]. The final particle size is thermodynamically controlled by the flame-temperature profile and the *High-Temperature Residence Time (HTRT)* of the particles [138]. Hotter flames and longer HTRT tend to produce larger nanosized particles [139]. In this context, enclosing the flame with a metallic tube, 21 cm in height in the present case, enhances the HTRT.

Using a metallic tube to surround the flame, stops the surrounding atmospheric air to interfere with the flame spray jet. This prevents the drop in temperature. By not hermetically closing the tube with the nozzle, the air flow that enters will fuel the flame and create an upward stream for the nanoparticles. Each addition of such tubes in the system can increase the High-Temperature Residence Time.

A flame enclosed by a tube typically produces substantially larger particles, because of the increased residence time and the overall increase in temperature above the hot zone, compared to a flame of the same parameters.

As for an industrial level, the tube enclosure can provide better control of the flame combustion and the surrounding atmosphere, since an industrial FSP has a flame height that can reach 1 meter.

Figure 2.9: Photograph of the metallic tube at 1 cm above the FSP-nozzle in order to increase the High-Temperature Residence Time.

Aiming to achieve the interface between $NaTaO_3$ nanoparticles and single atoms in a single step inside the flame, in this thesis, a suitable system has been used that allows the surgical decoration of atoms upon a flame-made matrix, which is unique in the field of flame-made particle production (patented in 2023). The technique combines a flame synthesis of nanoparticles by Flame Spray Pyrolysis with simultaneous spraying of a precursor solution (*Figure 2.10*).

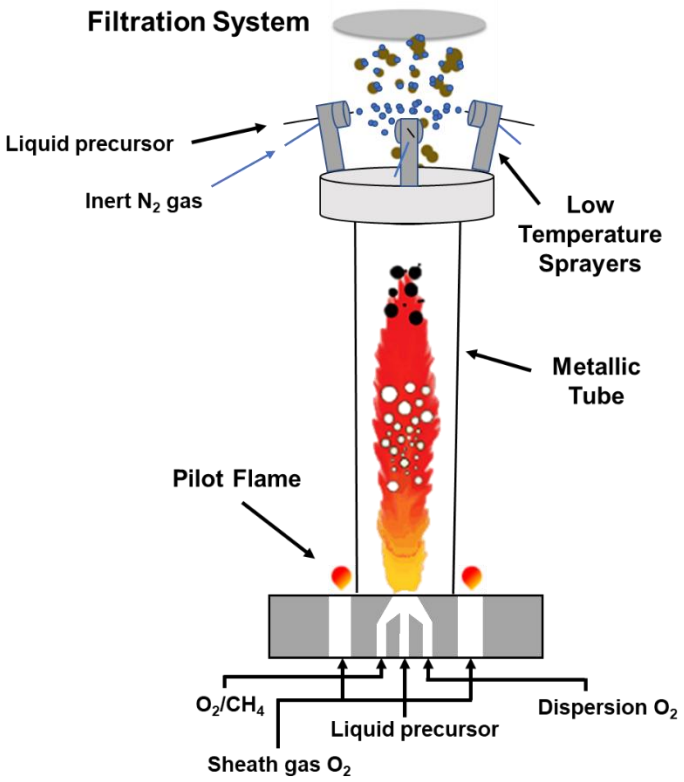

Figure 2.10: Schematic representation of the novel FSP set-up combining flame synthesis of nanoparticles with simultaneous spraying of precursor solution.

More specifically, a precursor solution is supplied in the form of micron-sized droplets with the aid of a second syringe pump. Subsequently, the droplets are sprayed through three symmetrically aligned dispersion nozzles (*Low-Temperature Sprayers*) injecting a high flow rate of inert Nitrogen (N_2) gas which is attached to each of the nozzles. The flow of N_2 is controlled so that the droplets aren't poured out in liquid form but burst as a mist just above the metallic tube. The key parameter is that the spraying is performed at the Low-Temperature zone of the FSP reactor, typically $> 30\ cm$ from the FSP combustion flame edge.

The freshly flame-made nanoparticles, vertically above the exit tube, are in-situ interfaced with the sprayed precursor in gas form. There, the sprayed metalorganic solution evaporates, without being combusted or burned. As a result, *nanostructures interfaced with single atoms*, not clusters or particles, can be synthesized in one step process by controlling the concentration of the sprayed precursor solution.

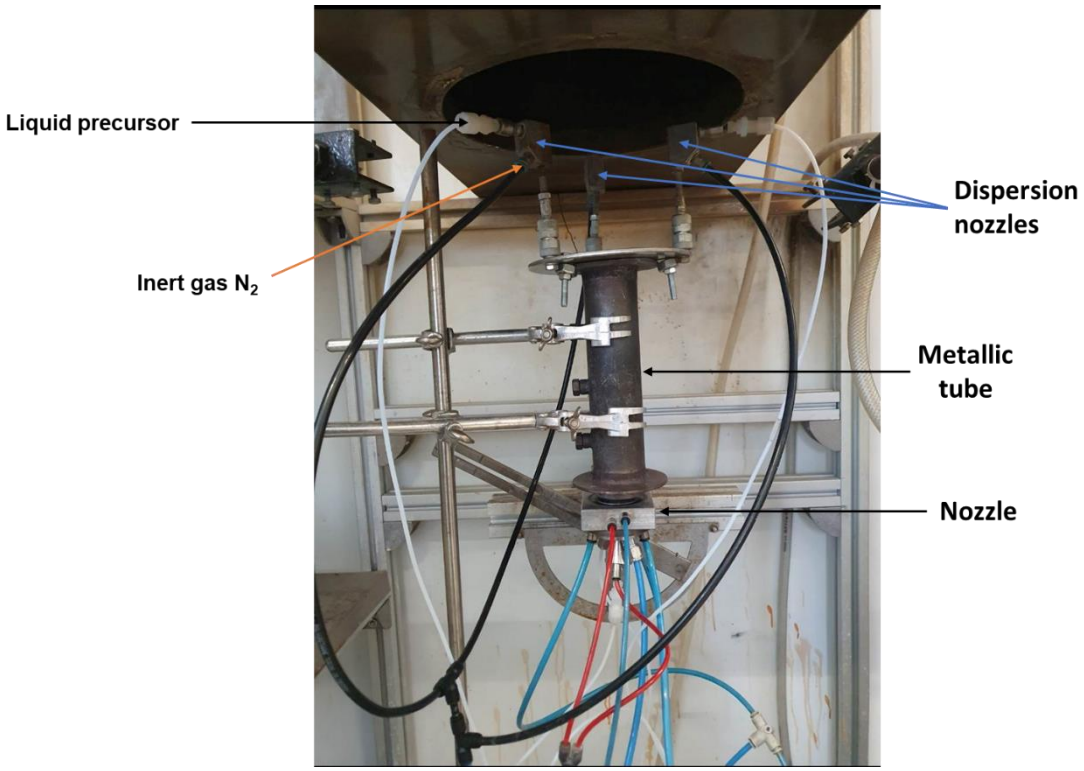

Figure 2.11: Photograph of the complete set-up used to synthesize the flame-made nanoparticles.

Through this particular FSP system, one can even decorate organic molecules on flame-made nanoparticles, a fact that has not yet been achieved with any other technique. This one-step process is beneficial since greater material losses, contamination, and labor time by multiple fabrication steps increase the chances of processing failure and the amount of required infrastructure and chemicals that skyrocket the product cost. These considerations become important when assessing the potential for large-scale fabrication.

2.2 X-Ray Diffraction (XRD)

X-Ray diffraction is a technique used for studying the crystal structure of materials. The basis of this technique is the constructive interference of monochromatic X-Rays and a crystalline sample when certain geometrical conditions are met. The resulting diffraction pattern is specific for each material and can be used for structural characterization of materials.

2.2.1 Basic Principles of X-Ray Diffraction

X-Ray diffraction from polycrystalline materials is the first, most used, and simplest quality and quantity control procedure for the identification of crystalline phases in solid materials and for those reasons has emerged as the most popular technique for analyzing the atomic structure and the formation of such crystalline materials [140–142]. The method is based on constructive interference of monochromatic X-Ray radiation of known wavelength, in the order of Å, in a crystalline sample.

In this method, the sample of material that is studied is in the form of a very fine powder consisting of microscopic crystallites, or aggregates of them, laid on a suitably shaped surface. The atoms of each such crystallite are arranged in a periodic structure of the long range. Therefore, the interatomic distances and consequently the distances between parallel atomic planes in crystals are of the same order size (~ Å) to the X-Ray wavelength. The maximum intensities of diffraction are at angular positions predicted by *Bragg's law* [143]:

$$d_{spacing} = \frac{n \cdot \lambda}{2 \cdot sin\theta}\,, \qquad (Eq.\,2.1)$$

where $d_{spacing}$ is the spacing between diffracting planes, n is an integer number that corresponds to the order of the diffraction (usually $n = 1$), λ is the wavelength of the incident X-Ray radiation, and θ is the incident angle.

When the X-Ray radiation interacts with the atoms, the light through elastic scattering spreads to the surrounding space, combining with other rays that are scattered. Most of them will cancel one another through destructive interference. But some that fulfill Bragg's law will add constructively and amplify. Therefore, the absorbed radiation, that has been detected, is converted as an increase in signal intensity.

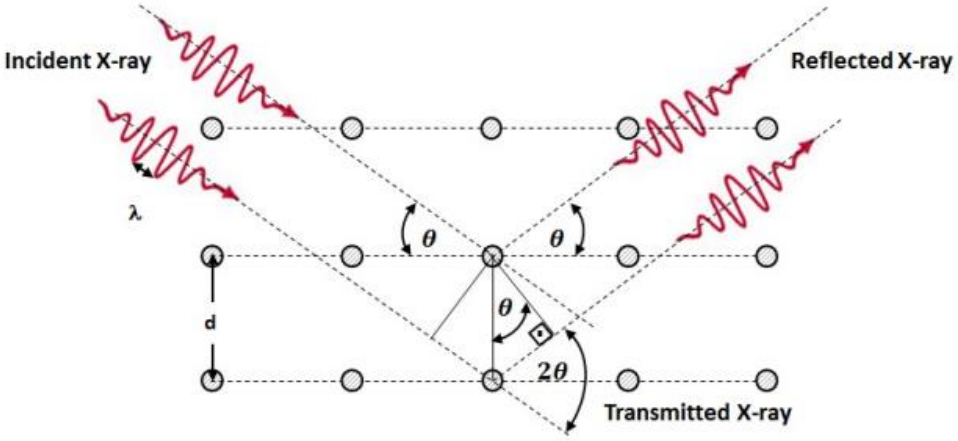

Figure 2.12: Schematic representation of Bragg's law conditions.

2.2.2 Determination of the nanocrystal size by Scherrer's equation

A single peak from the XRD pattern contains enough information to identify the phase and estimate the degree of crystallinity of the sample. Also, the mean crystal size can be calculated from the size broadening (or the width) of the peak using *Scherrer's equation* [144,145]:

$$d_{XRD} = \frac{K \cdot \lambda}{\beta \cdot cos\theta}\,, \qquad (Eq.\,2.2)$$

where d_{XRD} is the mean size of the ordered domains inside the crystalline powder, K is a dimensionless shape factor, that depends on the structure shape (usually it is close to unity, $K = 0.89$), λ is the wavelength of the incident X-Ray radiation, β is the Full Width at Half Maximum (F.W.H.M.) of the intensity of the peak (measured in radians) and θ is the detected angle that corresponds to the maximum of the peak.

Although Scherrer's equation can be used only for nanostructures larger than 1 nm, there is a limitation for microstructures larger than 0.1 μm. The advisability of the equation is bounded, as crystal lattice imperfections and strains contribute to the broadening of the peaks.

2.2.3 Experimental Set-up

X-Ray Diffraction (XRD) patterns were carried out with a D8 Advance Bruker diffractometer (*Figure 2.13*) with a Cu source ($K_a, \lambda = 1.5418\,nm$), a Lynxeye detector, and operation parameters of 40 kV generator voltage and 40 mA current. A powder diffractometer is called an apparatus that utilizes X-Ray diffraction powder or microcrystalline samples for the structural characterization of materials. Powder diffraction (pXRD) differs from the classic diffraction methods, which are commonly used with single-crystal samples. In this case, every possible crystalline orientation is represented equally in a powdered sample. pXRD operates under the assumption that the sample is randomly arranged. Therefore, a statistically significant number of each plane of the crystal structure will be in the proper orientation to diffract the X-Rays. Thus, each plane will be represented in the signal. In practice, it is sometimes necessary to rotate the sample orientation to eliminate the effects of texturing and achieve actual randomness.

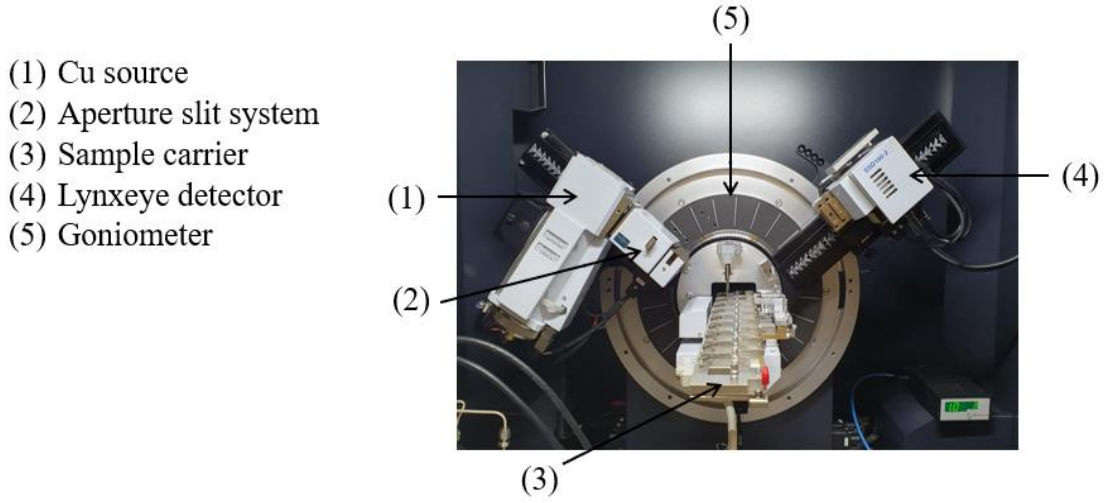

Figure 2.13: Photograph of the D8 Advance Bruker diffractometer.

The sample is placed on a holder and then is being inserted in one of the available positions of the sample carrier. The experimental parameters, including angle range, angle step, and residence time are defined by Bruker software. During the measurement, the sample rotates at a constant angular velocity such that the angle of incidence of the primary beam changes while the detector rotates at a double angular velocity around the sample; the so-called *Bragg-Brentano geometry*. The diffraction angle (2θ) is thus always equal to twice the glancing angle (θ). The phase analysis of the nanostructures was done using *DIFFRAC. EVA* and *Total Pattern Analysis Solution (TOPAS),* which are globally used line-fitting software specialized for the analysis of diffraction data and are based on the *Rietveld method* [146].

2.3 X-Ray Photoelectron Spectroscopy (XPS)

X-Ray Photoelectron Spectroscopy (XPS) is a surface-sensitive spectroscopic technique, that can identify the elemental composition and the nature of the elemental bonding that exists at the surface of a material.

2.3.1 Basic Principles of X-Ray Photoelectron Spectroscopy

The basis of this spectroscopic technique is the *photoelectric effect* [147], in which the sample under investigation is bombarded with a beam of X-rays while simultaneously measuring the kinetic energy of electrons that are emitted from the outer shell of the material.

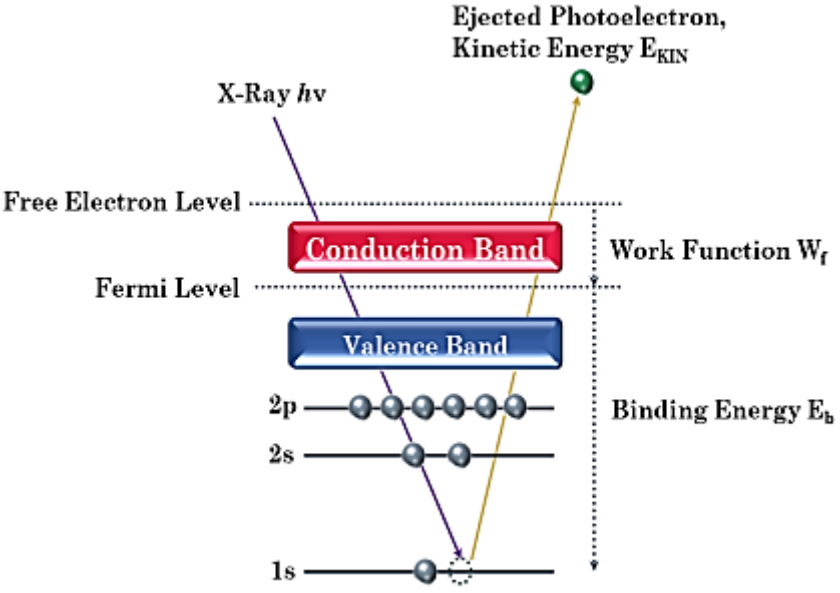

Figure 2.14: Schematic representation of the photoelectric effect.

As outlined in *Fig. 2.14*, when radiation of known energy, usually X-Rays, is absorbed by an atom or a molecule, an electron can be ejected. The kinetic energy of the ejected electron depends upon the incident photon energy (hv), and the binding energy (E_b), that is the energy required to remove the electron from the surface.

By measuring the kinetic energy of the ejected electrons, it is possible to determine which electrons are near a material's surface as well as the binding energy of the electron. The binding energy is characteristic of each element and depends on the orbital from which the electron was ejected as well as the chemical environment of the atom from which the electron was emitted.

$$E_b = hv - E_{kin} - W_f \,, \qquad (Eq.\,2.3)$$

where W_f is the work function; the minimum thermodynamic work (i.e., energy) needed to remove an electron from a solid to a point in the vacuum immediately outside the solid surface.

XPS only identifies photoelectrons that reach the detector, the elemental signals from the surface are much stronger than those from deeper in the sample. Therefore, the emitted photoelectrons originate from atomic layers close to the surface. High vacuum conditions ($\sim 10^{-9}\, mbar$) must be fulfilled in XPS measurements. High vacuum facilitates photoelectron transport to the analyzer and also prevents recontamination of clean samples.

2.3.2 Experimental Set-up

A SPECS (GmbH) spectrometer was used, equipped with a twin Al-Mg anode X-Ray source and a multichannel hemispherical sector electron analyzer (HAS-Phoibos 100), where the monochromatized Mg Kα line was set at 1253.6 eV, with an analyzer pass-energy at 15 eV, and the base pressure was to $(2-5)\cdot 10^{-9}$ mbar. The binding energies were determined versus the energy of the C 1s carbon peak at 284.5 eV. The peak deconvolution for the Shirley background and peak convolution was performed employing mixed Gaussian-Lorentzian functions in the least-squares curve fitting, using WinSpec software, developed at the Laboratoire Interdisciplinaire de Spectroscopie Electronique, University of Namur, Belgium.

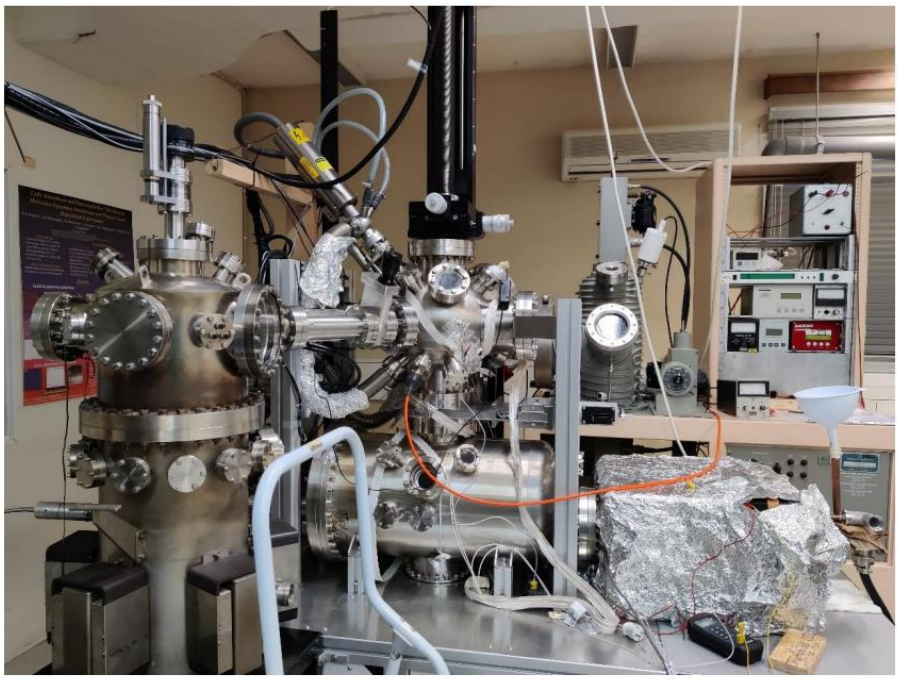

Figure 2.15: Photograph of the experimental set-up used in current thesis.

2.4 Brunauer-Emmett-Teller (B.E.T.) Analysis

The B.E.T. method (abbreviated from Brunauer-Emmett–Teller theory [148]) is the most widely used procedure for the determination of the surface area of solid or porous materials. B.E.T. analysis provides important information concerning the material's physical structure as the surface affects the way solid interacts with its environment.

2.4.1 Basic Principles of B.E.T. Analysis

B.E.T. measures surface area based on gas adsorption. The specific surface area of a particle is determined at an atomic level by the adsorption of an unreactive gas usually Nitrogen (N_2), Argon (Ar) or CO_2. In order to prevent interaction between the solid and the gas, the procedure is done at cryogenic temperatures. The temperature of the solid is kept constant under isothermal conditions, whereas the pressure of the adsorbing gas is increased. As the relative pressure is increased, more and more molecules adsorb on the surface. A thin layer will eventually cover the entire surface. The adsorption isotherm is obtained by measuring the amount of gas adsorbed across a wide range of relative pressure at a constant temperature (typically liquid N_2 at 77 K). Conversely, desorption isotherms are achieved by measuring gas removed as pressure is reduced.

2.4.2 Experimental Set-up

Prior to any measurement, the sample must be preconditioned to remove physically bonded impurities from the surface of the powder in a process called *degassing*. Samples are usually degassed either at vacuum conditions or with continuously flowing inert gas like N_2 at elevated temperatures. The temperature of the degassing process as well as the duration are carefully chosen to avoid structural changes or phase transitions in the sample.

A Quantachrome NOVAtouch LX^2 was used to record the N_2 adsorption-desorption isotherms at 77 K. The Specific Surface Area (SSA) was calculated using the absorption data points in the range of $0.1 - 0.3$ relative pressure P/P_0, while the pore radius analysis by the *B.J.H. method* [149] is in the range of $(0.35 - 0.99)$ P/P_0. The analysis of the isotherms and factors like degassing duration and temperature as well as B.E.T.-related factors were controlled with Quantachrome TouchWin software.

Figure 2.16: The Quantachrome NOVAtouch LX^2 apparatus.

The S.S.A equivalent diameter of the particles, d_{BET}, was calculated by the following equation:

$$d_{BET} = \frac{6000}{SSA \cdot p_{NaTaO_3}}, \qquad (Eq. 2.4)$$

where p_{NaTaO_3} is the density of the perovskite ($p_{NaTaO_3} = 7.129\ g/cm^3$).

2.5 Raman Spectroscopy

Raman spectroscopy [150] is a *non-destructive technique* that provides information concerning molecular interactions, chemical structure, crystallinity, and phase composition. The basis of this technique is *inelastic light scattering* due to the interaction of the incident light with the material's chemical bonds. A sample is irradiated with a single frequency radiation (usually a laser) and the energy difference between the incident beam and the scattered beam is recorded. Each material or molecule has a distinct Raman spectrum thus enabling its identification.

2.5.1 Basic Principles of Raman Spectroscopy

When light interacts with matter, the photons may be absorbed, scattered, or may not interact with the material and pass straight through it. Raman scattering involves the inelastic scattering of light upon interaction with the molecule. In Raman scattering, photons interact with the molecule and cause distortion (polarization) of the electronic cloud around the nuclei, and a short-lived state is formed called a '*virtual state*'. This 'virtual state' is formed by the electrons and the photons in the molecule in which time nuclear motion is not induced. This state is unstable, so the photons are emitted as scattered radiation.

Two cases can be discerned; if only electron cloud distortion is involved in scattering with no nuclear motion, the photons are scattered with minor frequency changes and hence the process is regarded as *elastic scattering*. This process is called *Rayleigh scattering* and it is the most dominant process. However, if nuclear motion is induced during the scattering process, energy transfer will occur either from the incident photon to the molecule or from the molecule to the scattered photon. This process is *inelastic scattering* and there is an energy difference of one vibrational unit between the incident and the scattered photon. This is called *Raman scattering* [151].

Since the virtual states are not real states and are created only when the photons interact with the electrons, their energy depends on the frequency of the light source. Depending on which vibrational energy state the process starts there are 3 types of scattering; *Rayleigh scattering* where there is no energy change and the photons return to the original energy state, *Stokes Raman scattering* where the process starts with a molecule in the ground vibrational state and *Anti-Stokes Raman scattering* where the process starts with a molecule in an excited vibrational state as shown in *Fig. 2.17*. It should be noted that at room temperature, most molecules are in the lowest vibrational (fundamental) energy state, so *Stokes-Raman scattering is the most favorable one*.

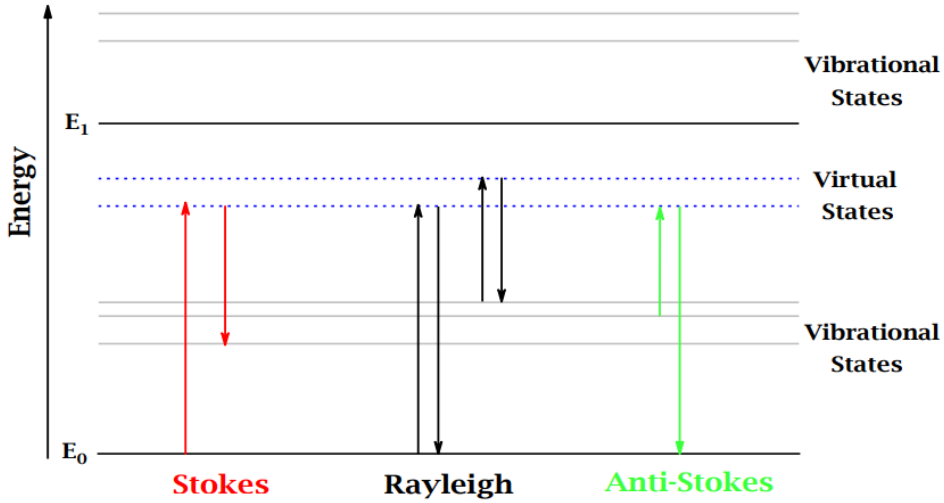

Figure 2.17: Rayleigh scattering and Raman scattering processes (Stokes &Anti-Stokes). In Stokes scattering (red arrows), the incident photon has greater energy than the scattered photon, whereas in Anti-Stokes scattering (green arrows), the incident photon is of lower energy than the scattered one.

2.5.2 Experimental Set-up

A Raman spectrometer's basic configuration consists of 3 different parts: a source of radiation which is, in general, a laser with a specific wavelength (monochromatic), a spectrometer that disperses the scattered light, and a detector that detects the scattered light. The laser's wavelength can vary from UV to Visible and near IR depending on the application. The most commonly used lasers are the 514.5 nm Ar^+ ion laser, the 532 nm Nd:YAG laser, and the 785 nm solid state. The 785 nm laser offers the best balance between scattering efficiency, influence of fluorescence, and detector efficiency.

Raman spectroscopy measurements were taken using a Horiba XploRA Plus Raman microscope coupled to an Olympus BX41 microscope and using a 785 nm laser as an excitation source. The microscope is coupled to a CCD which helped using low laser intensities of 1% or 10% in samples that were experiencing phase transformations due to heating. Spectrum was recorded and processed with Lab Spec software.

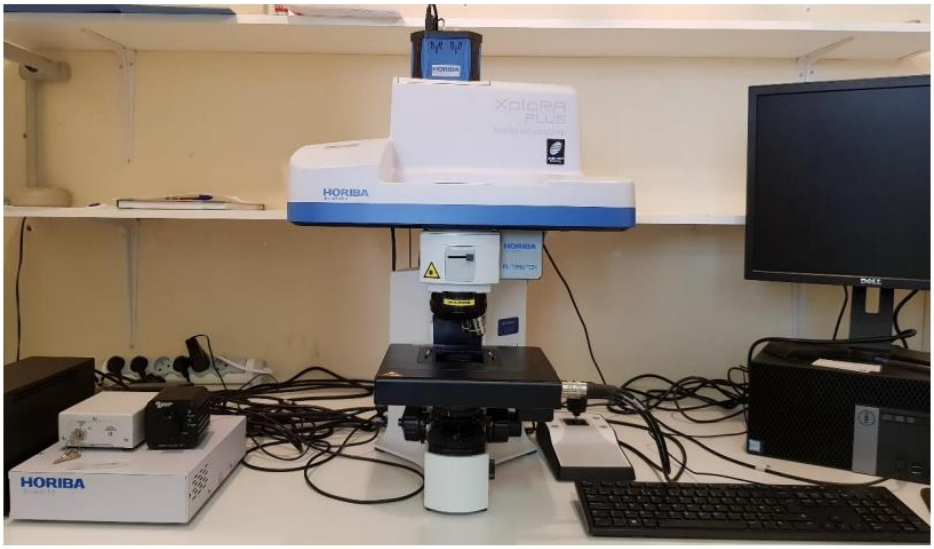

Figure 2.18: Photograph of the Horiba XploRA PLUS Raman microscope.

2.6 UV-Vis Diffuse Reflectance Spectroscopy (DRS)

Ultraviolet-Visible Diffuse Reflectance Spectroscopy (UV-Vis DRS) is a non-destructive technique used for the determination of parameters associated with the material's *optical properties* such as refractive index, reflectivity, and absorption. The scattered intensity of an incident light beam is scanned as a function of the wavelength and is analyzed concerning its macroscopic optical characteristics, such as reflectance or absorbance.

2.6.1 Basic Principles of Diffuse Reflectance Spectroscopy

When light interacts with a medium, two different types of reflection can occur [152]; *specular* (or regular) *reflection* which is associated with reflection from smooth surfaces like mirrors, and *diffuse reflection* which is associated with reflection from dull surfaces like *powders*. Both types of reflection are shown in *Figure 2.19*.

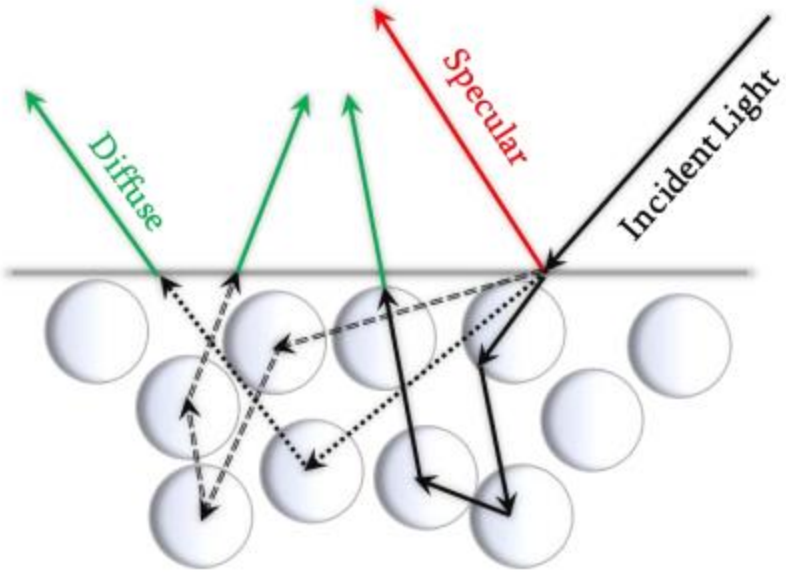

Figure 2.19: Schematic representation of light trajectories in a scattering sample.

When light interacts with a dull surface like a densely packed powdered sample, the sample will experience a combination of reflections, refractions, and diffractions (i.e., scattering) of the incident light. Furthermore, in certain materials, the light would be also absorbed. Therefore, samples of interest are samples that exhibit simultaneous absorption and scattering of electromagnetic radiation.

2.6.2 Determination of Band Gap (E_g) by Tauc plot

From the Density of States (D.O.S) theory [153], the separation between the lowest conduction band state (E_C or LUMO) and the highest valance band state (E_V or HOMO) in semiconductors generates the bandgap (E_g), which is an energy range where no electronic state exists. Depending on the value of E_g, materials characterized as insulators $(E_g > 5 - 6\ eV)$, semiconductors $(0.5\ eV\ < E_g < 5\ eV)$, and conductors (E_g close to zero).

There are, also, two types of band-to-band transitions, shown in *Figure 2.20*:

i) *Direct* transitions (or bandgaps), where the momentum is conserved without the participation of a phonon. The two edge points have the same value in the reciprocal k-space.

ii) *Indirect* transitions (or bandgaps), where at least one phonon is required for the conservation of momentum. The two edge points have different values in the reciprocal k-space.

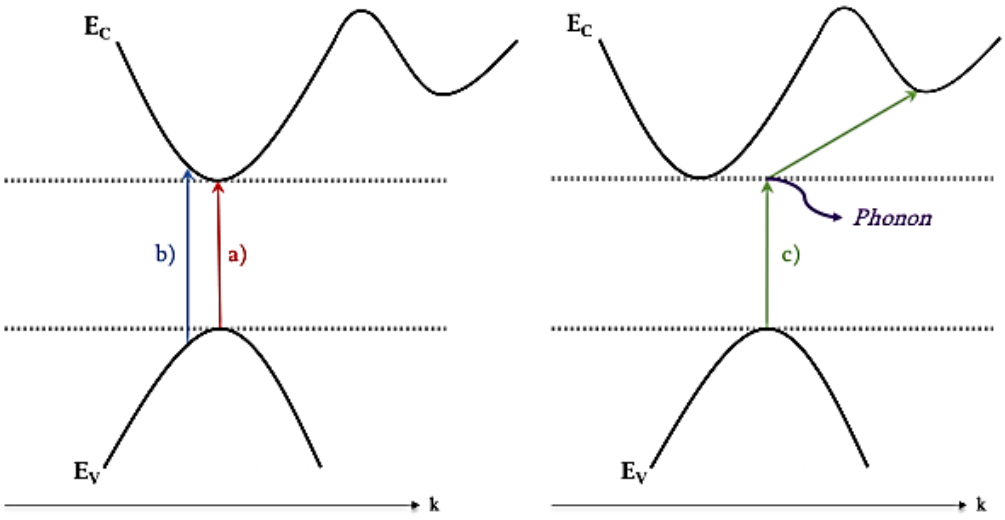

Figure 2.20: Schematic representation of the two types of band-to-band transitions. a) allowed and b) forbidden direct transitions; absorption of a photon with energy can occur E_g without the presence of a phonon c) indirect transition; the presence of a phonon is required.

The *Kubelka-Munk function* [154] is used for the determination of the optical band gap of semiconductors.

$$F(R_\infty) = \frac{(1 - R_\infty)^2}{2R_\infty} = \frac{K}{S}, \qquad (Eq. 2.5)$$

where R_∞ is the absolute remittance of a diffusively reflecting sample, K is the absorption coefficient, and S is the scattering coefficient. Assuming that the scattering coefficient changes negligibly, the Kubelka-Munk function depends solely on K. The correlation between the *absorption*, α, connected to the absorption coefficient K and the incident photon energy $E = h\nu$ can be achieved with a correlation function also involving an electronic transition-dependent exponent n. After a few modifications, the final expression of the Kubelka-Munk function reads as [155]:

$$(a \cdot h\nu)^{(1/n)} = C\big(h\nu - E_g\big), \qquad (Eq. 2.6)$$

where E_g is the bandgap energy, a is the absorption, $h\nu$ is the incident photon energy, C is a constant, and n is the electronic transition-dependent exponent.

Depending on the type of transition each time occurs, the exponent n takes the following values, summarized in *Table 2.1*.

Table 2.1: Types of electronic dipole transitions and their corresponding n-values.

Transition Type	n
direct, allowed	1/2
direct, forbidden	3/2
indirect, allowed	2
indirect, forbidden	3

By plotting the left part of *Eq. 2.6* against the photon energy hv, the bandgap energy E_g can be extracted by a linear fit at its rise. The crossing point between fit and abscissa will determine the bandgap energy. This representation is called *Tauc Plot* [156] and provides quantitative calculation of bandgaps. It should be noted that an ideal material with no imperfections would have a step-function-like plot and as a result, the bandgap in the Tauc plot would be measured precisely. An actual material contains impurities, surface defects, and other imperfections that alter its structure and result in a deviation from the ideal step-function-like line. For precise calculation of the bandgap energy, the fitted line must always pass through the middle of the experimental line.

Misuse of the Tauc Plot to determine the bandgap energy of the semiconductors may lead to erroneous estimates, especially in the case of modified semiconductors. Makula et al [157] addressed the aforementioned issue and proposed the correct way to determine the bandgap energy. An additional linear fit used as an abscissa must be applied for the slope below the fundamental absorption. The point where the two lines cross is the bandgap energy of the semiconductor.

2.6.3 Experimental Set-up

DRS experiments were conducted using a Perkin Elmer Lambda 35 spectrophotometer. The spectrophotometer uses a halogen lamp and a deuterium lamp to cover the wavelength range from 190 to 1100 nm. The switch from the halogen lamp to the deuterium lamp occurs at around 380 nm. The beam path is shown in *Figure 2.21*.

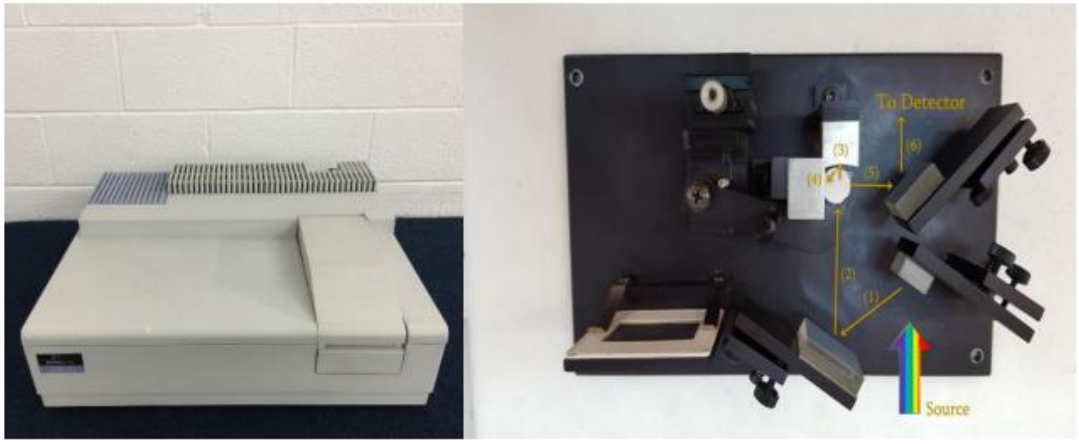

Figure 2.21: Photograph of the Perkin Elmer Lambda 35 spectrophotometer (left). The optical beam path inside the apparatus (right).

The procedure starts with the measurement of the standard reference sample to perform autozero. Barium sulfate, $BaSO_4$, (Riedel-de Haën 11432) is used due to its high absolute reflectance ranging from 0.973 to 0.988. After performing autozero, the sample to be measured is placed on the DRS holder and the measurement starts. As discussed before, all the samples must be packed carefully to have a smooth surface. After the measurement, the spectrum and the data are processed by software.

2.7 Electron Paramagnetic Resonance (EPR)

Electron Paramagnetic Resonance (EPR) is a technique based on the absorption of electromagnetic radiation, which is usually in the microwave frequency region, by a paramagnetic sample placed on a magnetic field. Paramagnetic species (species that have *unpaired electrons*) like free radicals and transition metal ions can be identified in solids, liquids, and gases as well as defects can be studied.

2.7.1 Basic Principles of Electron Paramagnetic Resonance

The electron possesses an intrinsic angular momentum, the spin. Electron is a spin $S = 1/2$ particle and in the quantum mechanical description the electron spin can be in two states $m_S = +1/2$ and $m_S = -1/2$. These two states, which are the projection of the electron spin, differ only in the orientation of the angular momentum in space and not in the magnitude.

The postulate of quantum mechanics states that definite components of the spin can be determined only in a specific axis. This means that the two spin states can be only on one axis, usually around the z-axis. In the absence of interactions between the electron spin with its environment, any choice for the direction in space of the z-axis is allowed. The electrons spin randomly, and the two states have the same energy, thus they are *degenerate* [158]. The electron spin angular momentum is associated with the magnetic moment by the formula:

$$\overrightarrow{\mu_e} = g\mu_B\vec{S}, \qquad (Eq.\,2.7)$$

where μ_B is Bohr's magneton ($\mu_B = 2.274 \cdot 10^{-24}\ J/T$) and g is the Lande factor or simply the g-factor $\left(g_{free\ electron} = 2.0023\right)$. The energy of a magnetic moment when a constant magnetic field is applied is given by the scalar product between the magnetic moment $\overrightarrow{\mu_e}$ and the magnetic field $\vec{B}$. Spin comes along the z-axis as discussed earlier and therefore the scalar product reduces to a single term if the magnetic field is applied to the z-direction. This reads as:

$$E = -\overrightarrow{\mu_e} \cdot \vec{B} = g|\mu_B|\vec{S} \cdot \vec{B} = g|\mu_B|B_0 \cdot S_z \qquad (Eq.\,2.8)$$

Since spin (S_z) has two states $m_S = +1/2$ and $m_S = -1/2$ by substituting in Eq. 2.8, the following expression results:

$$E_{\pm} = \pm\left(\frac{1}{2}\right) g|\mu_B|B_0 \qquad (Eq.\,2.9)$$

The energy difference due to predominately the interaction of an unpaired electron in the sample in the presence of a magnetic field is called the *Zeeman effect* [159]. According to *Planck's law* [160,161], the energy difference between the two states is:

$$\Delta E = E_+ - E_- = g|\mu_B|B_0 = hv, \qquad (Eq.\,2.10)$$

where h is Planck's constant ($h = 6.62 \cdot 10^{-34}\ J \cdot s$) and v is the frequency of the radiation.

Concluding, the two spin states have the same energy in the absence of a magnetic field, so without a magnetic field, there is no energy difference to measure. The energies of the spin states diverge linearly as the magnetic field increases and the energy difference depends linearly on the magnetic field. The absorption of energy causes a transition from a lower energy state to a higher energy state. Typically, the frequencies vary from the MHz range through visible light, to ultraviolet light. Radiation in the GHz range with a wavelength of a few cm is used for EPR experiments.

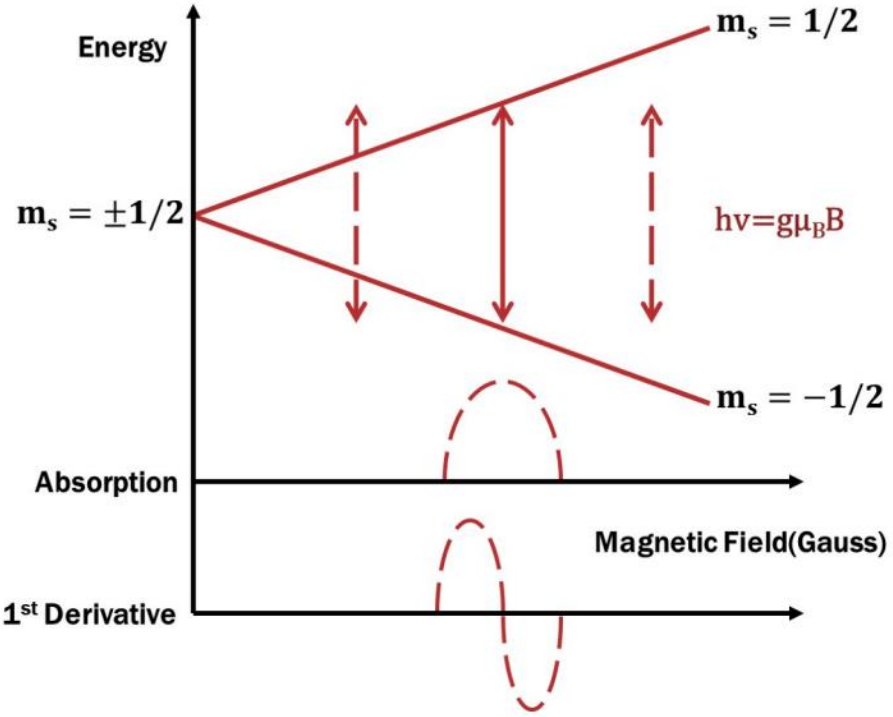

Figure 2.22: The Zeeman effect [159]. In the absence of magnetic field ($B = 0$) the spin states have the same energy. Application of static magnetic field ($B \neq 0$) leads to the separation of the two states; one with high energy when the magnetic moment is aligned with the magnetic field and one with low energy when the magnetic moment is aligned against the magnetic field.

The energy difference between the two spin states can be varied by changing the magnetic field strength, thus there are two potential approaches to obtaining spectra. The magnetic field could be held constant while the frequency of the electromagnetic radiation is scanned, which would be analogous to UV-Vis spectroscopy. Alternatively, the electromagnetic radiation frequency could be held constant while the magnetic field is being scanned.

Absorption of energy occurs when the magnetic field tunes the two spin states such that the energy difference matches the energy of the applied radiation. This field is called the *resonance field*. Resonance techniques are known for their high-resolution measurements. This technique can measure up to 10^{-11} spins. Because of difficulties in scanning microwave frequencies and because of the use of a resonant cavity for signal detection, most EPR spectrometers operate at constant microwave frequency and scan the magnetic field.

On a practical level, absorption gives a faint signal that usually coexists with random noise. The signal is selectively amplified through (a) *suitable amplifiers* and (b) the *Frequency Modulation* (F.M.) technique [162], where a small additional oscillating magnetic field is applied *perpendicularly to the external (Zeeman) magnetic field* at a typical frequency of 100 kHz (*microwave* region). By detecting the peak-to-peak amplitude the first derivative of the absorption is measured. Also, using phase-sensitive detection only signals with the same modulation (100 kHz) are measured. This results in higher signal-to-noise ratios. It should be noted that the application of this configuration for the detection of EPR signals results in the eventual recording of the first derivative of the signal, shown in *Figure 2.22*, and not the absorption. The resonance field is easily located from the zero point of the derivative intensity. The EPR absorption signal is a Lorentzian function, which represents the shape of the EPR resonance line.

The parameter used as a *fingerprint* for each molecule would be the *g-factor* since it's the only variable that remains constant at different frequencies and magnetic fields. It helps distinguish and identify types of samples. A useful expression is the following:

$$g = \frac{hv}{\mu_B B_0} = 714.5\ \frac{v\ (GHz)}{B_0\ (Gauss)} \qquad (Eq.\ 2.11)$$

Note that high g-values occur at low magnetic fields and vice versa. The g-factor helps to distinguish and identify types of samples as a function of the mobility of the valence electron. Carbon-centered radicals have g in proximity to the free electron value, which is 2.0023. Heteroatoms shift the g-factor.

So far, only the case of one molecule in a fixed orientation has been discussed. Since molecules are oriented in space, mixing them would make the analysis direction dependent. This is expressed in observable parameters with the *anisotropy of the g-factor* [163,164]. The term anisotropy refers to the different g-values due to the molecule's orientation relative to the external magnetic field. The g-factor has a set of principal axis system labeled as g_x, g_y and g_z . Depending on the values of the g-factor there are different line shapes in an EPR spectrum as shown in *Fig. 2.23*.

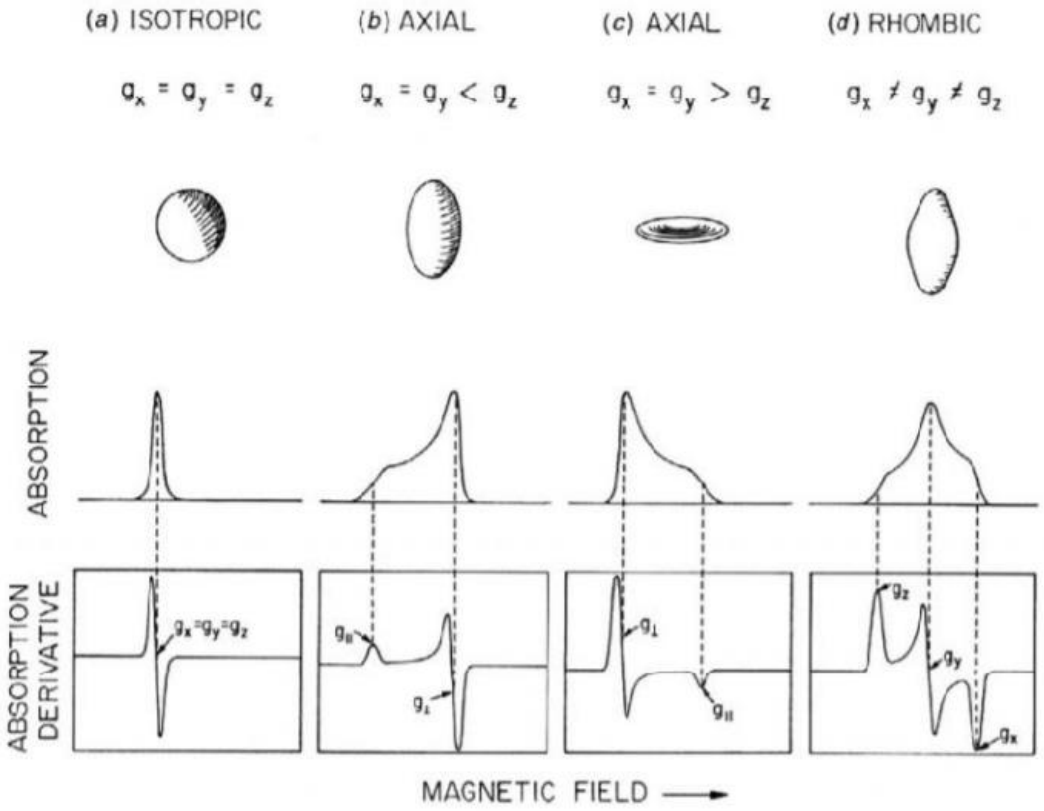

Figure 2.23: Schematic representation of the anisotropy of the g-factor and the corresponding absorption and EPR spectra [164]. Depending on the g-values there are different types of anisotropy. *(a)* Equal g-values in 3 directions result in an *isotropic g-factor*. *(b,c) Axial g-factor* has one component different than the others. *(d) Rhombic g-factor* has different components in 3 directions.

As shown in *Figure 2.23* anisotropy is responsible for the line shape in an EPR spectrum. Starting from the isotropic case where only dipolar interactions are considered, the absorption spectrum follows a Gaussian distribution. Progressing to a higher order in perturbation theory, more interactions are added (e.g., exchange interactions, spin-orbit coupling), the isotropic spectrum begins to deviate, and the absorption line takes the form of a Lorentzian distribution.

2.7.2 Experimental Set-up

The basic components of an EPR spectrometer are the *microwave bridge* and the EPR *magnet*. Starting from the microwave bridge, the most used one would be the X-Band microwave bridge operating at around 9.6 GHz. From *Eq. 2.9* it is apparent that $g = 2$ comes for a resonance field of 3380 Gauss. The microwave bridge houses the source and the detector. The microwaves are produced in the source as shown in *Figure 2.24* and pass through a variable attenuator. The attenuator controls the flow of microwave radiation and thus the microwave power can precisely be tuned.

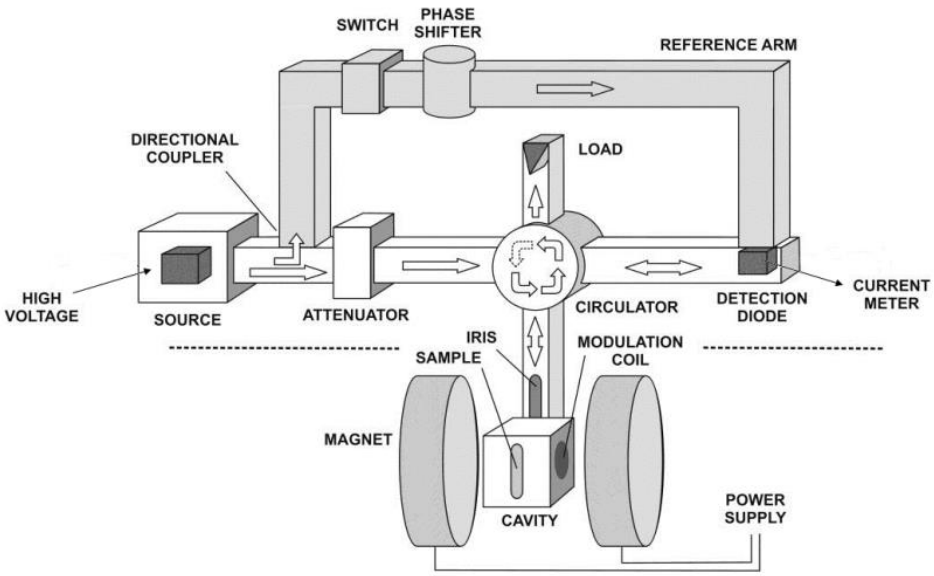

Figure 2.24: Schematic representation of an EPR spectrometer [161].

Most EPR spectrometers are reflection spectrometers meaning that they detect reflected radiation from the microwave cavity, which is a metal box where the sample is placed. This happens because of the circulator. The circulator guides the microwaves with the aid of waveguides towards the cavity. The microwaves are coupled into the cavity via the iris which tunes the amount of radiation being reflected by matching the impedances of the waveguide and the cavity. The reflected radiation passes through the circulator and is guided to the detector. Any remaining radiation that was been reflected from the detector is forced by the circulator into the upward waveguide and the radiation is converted into heat. The detector measures DC current. The DC current is transformed into AC via a lock-in amplifier, thus producing the EPR signal.

These properties give rise to an EPR signal in the following way. In general, the cavity stores microwave energy and thus at resonance frequency no microwaves will be reflected but will remain inside it. When the sample absorbs the microwave energy the impedance in the cavity changes and thus the cavity is no longer coupled, and the microwaves will be reflected to the bridge resulting in the corresponding EPR signal.

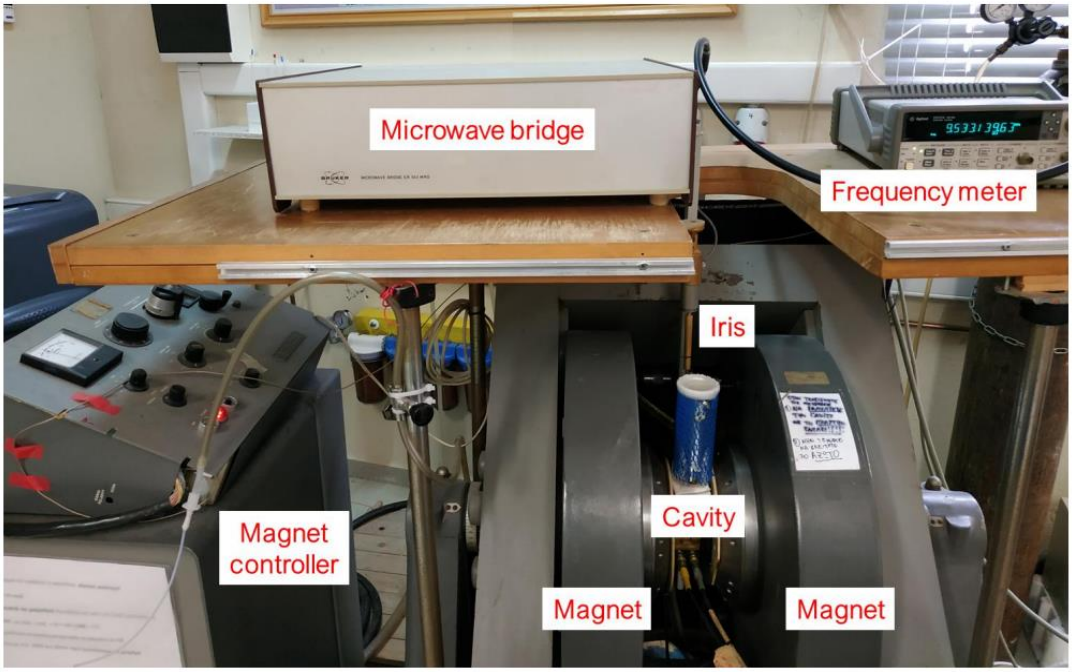

Figure 2.25: Photograph of EPR spectrometer components used in current thesis.

EPR experiments are conducted on various temperatures ranging from that of liquid helium (4.2 K), liquid nitrogen (77K), and room (R.T) up to high (1200 K) temperature. The EPR experiments were carried out using a Bruker ER 200D spectrometer with a Bruker X-Band microwave bridge operating in the region of 9 – 10 GHz. Samples for electron-hole studies were placed in quartz tubes of 5 mm, degassed for 20 min, and placed inside a Dewar at liquid nitrogen temperature (77 K). The samples were illuminated using an Oriel 6293 Arc Xenon Lamp with a maximum output of 800 W. The microwave power was controlled using a microwave controller and the magnetic field by a field controller. The EPR spectra were recorded and processed using Lab-View software.

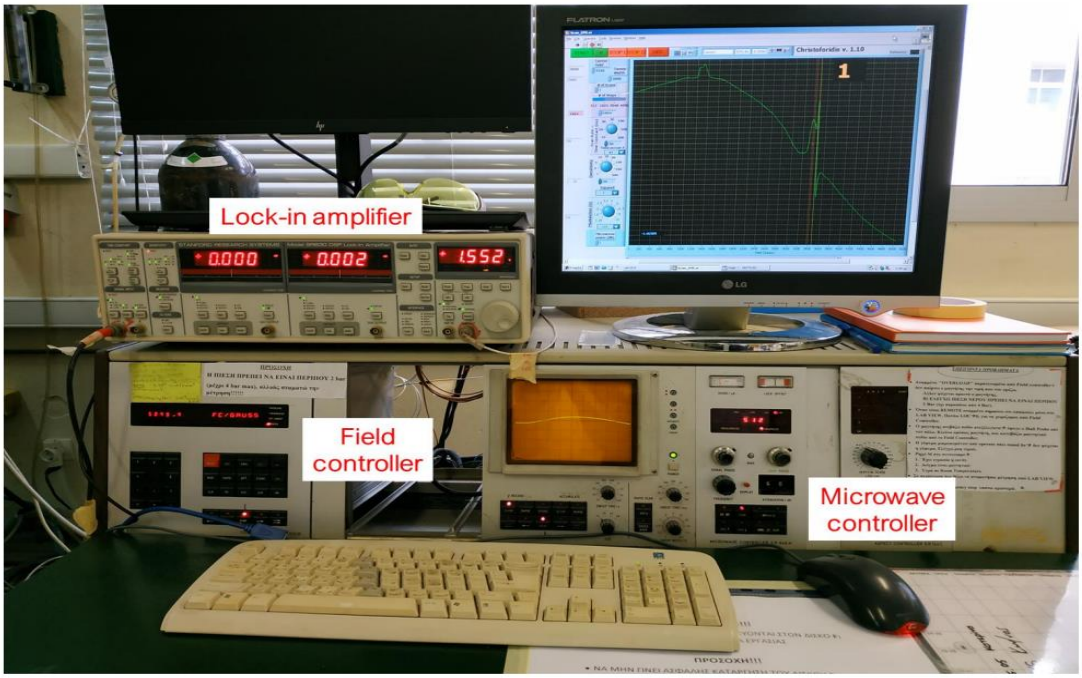

Figure 2.26: Field, microwave controllers, and lock-in amplifier necessary for accurate EPR signal acquisition.

2.7.3 ''Peisach – Blumberg'' Correlation of $g_{\parallel}$ and $A_{\parallel}$ factors

Peisach and Blumberg [165] demonstrated an extension of a method relating chemical structure to the EPR parameters $g_{\parallel}$ and $A_{\parallel}$.Those parameters can in certain instances be used for the assignment of the structure of metal-binding sites in artificial and natural nonblue copper proteins. This technique, while sometimes leading to ambiguous assignments, can often be used for the unequivocal assignment of structure, especially in conjunction with other studies. Furthermore, these assignments derived from the EPR parameter can be used to describe the chemistry of ligand-exchange reactions in copper proteins.

Divalent copper occurs naturally or can be added to specific and nonspecific binding sites in various protein molecules. Cu^{2+} has 9 d electrons (Cu^{2+}: $[Ar]4s^2 3d^9$), which are always maximally paired to give a total spin $S = 1/2$. The g-tensor is of the *axial type*, showing a major absorption to higher field at $g_{x,y} = g_{\perp}$, and lesser absorption to lower field at $g_z = g_{//}$. As the nuclear spin of each naturally occurring isotope, ^{63}Cu and ^{65}Cu, is 3/2, the EPR spectrum of Cu^{2+} will show a hyperfine splitting of four features $(2I + 1)$.

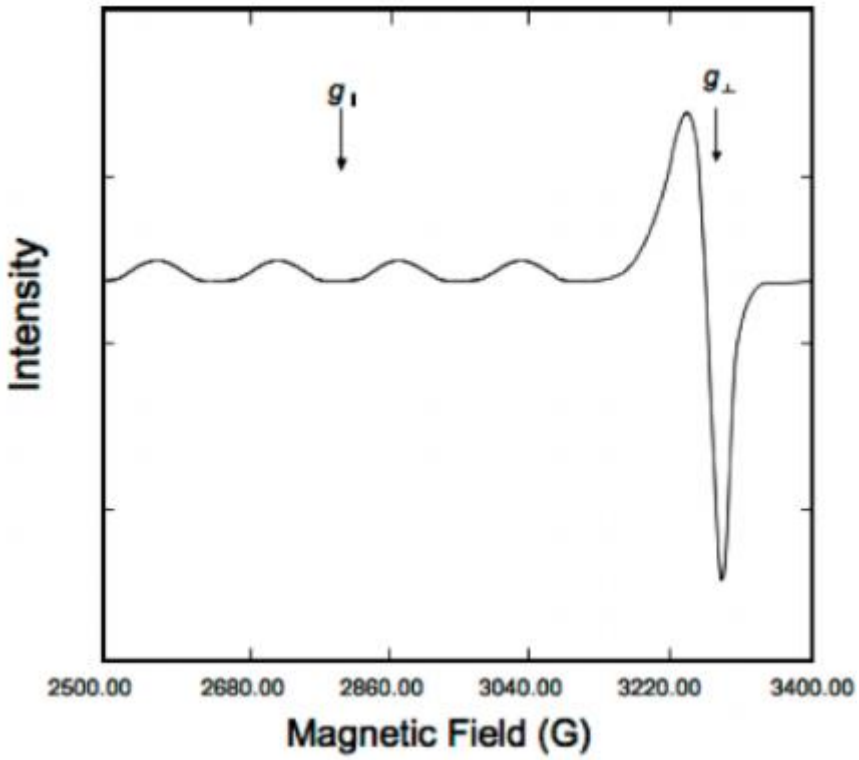

Figure 2.27: Typical X-band EPR spectrum of Cu^{2+} compounds [167].

The hyperfine splitting, $A_{\perp}$, arising from the nuclear magnetic moment of the Cu^{2+} at $g_{\perp}$, is usually very small so this feature of the spectrum often shows no splitting. On the other hand, $A_{//}$, the nuclear hyperfine splitting at $g_{//}$, is usually much larger, and the four features at $g_{//}$, are often resolved [166,167]. It is the magnitude of $A_{//}$, and $g_{//}$ which are dependent, among other things, on the nature of the ligands of Cu^{2+}, and these values can often be used to assign *structure*.

When Cu^{2+} is ligated to nuclei having a nuclear magnetic moment greater than zero, one can sometimes observe the super-hyperfine splitting of various features of the EPR spectrum. This splitting arises from the magnetic interaction of the unpaired electron spin with the nuclear magnetic moment, and the resulting pattern provides a signature for the kind and number of these nuclei.

Depending on the type of **g** and **A** tensors (isotropic, axial, or rhombic), the copper EPR spectrum changes dramatically. Next, the three cases that arise in terms of the type of **g** tensor in relation to the type of **A** tensor are described separately.

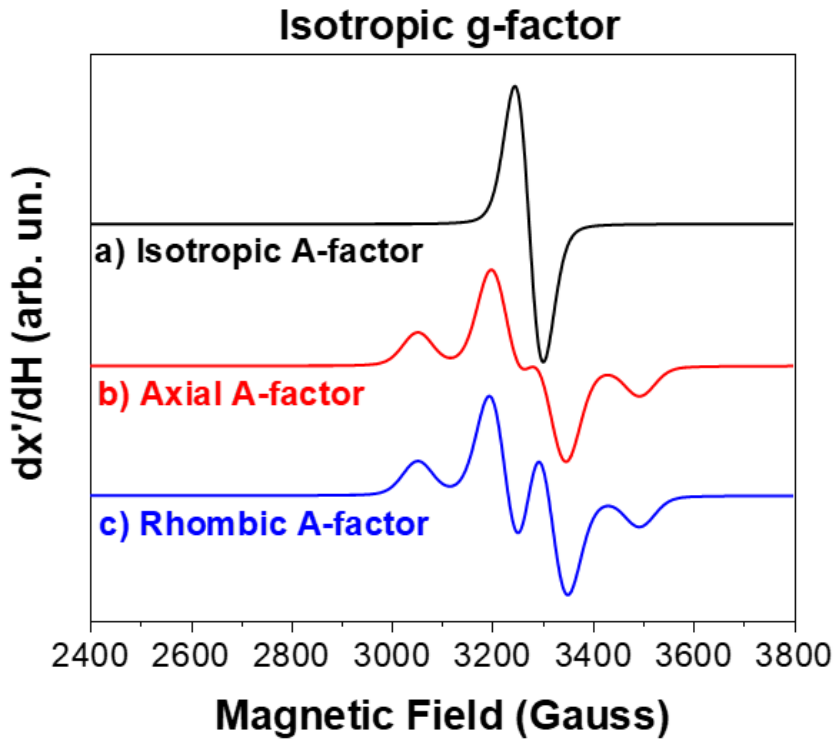

Figure 2.28: EPR spectra of Cu^{2+} with isotropic g-tensor. The black, red, and blue lines correspond to isotropic, axial, and rhombic A-tensor, respectively.

Figure 2.28 shows the spectra obtained in the first case where the **g**-tensor is isotropic $(g_x = g_y = g_z)$. When the g-tensor is isotropic, the electrons have greater mobility, because there is no restriction of their movement in any direction in space. Depending on the type of **A**-tensor, there are changes in the recorded spectra. The sub-case of the isotropic **A**-tensor $(A_x = A_y = A_z)$. is very common when studying systems with a high concentration of copper (e.g., clusters) where the spin centers are not isolated from each other. At room temperature, it is the most common spectrum observed. As the shape of the **A** tensor changes to axial $(A_x = A_y \neq A_z)$ or rhombic $(A_x \neq A_y \neq A_z)$, the hyperfine interactions separate and shift. *g and* **A***-tensors shift due to the change in the type of coordination*.

Figure 2.29 shows the spectra obtained in the second case where the **g**-tensor is axial $(g_x = g_y \neq g_z)$. The case of the axial tensor is the most common in the systems where copper is studied. When the **g**-tensor is of axial type, the electrons feel a restriction of their motion in one (z) direction., thus their mobility is reduced in that direction.

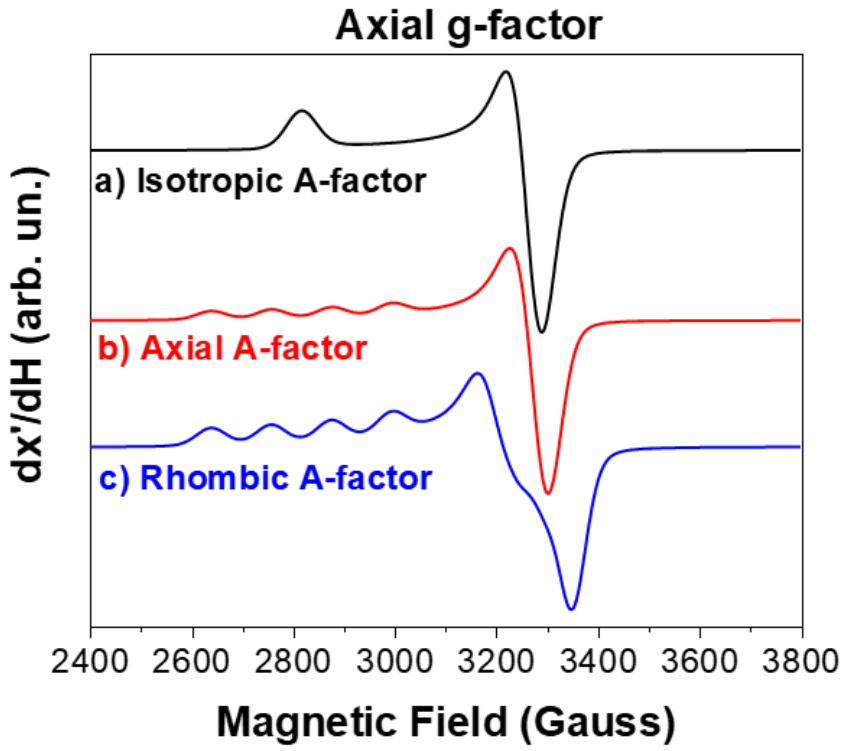

Figure 2.29: EPR spectra of Cu^{2+} with axial g-tensor. The black, red, and blue lines correspond to isotropic, axial, and rhombic A-tensor, respectively.

In the subcase of the isotropic **A**-tensor $(A_x = A_y = A_z)$, one hyperfine interaction is observed instead of four at large g-values (small magnetic field values). The four hyperfine interactions have been broadened so much that they are essentially indistinguishable from each other, resulting in a flattened curve. In the case of the axial $(A_x = A_y \neq A_z)$ and rhombic$(A_x \neq A_y \neq A_z)$, **A**-tensor, the hyperfine interactions are distinct, and in the latter case a shift of the g-values in the vertical plane (g_x, g_y). is observed, to the point where they are also distinct from each other.

In the latter case of the rhombic **g**-tensor $(g_x \neq g_y \neq g_z)$., shown in *Figure 2.30*, electron mobility is limited in all three directions. In all subcases of the **A**-tensor, the form of the **g**-tensor is distinct. When the **A**-tensor is isotropic $(A_x = A_y = A_z)$, as explained in the previous case, the 4 hyperfine interactions are broadened and separate from each other in the case of the axial **A**-tensor $(A_x = A_y \neq A_z)$. Finally, when the **A**-tensor is of rhombic symmetry $(A_x \neq A_y \neq A_z)$, the contributions in the parallel plane (x,y) can also be distinguished.

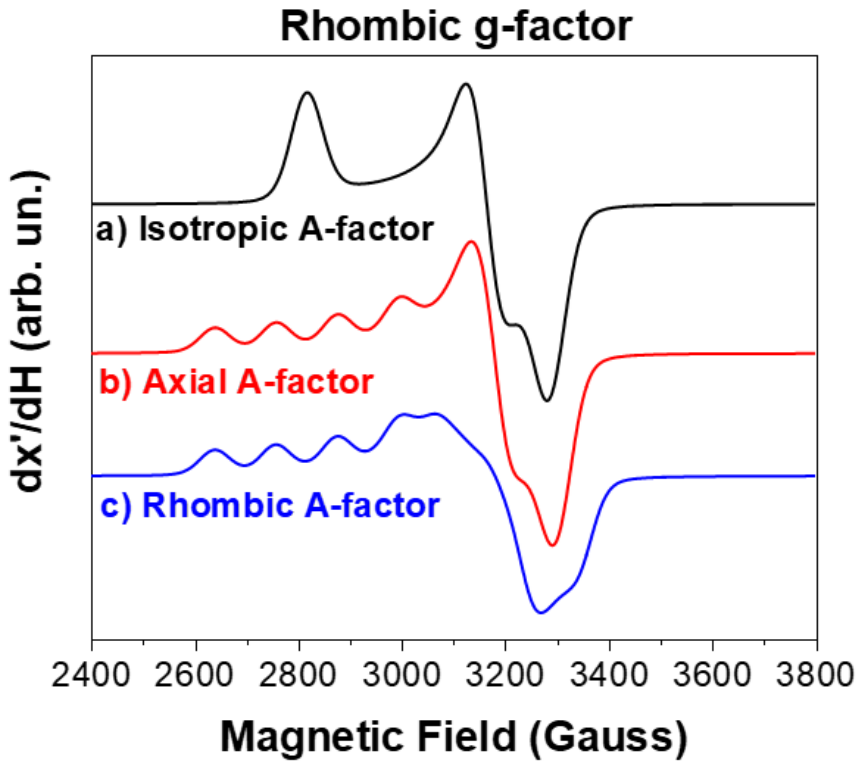

Figure 2.30: EPR spectra of Cu^{2+} with rhombic g-tensor. The black, red, and blue lines correspond to isotropic, axial, and rhombic A-tensor, respectively.

In frozen solutions of Cu^{2+} bound to model complexes, the physical constraints that can exist in the specific sites of the copper compounds are most often not present, and EPR can be used as a probe of the structure of the copper-binding site.

The relationships of $g_{\parallel}$ and $A_{\parallel}$ for different classes of model compounds in which the structure and charge are known or can reasonably be assigned. In the simplest cases, where all the ligands to the copper consist of the same atom, either *all nitrogen* (4N) or *all oxygen* (4O), one can almost unambiguously make a structural assignment based on the EPR parameters. For any one species, for example, all-oxygen ligation compounds of varying charge lie in a region arbitrarily set off in the figure. The total charge of the metal ion and its four principal ligand atoms varies from $2+$ to $2-$ monotonically within this region. Nitrogen is more electron-rich than oxygen and this is reflected in smaller values of $g_{\parallel}$ and larger values of $A_{\parallel}$. Having calculated the EPR parameters $g_{\parallel}$ and $A_{\parallel}$ one can define the ligands in copper complexes where the ligand structure for the metal ion is unknown. In *Figure 2.31* the various regions have been indicated which are representative of the different types of ligands to copper that one might encounter.

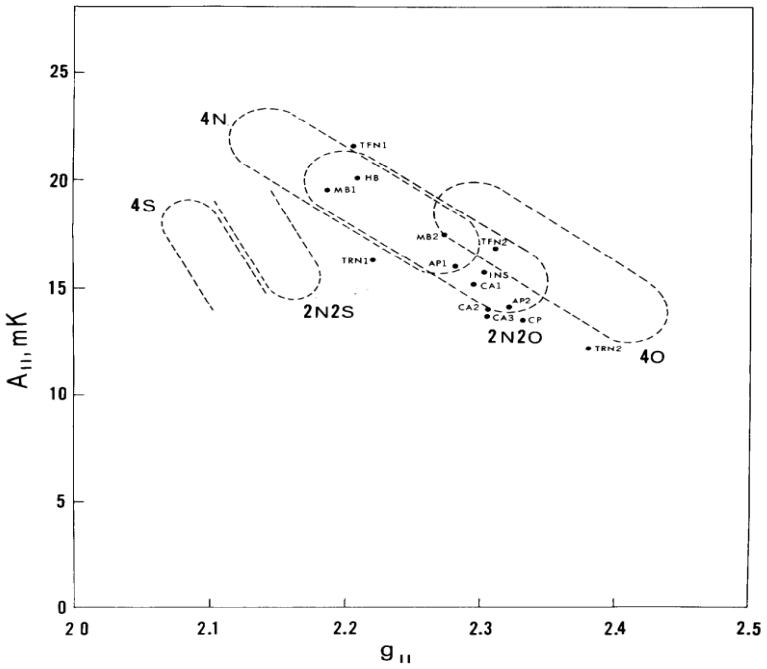

Figure 2.31: The relation between $g_{\parallel}$ and $A_{\parallel}$ for copper complexes [165]. The regions set off by dashed lines are corresponding to four sulfur atoms (4S), two sulfur and two nitrogen atoms (2N2S), four nitrogen atoms (4N), two nitrogen and two oxygen atoms (2N2O), and four oxygen atoms (4O).

There are two caveats in the use of that figure. The first and most obvious is that there are regions of overlap among the different types of ligation, and this overlap may be worsened by charge differences and differences in the nature of the atoms of the second ligation sphere. The second and most important is that small deviations from square planar coordination will shift $A_{\parallel}$; to smaller values while larger deviations will also shift $g_{\parallel}$, to smaller values (closer to $g = 2$) as well.

2.7.4 Quantification of an EPR Spectrum

It is possible to determine the number of spins in a sample without the concurrent measurement of a reference sample. In this case, the double integrated intensity of the experimental spectrum and a software calculation is used to measure the number of spins. The area under the absorption spectrum of an EPR signal is, just as in optical spectroscopy, a direct measure of the concentration of unpaired electrons. Unlike electronic absorption spectroscopy, however, there is no extinction coefficient in EPR spectrometry.

To correlate the intensity of the EPR signal with a concentration, a standard is needed. Different standards can be used. For example, if an EPR signal presents a radical close to $g = 2$ and $B_0 = 3390$ Gauss, a spin $S = 1/2$ system standard is needed (e.g., copper nitrate) in order to quantify this signal. Having experimental measurements of copper which comes from the combustion of copper nitrate, its selection is one-way in the present thesis. By comparing the spin concentration of the copper standard with the spin concentration of the signal of interest the concentration of that signal can be determined. To make a comparison between the EPR signal of interest and a standard the spectra to be compared must be obtained under the same conditions. The recorded EPR spectra are the first derivatives of the normal absorption spectra. Since an EPR spectrum is a first derivative, a double integration is needed to obtain the intensity, i.e., the area under the absorption spectrum.

2.7.5 Spectral Simulation and Analysis by EasySpin

The curve simulation process was carried out by EasySpin, an open-source MATLAB toolbox for simulating and fitting a wide range of EPR spectra. It supplements the numerical and visualization power of MATLAB with the best computational methods devised by EPR spectroscopists. In EPR spectroscopy, computerized data processing, numerical spectral simulations, and iterative parameter fittings are essential in extracting quantitative information on structure and dynamics from experimental data. It is developed by the author and was originally conceived as a simulation program for solid-state continuous wave EPR spectra in the laboratory of Arthur Schweiger at ETH Zurich, with a first public release in 2000. Numerical simulations of EPR spectra are usually performed with three intentions [168]:

(i) systematic study of the dependencies of spectral features on the magnetic parameters,

(ii) predictions whether a new experiment will give new information, and

(iii) accurate parameter extraction from experimental spectra.

The g-values are calculated exclusively using EasySpin, comparing the fitting of the theoretical curve with the experimental measurement.

2.8 Electrochemical Impedance Spectroscopy (EIS)

Electrochemical impedance spectroscopy (EIS) is a powerful technique for studying the electrochemical properties of materials, including their charge transfer resistance (R_{ct}), capacitance, and double-layer capacitance (C_{dl}). EIS has been widely used in various fields, including material science, electrochemistry, and biology, for investigating a range of phenomena such as corrosion [169,170], redox couple reactions [171,172], energy storage [173–175], and biochemical reactions [176,177].

2.8.1 Basic Principles of Electrochemical Impedance Spectroscopy

The technique involves applying a small amplitude sinusoidal voltage to a sample and measuring the resulting current response, which can be used to calculate the impedance of the system as a function of frequency.

From a mechanistic point of view, an electrochemical reaction at an electrode–electrolyte interface can be decomposed into a series of multistep processes (mass transport, charge-transfer processes, adsorption), each occurring at distinct rates. The individual steps are time-dependent and may occur at different timescales [178–180]. Therefore, the use of transient techniques such as EIS, which enables the analysis of time-dependent mechanisms based on the response (current or potential) of the electrochemical system collected at selected frequencies, is required to facilitate the evaluation of electrochemical systems.

Macdonald [181] wrote that electrical equivalent circuits (EECs) are merely analogs, rather than models. Using an EEC as a model, one can describe an electrochemical reaction that takes place at the electrode/electrolyte interface. Then it is examined whether an EEC can indeed be used as a model for the reaction at the electrified interface. The current flowing at an electrified interface due to an electrochemical reaction,

$$O + ne^- \rightarrow R, \qquad (Eq.2.12)$$

always contains non-faradaic components, no matter how well the measurement is made. In the above equation, n is the number of electrons transferred, O is the oxidant, and R is its reduced product (reductant).

The electron is transferred across the electrified interface [180], as illustrated in *Figure 2.32a*. The charge transfer leads to both faradaic and non-faradaic components. The faradaic component arises from the electron transfer via a reaction (*Eq. 2.12*) across the interface by overcoming an appropriate activation barrier, namely the *polarization resistance* (R_p), along with the uncompensated *solution resistance* (R_s). The non-faradaic current results from charging the *double-layer capacitor* (C_{dl}). When the charge transfer takes place at the interface, the mass transports of the reactant and product take on roles in determining the rate of electron transfer, which depends on the consumption of the oxidants and the production of the reductant near the electrode surface.

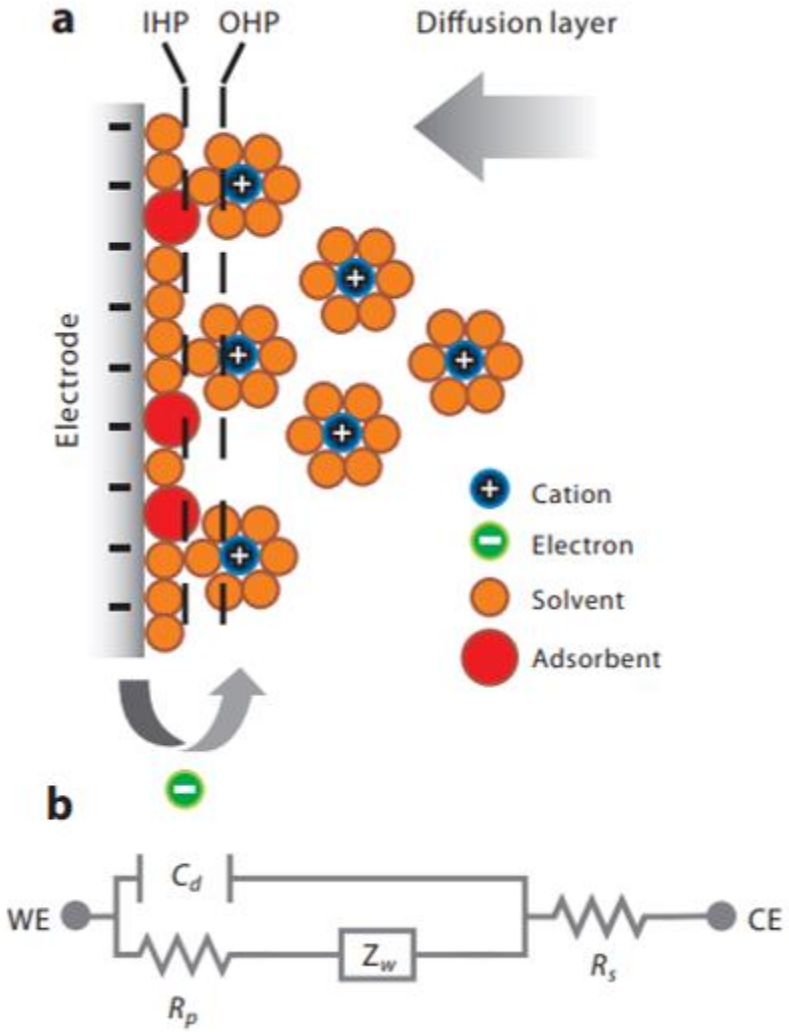

Figure 2.32: a) At top is an electrified interface in which the electrode is negatively charged; countercations are aligned along the electrified surface. At bottom are the electrical circuit elements corresponding to each interface component. (b) An idealized Randles EEC for the interface, shown with no specifically adsorbed anions. The high-frequency components are shown on the left, and the low-frequency components are shown on the right. Abbreviations: C_d, double-layer capacitor; WE, working electrode, CE, counter electrode; IHP, inner Helmholtz plane; OHP, outer Helmholtz plane, Zw, Warburg impedance [180].

The mass transport of the reactants and the products provides another class of impedance (Z_W), which can be exploited by electroanalytical chemists because it shows up in the form of a peak current in a voltammogram or a current plateau in a polarogram. The EEC in *Figure 2.32b* shows that each circuit component corresponds to each interfacial component. The EEC first proposed by Randles, displays both the high-frequency components (e.g., R_s) and the low-frequency components (e.g., Z_W). The left-to-right arrangement of the EECs is important because the impedance data are normally displayed in this manner. Also, note that the activation barrier at any potential is represented by the *polarization resistance*, R_p, but that barrier becomes the *charge-transfer resistance*, R_{ct}, at the standard (or formal) electrode potential.

Cyclic voltammetry (CV) is often preferred rather than EIS for the study of electrochemical steps coupled with chemical reactions, whose kinetics can be measured by varying the potential scan rate [182]. In contrast to cyclic voltammetry where the entire potential domain is scanned at a given scan rate, EIS offers the unique advantage of being able to perform measurements at different potentials. Cyclic voltammetry and EIS are therefore complementary techniques, and the choice of which technique is best to use depends on the process that each user is seeking to characterize.

EIS is a type of *transfer-function measurement*, commonly used in the analysis of linear time-invariant systems. In the case of an electrochemical system, the main difficulty is that the system must remain in a stationary state throughout the measurement. EIS uses a small-amplitude potential or current periodic perturbation to excite the electrochemical system at different frequencies. By measuring the response (current or potential) of the system to this perturbation, a transfer function is calculated which is the *electrochemical impedance of the system* in the case of an electrochemical cell. The impedance, Z, can be expressed as:

$$Z(\omega) = \frac{\tilde{V}(\omega)}{\tilde{I}(\omega)} = \left|\frac{\tilde{V}(\omega)}{\tilde{I}(\omega)}\right| [\cos\varphi(\omega) + i \cdot sin\varphi(\omega)] = Z'(\omega) + i \cdot Z''(\omega), (Eq. 2.13)$$

where ω is the angular frequency related to the frequency f (in Hz) by $\omega = 2\pi f$, φ is the phase angle between the input and output signal, and $i = \sqrt{-1}$ is the imaginary number.

The variable $\tilde{V}$, and $\tilde{I}$ are phasors, which are complex time-invariant numbers that account for the amplitude and phase of a sinusoidal function. The electrochemical impedance, as defined by *Eq. 2.13*, is a frequency-dependent complex number, whose real part, $Z'(\omega)$, is a *frequency-dependent resistance* and imaginary part,· $Z''(\omega)$, is a frequency-dependent reactance. The impedance differs from the resistance since the resistance observed in DC circuits obeys Ohm's Law directly.

The first step towards data analysis is the use of graphical methods to visualize and interpret the impedance data. To emphasize a specific feature or behavior, impedance data need to be presented in different formats that include the *Nyquist representation* for mass transfer and kinetic behavior; the *Bode representation* for frequency-dependent behavior; the *admittance format* for capacitive behavior at high frequency; and the *complex-capacitance* format for capacitive behavior of a dielectric system.

The impedance expression is divided into a real part and an imaginary part. When the real part, $Z'(\omega)$, is plotted on the X-axis, and the imaginary part· $Z''(\omega)$ is plotted on the Y-axis, a "Nyquist Plot" is formed (*Figure 2.33a*). Each point on the Nyquist plot is an impedance value at a frequency point, while the $\cdot Z''(\omega)$ is negative. At the X-axis, impedance at the right side of the plot is conducted with low frequency, while, at the higher frequencies, their generated impedances are exerted on the left. Moreover, on a Nyquist plot, impedance can be represented as a vector (arrow) of length |Z|. The angle between this arrow and the X-axis is called the "phase angle".

Another way to express the impedance results is to use what is called a *Bode plot*, which is very common in the engineering community compared to the Nyquist plot, where the Bode plot comprises two separate logarithmic plots: magnitude vs. frequency and phase vs. frequency (*Figure 2.33b*). In general terms, Bode plots are used for evaluating the capacitive systems, while the Nyquist plots are typically used for analyzing the resistive processes [183].

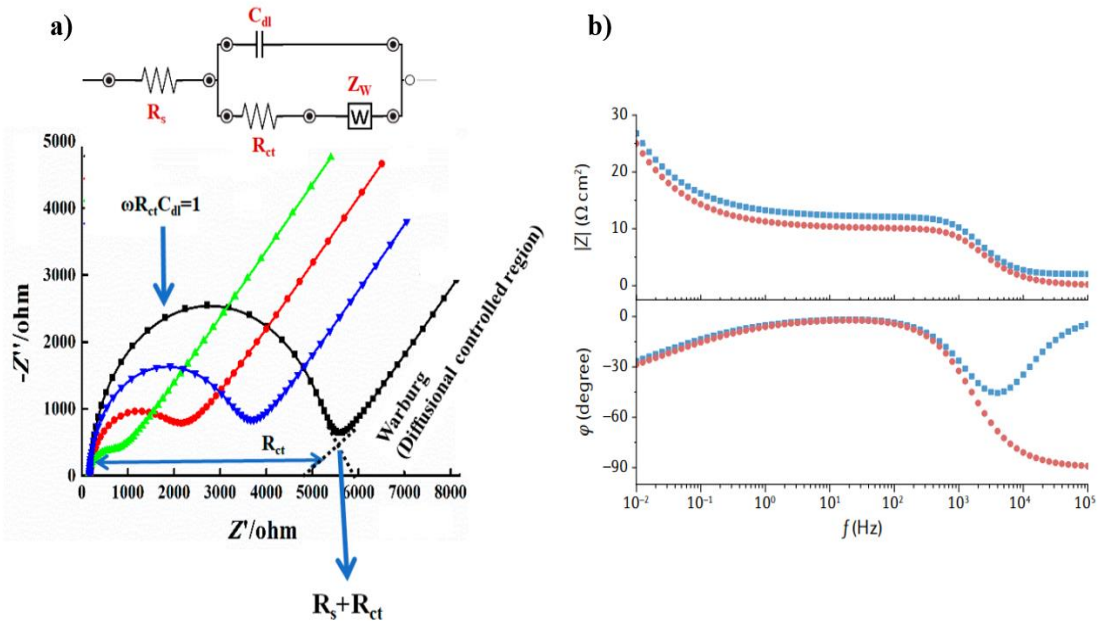

Figure 2.33: a) Nyquist representation of a Randles EEC: imaginary part of impedance, as a function of the real part in a complex plane with frequency as a parameter (left) [181]. b) Bode representation: modulus and phase of impedance as a function of frequency (right) [183].

The total impedance of an equivalent circuit is calculated by Kirchhoff's laws where Z is treated as a resistance. Therefore, the total impedance Z(ω) of a Randles circuit is shown in *Eq 2.13*. The real and imaginary components of Z(ω) are then solved algebraically. Even for the simple Randles circuit, $Z'(\omega)$ and $\cdot Z''(\omega)$ are quite complicated functions.

$$Z(\omega) = R_s + \frac{R_{ct}}{1 + i\omega R_{ct} C_{dl}} = Z'(\omega) + i \cdot Z''(\omega), \qquad (Eq. 2.13)$$

where the Warburg impedance, Z_w, has not been included in the above relationship.

2.8.2 Experimental Set-up

All experiments were carried out at room temperature, T = 23 ℃, in a three-compartment cell (three-electrode set-up), filled with 100 mL triple distilled water containing 0.1 M NaOH ($pH = 13.5$) for alkaline media measurements. An Ag/AgCl (3 M KCl) electrode (Metrohm A.G.) was used as the reference electrode and a Pt-wire electrode as the counter electrode. As a working electrode a Fluorine doped tin oxide (FTO) glass substrate was used, where the electrocatalytic materials were deposited as drop-casted films.

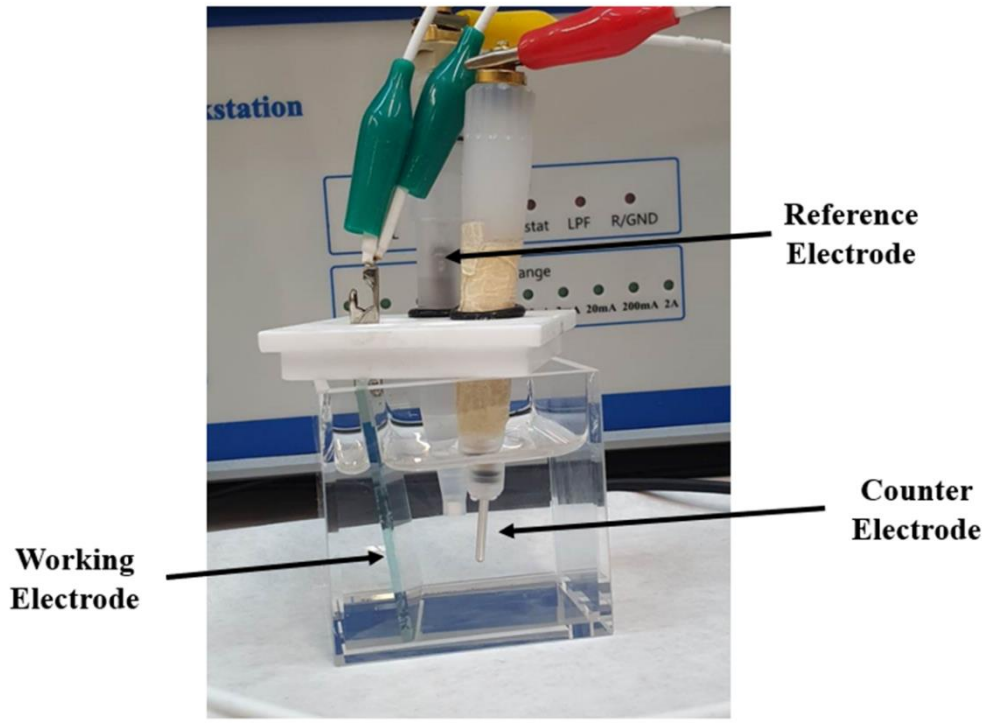

Figure 2.34: Photograph of the three-electrode set-up used in current thesis.

The three-electrode setup, shown in *Figure 2.34*, is the most common type of electrochemical cell system widely used in the field of electrochemistry. This system consists of a *potentiostat*, with the help of which a constant voltage is applied or a current is supplied to the system, depending on whether its desired function is potentiostatic or galvanostatic respectively, a *Working Electrode* (W.E), on which the material under study is deposited, an *Auxiliary/Counter Electrode* (C.E) to supply current to the work and a *Reference Electrode* (R.E) to impose the desired potential difference - voltage. With the help of a computer and using appropriate software, the experimental results are obtained. The difference in potential is controlled between the counter and the working electrode and is measured as a function of the reference electrode (Ag/AgCl). The potential between C.E. and W.E. is usually not measured. The system is constructed in such a way that the potential difference between W.E and R.E is the voltage that the operator applies to the system. This happens essentially via the potentiostat, applying a potential difference between C.E and W.E, the value of which each time depends on the voltage applied between the W.E and R.E.

2.8.3 Preparation of Electrocatalytic Electrodes

The electrocatalytic materials were deposited as drop-casted films, on Fluorine Tin Oxide (FTO) substrates as a working electrode (Fluorine doped tin oxide coated glass slide Sigma-Aldrich, Saint Louis, MO, USA) with a 50 mm x 50 mm x 2.2 mm dimensions (with a geometric surface area of 25 cm^2) and surface resistivity of $\sim 7\ \Omega/\mathrm{sq}$. To construct the electrode, first, a catalyst-suspension was prepared containing 15 mg of the material-powder in a 6 mL mixture of triple distilled water (2.75 mL) and isopropanol (3.25 mL) (Merck, ACS Reag, NJ, USA). Depending on the experiment, the catalyst powder was either Pt^0-particles, or FSP-made Cu:$NaTaO_3$ particles.

Before the drop-casting step, the catalyst mixture was ultrasonicated using a 20 W ultrasonication bath (Elmasonic S10 h, Singen, Germany) to achieve a homogeneous slurry. Deposition of each electrocatalyst material on the working electrode was performed by drop-casting of the prepared suspension onto the FTO substrate glass. Then, 2 mL of the catalyst suspension was drop-casted onto the glassy carbon, using a micro-pipette (100 μL per drop), and rapidly dried at room temperature at 9000 rpm, forming a dry catalyst film. Then, 20 μL of Nafion-solution was drop-casted on the formed film and allowed to dry at room temperature, forming a dry {Nafion: catalyst} film on the glassy carbon. The Nafion solution consisted of 5 wt.% perfluorinated Nafion resin solution (Sigma Aldrich, MO, USA), in triple distilled water/isopropanol (110 μL Nafion solution: 5.5 mL triple distilled water: 6.5 mL isopropanol). According to the standard procedure, the deposition of a Nafion on top of the catalyst film acts as a binding agent [184] stabilizing the electrode.

So far, platinum/carbon (Pt^0/C) is the most promising candidate for Hydrogen Evolution Reaction (HER) and Oxygen Evolution Reaction (ORR), in both alkaline and acidic media, due to their good electrocatalytic activity and stability. However, the high-cost and environmental scarcity of Pt are prohibitive factors, thus, low-cost/earth-abundant metal oxide catalysts are in immediate need. Moreover, the properties of the carbon support, i.e., such as graphitization quality, conductivity, O_2 diffusion, and surface area affect the activity and catalyst's durability.

Chloroplatinic acid hexahydrate ($H_2PtCl_6 \cdot 6H_2O$, Sigma-Aldrich, Saint Louis, MO, USA), Sodium Borohydride ($NaBH_4$), used to form the Pt nanoparticles were purchased from Sigma Aldrich (Saint Louis, MO, USA). Carbon black (Vulcan XC-72R) was a kind gift from Cabot (Boston, MA, USA), and was used as-received as the support of the electrocatalysts.

Pt^0-particles were synthesized as a reference catalyst, employing the wet-impregnation method [185], based on the formation of fine Pt^0 particles via the reduction of Pt^{2+} by BH_4. Briefly, 85 mg of the Pt-salt was dissolved in 8 mL of ultra-pure triple distilled water (Millipore SIMS600 CP Burlington, USA) at room temperature, $T = 23$ ℃, plus 160 mg of Vulcan XC-72 R carbon black. The mixture was allowed to mix under continuous stirring for 2 hours until it became a homogeneous black slurry. Then, $NaBH_4$ was added dropwise to the Pt/carbon slurry, using a 10 μL pipet, at a rate of 1 mL/min under vigorous stirring. The $NaBH_4$ was taken from a stock of 31 mg $NaBH_4$ dissolved in 8 mL of triple distilled water. The reduction potential of the $NaBH_4$/Pt/carbon slurry was $E_h = -65$ mV vs. NHE [186], monitored in situ by a redox Pt-electrode (Metrohm, Pt Working Electrode 3 mm diameter Herisau, Switzerland). Then, the resulting $NaBH_4$ /Pt/carbon slurry was heated under stirring for 12 hours at 90 ℃, and afterward, the formed solid residue was collected by centrifugation at 8000 rpm. The collected solid was dried for 12 h at 23 ℃ under an N_2 stream. This material, herein codenamed as {20% w/w Pt/C}, had a Pt-loading of 20.2% as determined by X-Ray Fluorescence.

Chapter 3

Results-Discussion

3.1 Synthesis and Characterization of Cu:$NaTaO_3$ nanoparticles

Utilizing the adaptability and versatility of the FSP technology, which is described in detail in the previous chapter, in this paragraph the flame-made nanoparticles with different Cu loading configurations are demonstrated, along with their FPS parameters.

3.1.1 FSP Parameters and Crystal Structure

In Flame Spray Pyrolysis, the ratio *P/D*, i.e., the feed rate of liquid precursor (*P*) over the feed rate of dispersion O_2 gas (*D*), is a key parameter determining the nanocrystal formation process. Having prepared a homogeneous and opaque solution containing $0.3\,M\,TaCl_5$ and $0.3\,M\,C_8H_{15}NaO_2$, it is fed into the syringe. The combustion parameters used are gathered in detail in *Table 3.1*.

Table 3.1: Flame Spray Pyrolysis parameters used for the synthesis of nanoparticles.

Sample ID	Characteristics	Cu^{2+} loading (% w/w)	Total Precursors Concentration (mol/L)	Pilot Flame O_2/CH_4 (L/min)	Precursor feed rate (mL/min) / Dispersion O_2 (L/min)	Sheath O_2 (L/min)	Precursor feed rate (mL/min) / Flow rate N_2 (L/min)	d_{XRD} (nm)
3450	$NaTaO_3$	-	0.6	2/1	5/5	10	5/12	21
3487	Cu^{2+} single atoms deposition	0.05						14
3488		0.1						14
3489		0.5						14
3491		1						13
3490		2.5						14

The FSP reactor Set-up was thoroughly investigated to achieve the optimal Set-up for that specific purpose. The only variable of the system is the Cu loading which increases gradually, calculated in terms of the molarity of the perovskite. All the other parameters remain constant, which suggests, according to *FSP* technology, that the particle diameters should be in proximity, calculated from the *XRD* patterns. Sheath gas (O_2) was constantly fed to the burner to ensure a high-temperature zone presence which allows longer residence times in the flame zone and protection of the particle formation pathway. The precursor feed rate, the dispersion of oxygen gas, as well as the premixed pilot O_2/CH_4 flame, has been previously established, and any detail is outside the scope of this thesis. After collecting the powder by scraping it from the glass fiber filter, the particles were stored in glass vials under the influence of Argon gas (Ar). *Figure 3.1* shows the samples that were synthesized in one step process without any pretreatment needed.

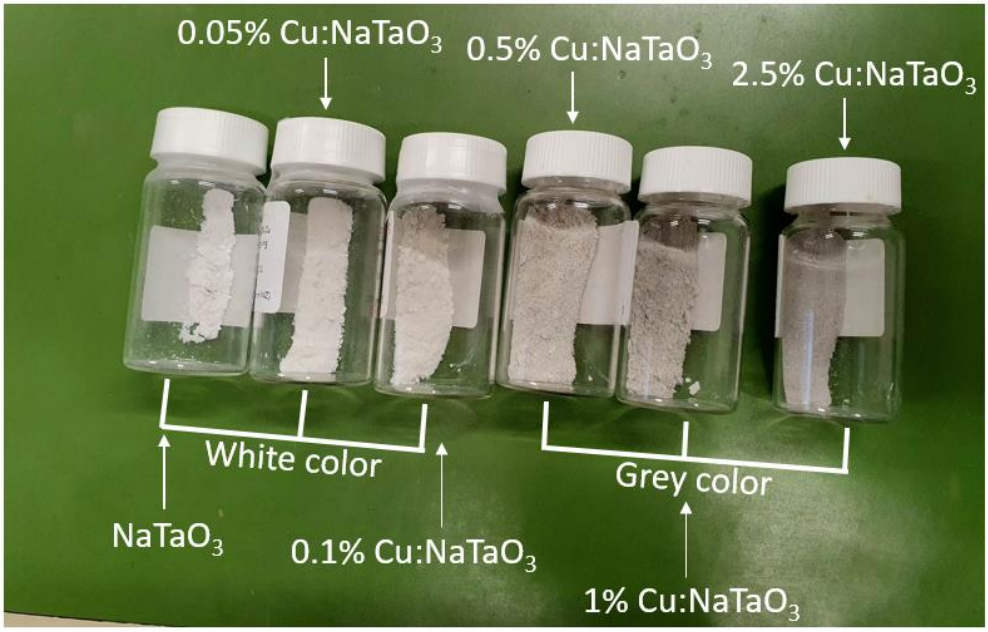

Figure 3.12: Nanoparticles produced via Flame Spray Pyrolysis technology.

In *Figure 3.1*, from left to right the content of Cu increases. It is observed that at low concentrations (0.05% and 0.1% Cu) the collected powder is white in color and crispy, just as expected for $NaTaO_3$ nanoparticles. As the loading of Cu increases, the color changes to gray and the texture becomes smoother. This is a visual indication that at high concentrations (0.5%, 1%, and 2.5%) Cu (or CuO) particles have formed, hence the change in color.

X-Ray Diffraction was used to study the crystal structure of the nanomaterials. *Figure 3.2* presents the XRD pattern of flame-made nanoparticles listed in *Table 3.1*. The crystal size is calculated by the *Scherrer equation* (*Eq. 2.2*). A multi-peak Lorentzian fitting was used to study the variability of the linewidth of the peaks. It turns out that the final d_{XRD} $\left(\text{or } d_{spacing}\right)$ did not change dramatically in the different lattice planes, a fact that agrees with the spherical symmetry of the particles. Highly crystalline Cu: $NaTaO_3$ nanostructures were synthesized with a constant particle diameter of about 14 nm. The constant particle size proves that Cu has *not been incorporated into the perovskite lattice* but has been deposited on its surface.

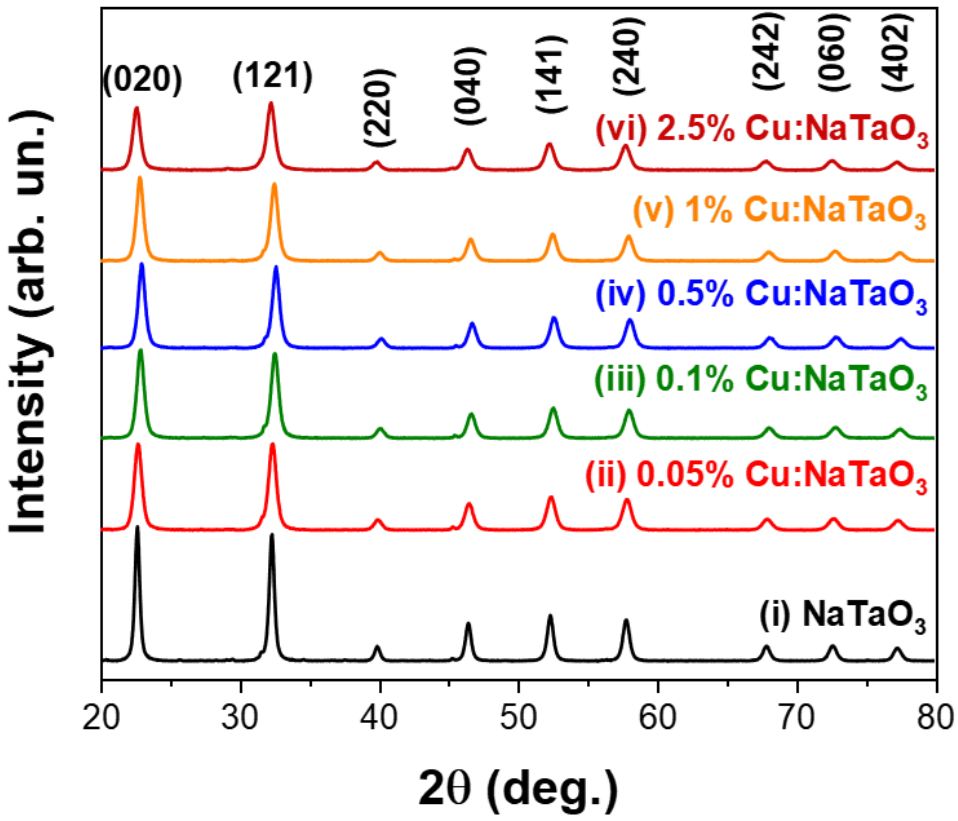

Figure 3.2: XRD patterns of flame-made nanoparticles. The black line corresponds to (i) $NaTaO_3$ perovskite structure. The red, olive, blue, orange, and burgundy lines correspond to (ii) 0.05%, (iii) 0.1%, (iv) 0.5%, (v) 1%, and (vi) 2.5% Cu single atoms deposition, respectively.

The phase analysis of the nanostructures was done using *DIFFRAC. EVA* and *Total Pattern Analysis Solution (TOPAS)* globally used line-fitting software specialized for the analysis of diffraction data and are based on the *Rietveld method*. The Bragg diffraction peaks correspond to (020), (121), (220), (040), (141), (240), (242), (060), and (402) crystal planes of $NaTaO_3$ perovskite structure. The peaks correspond to the *cubic lattice* with $a = b = c = 3.93$ Å (JCPDS card no. 74-2488).

No indication of the presence of a diffraction peak corresponding to Cu (or CuO) appears to emerge. Furthermore, there is a very small percentage ($< 1\%$) corresponding to the existence of NaCl salt, which is not visible to the naked eye. The diffraction peaks and their corresponding diffraction angles are presented in *Table 3.2*.

Table 3.2: Number of diffraction peaks, diffraction angles (2θ) and their corresponding planes.

Diffraction Peaks	2θ (deg.)	Diffraction planes
1	23	(020)
2	32	(121)
3	40	(220)
4	46	(040)
5	52	(141)
6	58	(240)
7	68	(242)
8	73	(060)
9	77	(402)

Through the identification of the diffracted crystal planes, one concludes that the desired nanostructure, having high crystallinity, has been successfully formed. The formation of individual oxides (Ta_2O_5 *and* Na_2O) from the 2 precursor solutions has been avoided, indicating the stability of the perovskite structure. Copper detection was not achieved, which will be done below through surface techniques.

3.1.2 Surface Structure

The XPS analysis was carried out to study the surface chemical compositions and states. All binding energies are corrected by the C 1s signal at 284.5 eV, shown in Figure 3.3. After measuring all the produced materials, only the highest percentage of the deposited Copper was able to be recovered from the XPS measurement. Figure 3.3 displays the survey spectra of the sample 2.5% Cu:$NaTaO_3$.

It clearly shows that the sample is mainly composed of Na, Ta, and O elements without other impurities, excluding adventitious carbon-based contaminants. Furthermore, it shows the existence of Copper atoms, but the measurement resolution isn't ideal to study the state of Cu upon the perovskite structure. It should be emphasized at this point that the deposited content of Cu atoms is a *nominal value* and perhaps the actual value is less than it is considered to be.

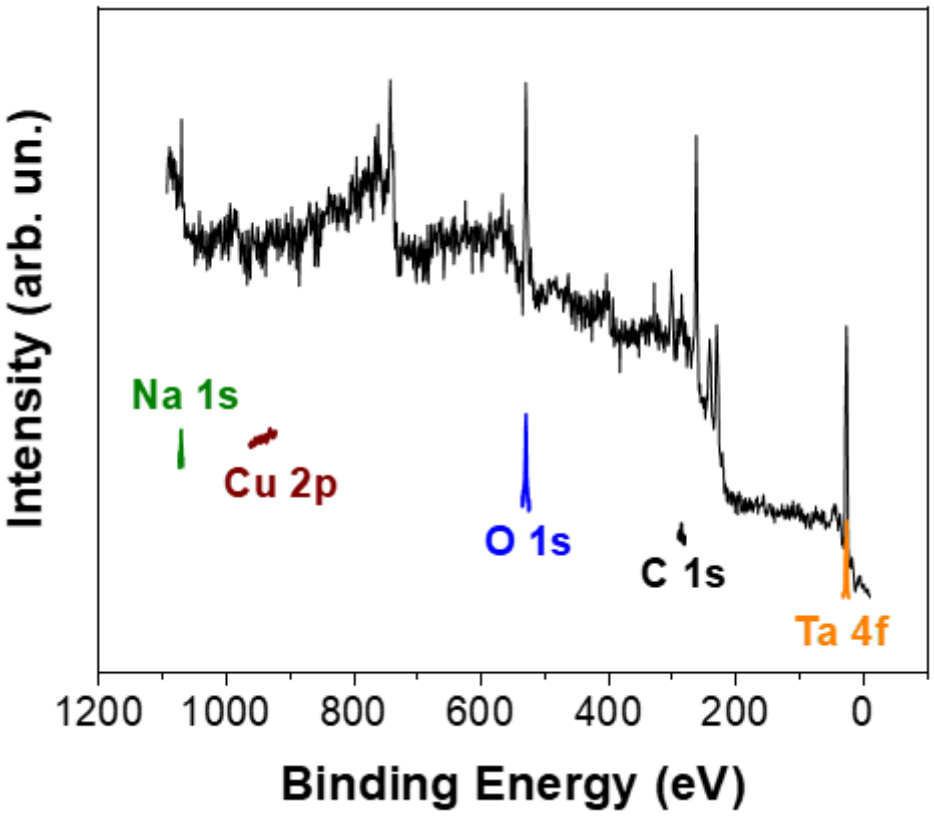

Figure 3.3: XPS survey spectrum measured for the sample with the highest Cu loading (2.5% Cu nominal).

The Ta 4f spectrum in *Figure 3.4* displays two primary bands at 25,9 and 27,8 eV, indicating a characteristic of Ta^{5+} in $NaTaO_3$ [187]. The characteristic Na 1s binding energy of 1071 eV, shown in *Figure 3.5*, confirms the presence of Na atoms in the $NaTaO_3$ structure [188].

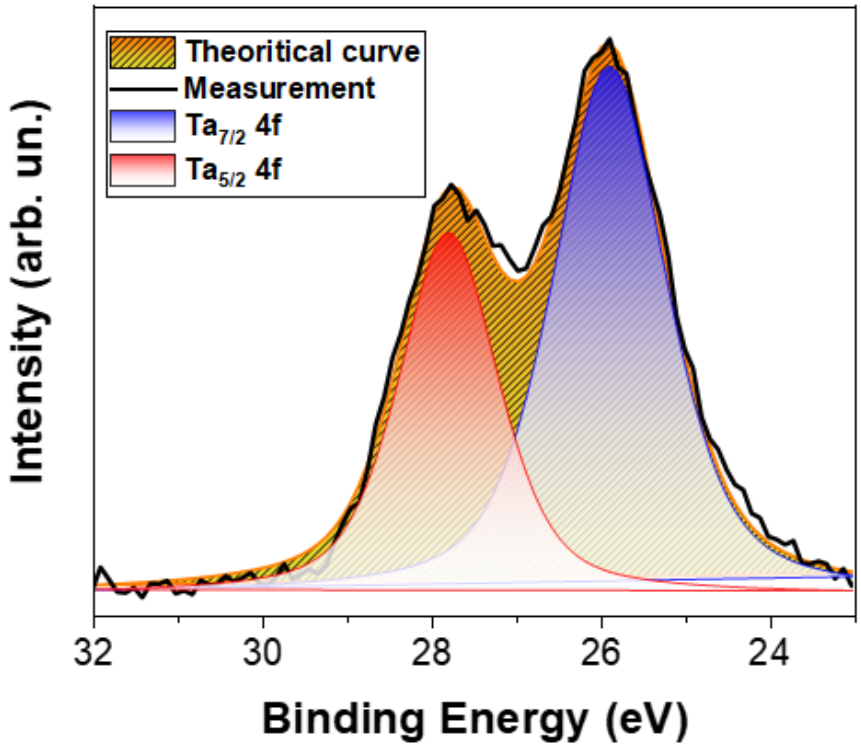

Figure 3.4: XPS spectrum of Ta 4f. With a black line is shown the experimental spectrum, after the carbon peak correction. With yellow filling and diagonal complementary lines, the theoretical curve is composed. Characteristic bands $Ta_{5/2}{}^{5+}$ and $Ta_{7/2}{}^{5+}$ are depicted with red and blue filling, respectively.

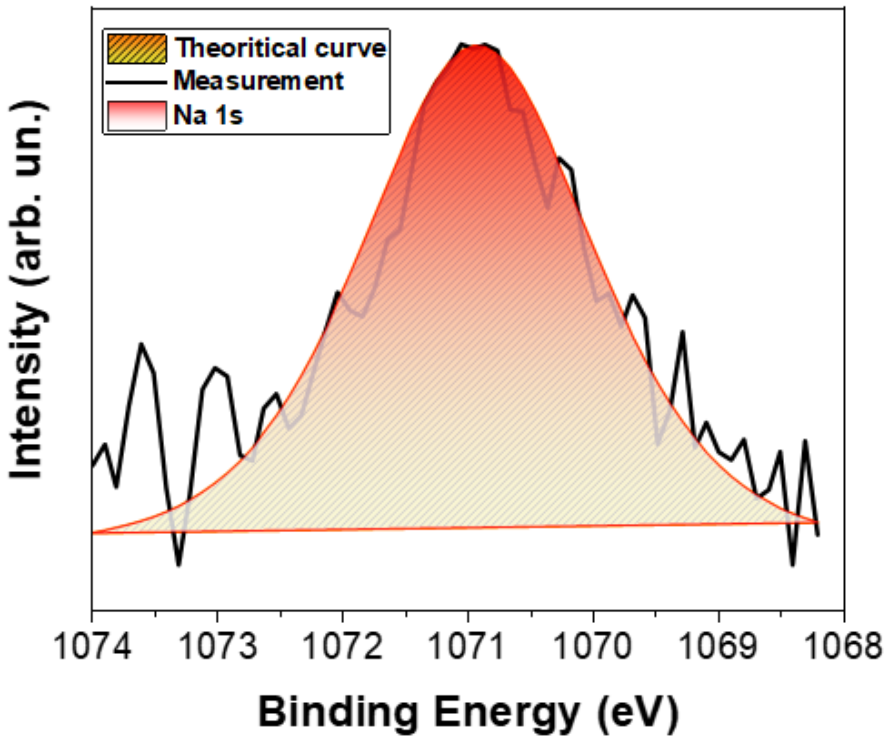

Figure 3.5: XPS spectrum of Na 1s. With a black line is shown the experimental spectrum, after the carbon peak correction. With yellow filling and diagonal complementary lines, the theoretical curve is composed. The characteristic peak of Na 1s is depicted with red filling.

The Ta spectrum shows the distinct $Ta_{5/2}{}^{5+}$ and $Ta_{7/2}{}^{5+}$peaks. Reduced Ta states as Ta^{4+}, Ta^{3+}, and/or Ta^{0} were absent in the XPS spectra [188]. The oxygen spectrum, shown in *Figure 3.6* contains characteristic peaks at 531 eV, assigned to surface hydroxyl groups, and 529 eV, assigned to the O-Ta bonds of the crystal. Overall, the XPS data confirm the $NaTaO_3$ structure, without oxygen defects or reduced Ta atoms.

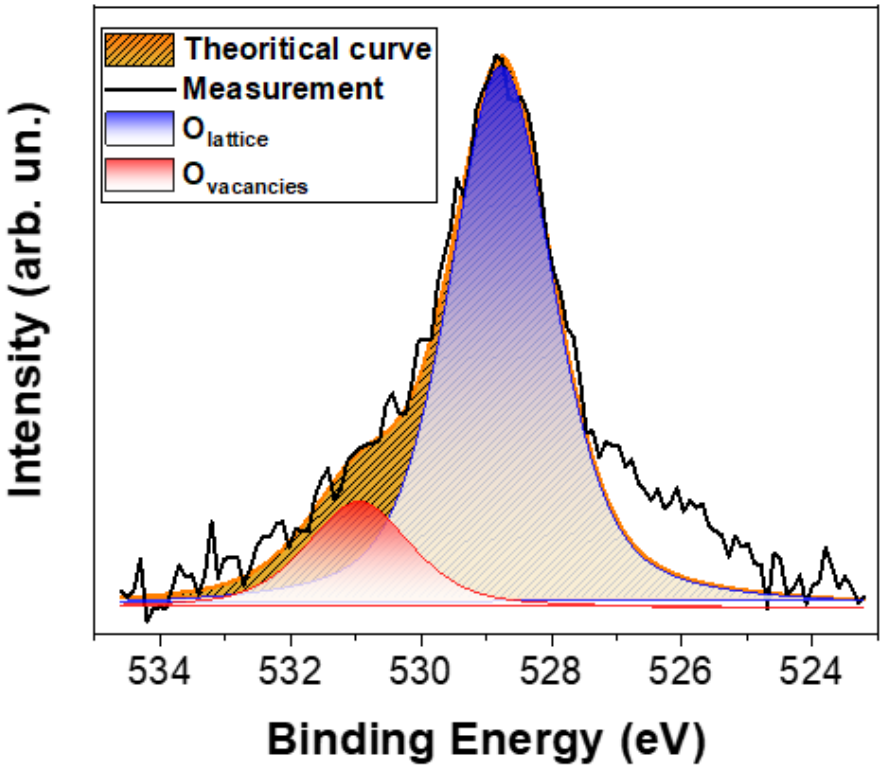

Figure 3.6: XPS spectrum of O 1s. With a black line is shown the experimental spectrum, after the carbon peak correction. With yellow filling and diagonal complementary lines, the theoretical curve is composed. Characteristic bands assigned to surface hydroxyl groups and O-Ta bonds of the crystal are depicted with red and blue filling, respectively.

From a physical point of view, there is no possible explanation that argues for the existence of a different origin of oxygens, which are detected at 525-527 eV. Therefore, in that region where the fitting is not completely ideal, there has either been an experimental error or an error in the data processing.

High-resolution XPS has not been used in the Copper detection measurement. Nevertheless, in *Figure 3.7* can be identified two primary bands at 932, and 952 eV, indicating the distinct $2p_{3/2}$ and $2p_{1/2}$, respectively.

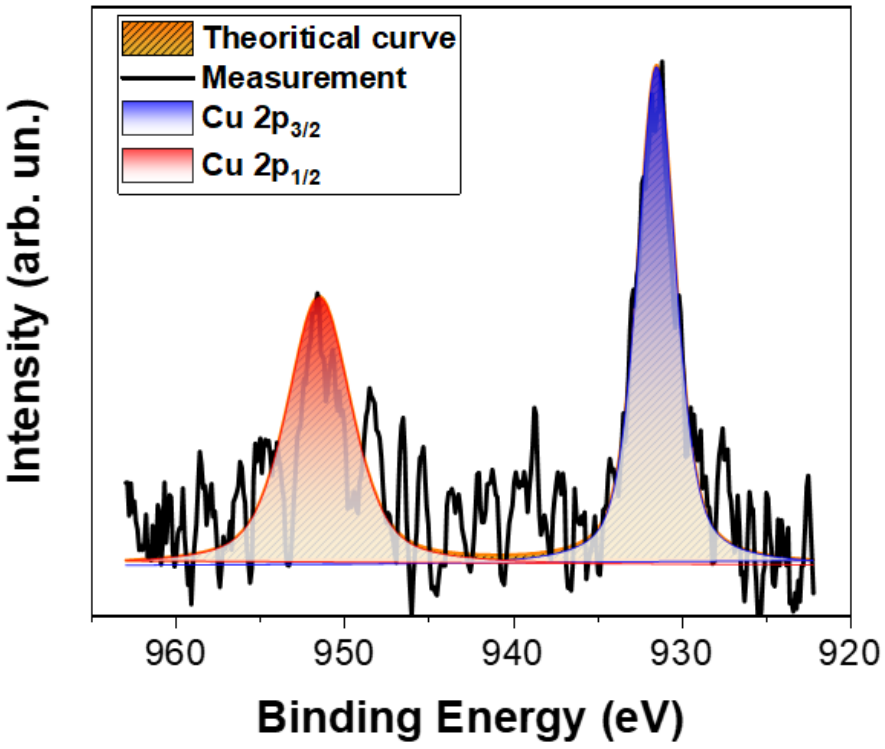

Figure 3.7: XPS spectrum of Cu 2p. With a black line is shown the experimental spectrum, after the carbon peak correction. With yellow filling and diagonal complementary lines, the theoretical curve is composed. Characteristic bands $Cu\ 2p_{1/2}$ and $Cu\ 2p_{3/2}$ are depicted with red and blue filling, respectively.

Poulston et al. [189], in their study of surface oxidation and reduction of Cu_2O and CuO, have used both the Cu LMM and the Auger parameter to distinguish Cu^0, Cu^{1+} and Cu^{2+}. These parameters are very useful for the identification of the different states present on the surface, but they are difficult to quantify as relative amounts of each species. The Cu 2p XPS spectrum is still the signal most used for this purpose. In this analysis, a statistical separation of the $Cu\ 2p_{3/2}$ peak position for Cu^0 and Cu_2O is achieved. This should be expected, as most spectrometer calibration procedures include referencing the ISO standard Cu metal line at 932.63 eV with a deviation of this line set at ± 0.025 eV. Curve-fitting of the $Cu\ 2p_{3/2}$ line for both Cu metal and Cu_2O employed Gaussian (10%) - Lorentzian (90%) and Gaussian (20%) - Lorentzian (80%) peak shapes, respectively (defined in WinSpec). *None of the above assumptions* results in an ideal fitting. The best case is achieved by employing Gaussian (2-3%) - Lorentzian (97-98%), which is due to the slight broadening of the peak as shown in *Figure 3.7*. Therefore, it was not possible to achieve the deconvolution of the $Cu\ 2p_{3/2}$ peak and thus the ration Cu^0/Cu^{2+} can't be properly found, but as the Lorentzian curve prevails, its value will be close to zero.

3.1.3 Porus Analysis

Brunauer – Emmett – Teller (BET) analysis was implemented to determine the specific surface area (SSA) of the flame-made nanoparticles. *Table 3.3* lists the values of the SSA, d_{BET} resulting from *Eq. 2.4*.

Table 3.3: Specific Surface Area, d_{BET}, and comparison with the d_{XRD} of the flame-made nanoparticles.

Sample ID	Characteristics	Cu^{2+} loading (% w/w)	Specific Surface Area (m^2/g)	d_{BET} (nm)	d_{XRD} (nm)
3450	$NaTaO_3$	-	44	19	21
3487	Cu^{2+} single atoms deposition	0.05	57	15	14
3488		0.1	58	15	14
3489		0.5	55	15	14
3491		1	62	14	13
3490		2.5	56	15	14

The specific surfaces of the nanostructures on which the Cu has been deposited have values of $55 - 62\ m^2/g$ and corresponding d_{BET} between $14 - 15\ nm$. These values are in close proximity to the d_{XRD} (*Table 3.1*) and therefore there is an agreement between the two techniques. Large values in specific surface area correspond to smaller particle diameters. This means that the surface-to-volume ratio increases. Therefore, there are more surface sites where they can be active in catalytic reactions, which goes hand in hand with the use of working materials. So, it is of great importance for the produced nanomaterials to have a large surface area.

Figure 3.8 shows the isotherm measurements for the materials: (i) $NaTaO_3$, (ii) 0.05% Cu:$NaTaO_3$, and (iii) 0.1% Cu:$NaTaO_3$, respectively, to get an insight into the porus radius. This correlation is made through the study of the change in specific volume. A sharp increase and then decrease in volume corresponds to the existence of pores, which range in similar spatial dimensions.

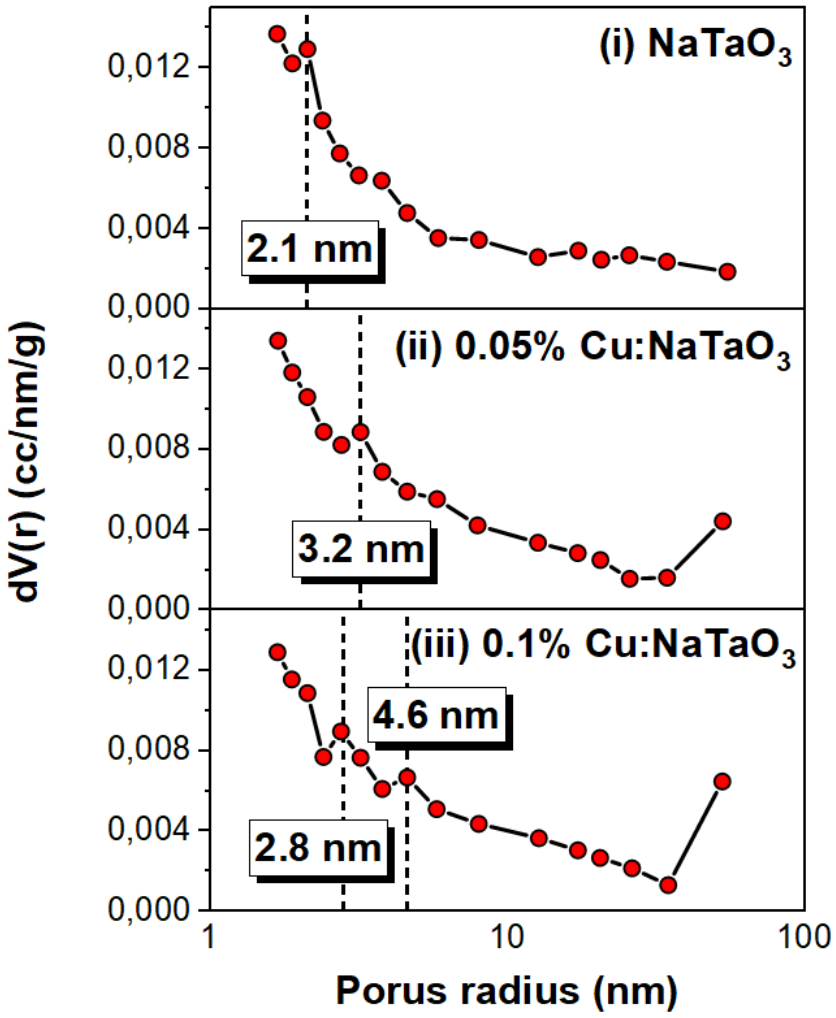

Figure 3.8: Porus radius distribution for the materials: (i) $NaTaO_3$ (top), (ii) 0.05% Cu:$NaTaO_3$ (middle), and (iii) 0.1% Cu:$NaTaO_3$ (bottom).

It appears that these 3-materials exhibit nano-pores with dimensions of $2-4\,nm$. Therefore, the materials are not particularly porous but have a large specific surface area. *Figure 3.9* shows the isotherm measurements for the materials with a higher loading of copper.

It is observed that there is a redistribution of pore size as the percentage of copper increases. As the Cu is converted from monomeric to particles the pores grow in size and have a radius of $17-18\,nm$, and $35\,nm$.

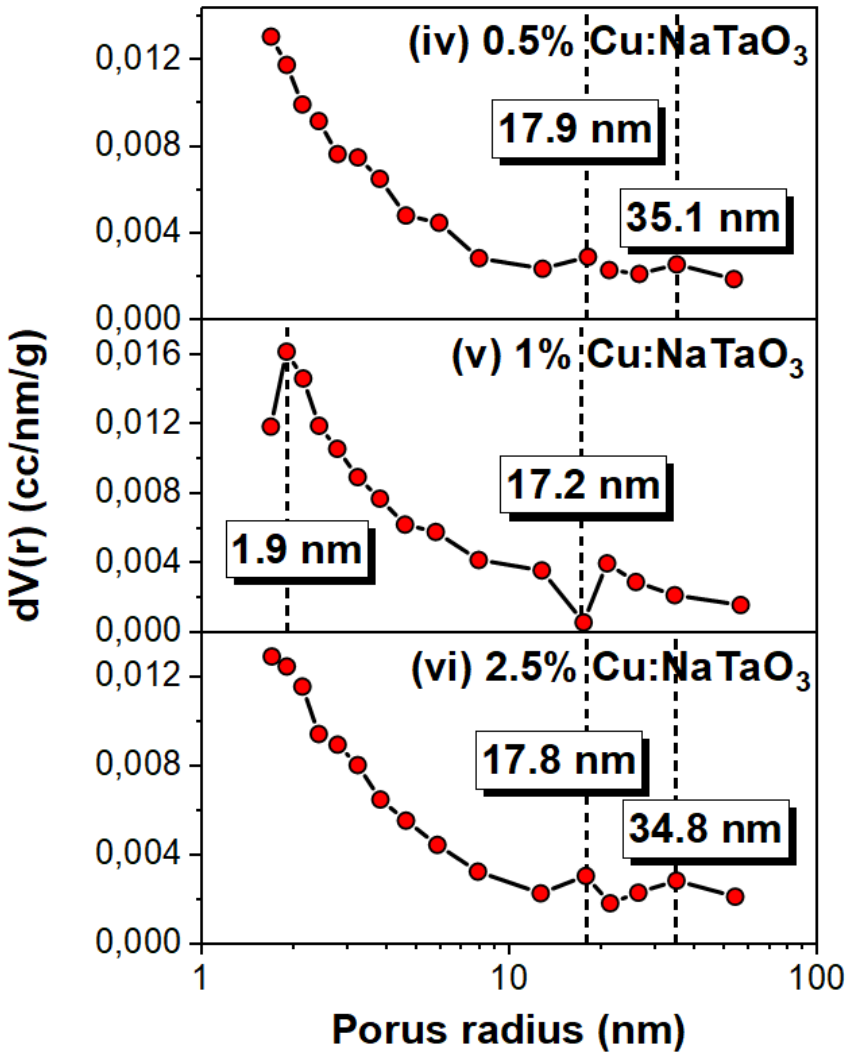

Figure 3.9: Porus radius distribution for the materials: (iv) 0.5% Cu:$NaTaO_3$ (top), (v) 1% Cu:$NaTaO_3$ (middle), and (vi) 2.5% Cu:$NaTaO_3$ (bottom).

In summary, through the techniques analyzed so far stable Cu:$NaTaO_3$ nanostructures, with a high degree of crystallinity and a high value of specific surfaces have been successfully produced. Tantalum is not in any oxidation state beyond the expected (Ta^{5+}), and the presence of copper has been identified, as has its valence (Cu^{2+}) by X-Ray Photoelectron Spectroscopy.

In the next paragraph, the vibrational modes using Raman spectroscopy and the optical properties using UV-Vis Diffuse Reflectance Spectroscopy are analyzed.

3.2 Vibrational Modes and Optical Properties

The $NaTaO_3$ Raman spectra can be divided into three internal modes in the range of $150 - 1000\ cm^{-1}$, presented in *Figure 3.10*. These are attributed to $O - 2Ta$ or $O - 3Ta$ deformation and stretching vibrational modes. [190,191]. Most importantly, the detection of the vibrations in $200 - 250\ cm^{-1}$, ensures that the materials do not have amorphous regions. $NaTaO_3$ possesses similar peaks with the Ta_2O_5 due to Ta–O groups, in accordance with literature data and theoretical calculations [192,193]. The lack of Raman phonons in the range of $1000 - 1500\ cm^{-1}$ indicates the absence of carbon-induced vibrational modes [194] which is important, showing that carbon-free materials are formed by the FSP process, meaning that during the FSP combustion process, carbons from the solvent and the metal precursor are completely combusted to CO_2, due to the high combustion enthalpy/ oxygen-rich process used in the present FSP protocols.

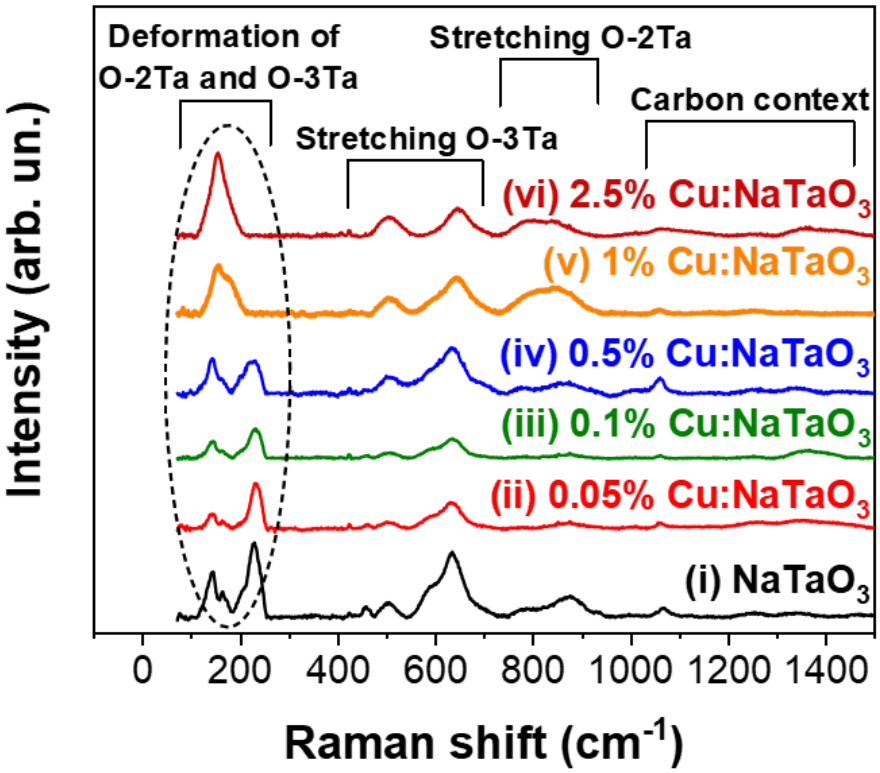

Figure 3.10: Raman spectra of the flame-made materials, with the assigned deformation/stretching vibrational modes of O-2Ta, and O-3Ta. The black line corresponds to (i) $NaTaO_3$ perovskite structure. The red, olive, blue, orange, and burgundy lines correspond to (ii) 0.05%, (iii) 0.1%, (iv) 0.5%, (v) 1%, and (vi) 2.5% Cu single atoms deposition, respectively.

Local arrangement in Ta_2O_5 was described using Ta-centered polyhedra: TaO_6 octahedron and TaO_7 pentagonal bipyramid, and TaO_8 hexagonal bipyramid. These polyhedra can be edge-sharing and corner-sharing, leading mostly to two-coordinated and three-coordinated oxygen configurations, referred to as $O-2Ta$ or $O-3Ta$, respectively. This variety of possible arrangements leads to an important bond distortion from one site to another.

Comparing the spectrum of the pure perovskite ((i) $NaTaO_3$) to those in which copper has been deposited, one notices that there are dramatic changes in the critical areas between $100-1000\ cm^{-1}$. Spectral regions were identified and assigned to specific vibrational modes: internal modes (Ta–O phonon modes) can be divided into three spectral regions in the $100-1000\ cm^{-1}$ range and contributions below 150 cm^{-1} are attributed to external modes. At this point, it should be emphasized that measurements of CuO and Cu_2O have been made (*Figure 3.11*) and the identification of the vibrational mode of Cu in the samples under study cannot be achieved.

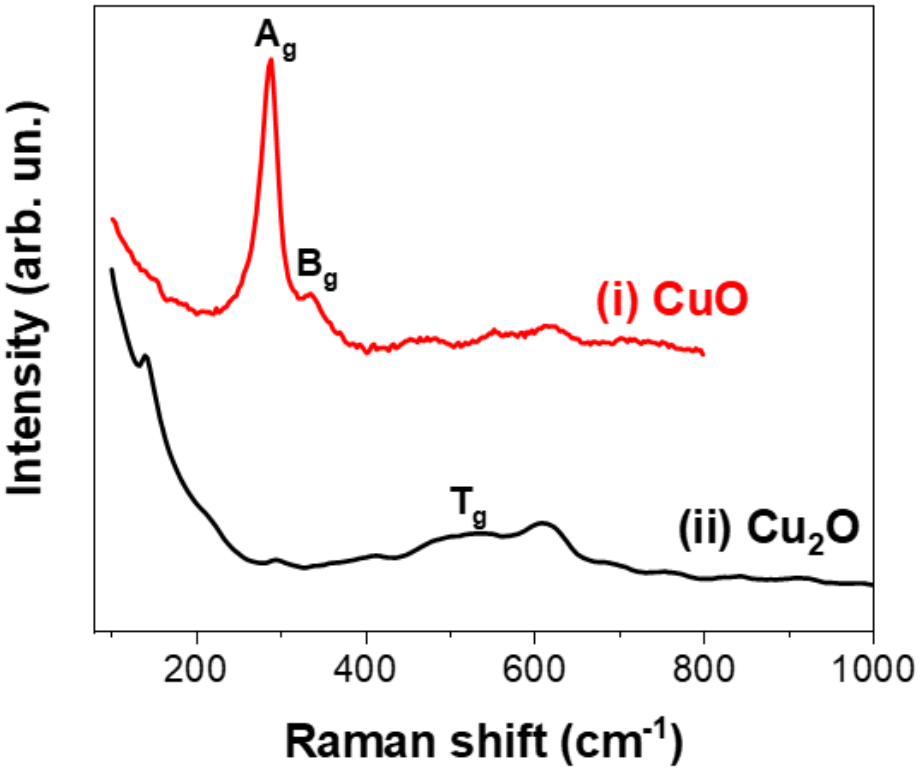

Figure 3.11: Raman spectra of (i) CuO (red line) and (ii) Cu_2O (black line).

Changes in the shape and intensity of the curves are observed in the three critical areas. In the first area $(100 - 250\ \mathrm{cm}^{-1})$ where according to the literature it is attributed to the deformation of $\mathrm{O} - 2\mathrm{Ta}$ and $\mathrm{O} - 3\mathrm{Ta}$ as the concentration of copper in the system increases, a gradual broadening of the two characteristic peaks is observed. As a final result, the two peaks are broadened so much that they are indistinguishable from each other. In the second region $(450 - 750\ \mathrm{cm}^{-1})$ there is a drastic change in the shape of the curve between the pure perovskite and the rest of the samples. The intensity of that area is quite high compared to the systems where Copper is present. But as its concentration increases, a gradual increase in intensity is observed. The same thing happens in the third region $(750 - 950\ \mathrm{cm}^{-1})$ where the intensity in that area is high in $NaTaO_3$ and as copper increases the intensity of the curve increases too.

Through the changes in the spectra in the above three regions the following conclusion is drawn. The formation process of the flame-made particles is not yet complete when they meet the cloud where the copper atoms are present. Thus, the deposition of copper on the perovskite brings about changes in its lattice. In $NaTaO_3$ perovskite in all 3 regions of the spectrum, the intensity is quite high and therefore these are intrinsically characterized by high deformation and stretching vibrational modes of $\mathrm{O} - 2\mathrm{Ta}$ and $\mathrm{O} - 3\mathrm{Ta}$. As copper is deposited there is a drastic change in the first region, while the other two increase in intensity. Therefore, increasing the concentration of copper affects the lattice structure and as copper atoms become nanoclusters, particles increase the order of the stretching of the bonds.

Cu – Ta interface

From the results of the Raman spectroscopy, one realizes that in this way *the in-situ monitoring of Strong Metal – Support Interaction (SMSI)* has been achieved. This interaction refers to the strong interaction between metal (Cu^{2+}) centers and the active surface of oxide support. The SMSI phenomenon [195] involves a delicate balance between the catalytic activity of the metal and its interaction with the support material. In the case of Cu^{2+} and perovskite oxides, the interaction leads to the formation of highly dispersed atomic Cu species on the oxide, which can act as highly active sites for various catalytic reactions. Additionally, is known in the literature that the SMSI effect can enhance the stability of the Cu particles on the surface, leading to improved durability of the catalyst and enhanced ability to selectively catalyze certain reactions.

From the point of view of particle formation, the drastic distortion of the $NaTaO_3$ surface was observed at the interface of the Cu nanoclusters with Tantalum. Assuming, according to the above, that the formation process of the perovskite is not complete, one can conclude that as the copper atoms increase inside the micron-sized droplet, part of them condenses and forms the nanoclusters, while another remains isolated and is deposited as single atom on the perovskite surface. The Cu nanoclusters cause a higher degree of distortion on the perovskite surface, shown in *Figure 3.12*.

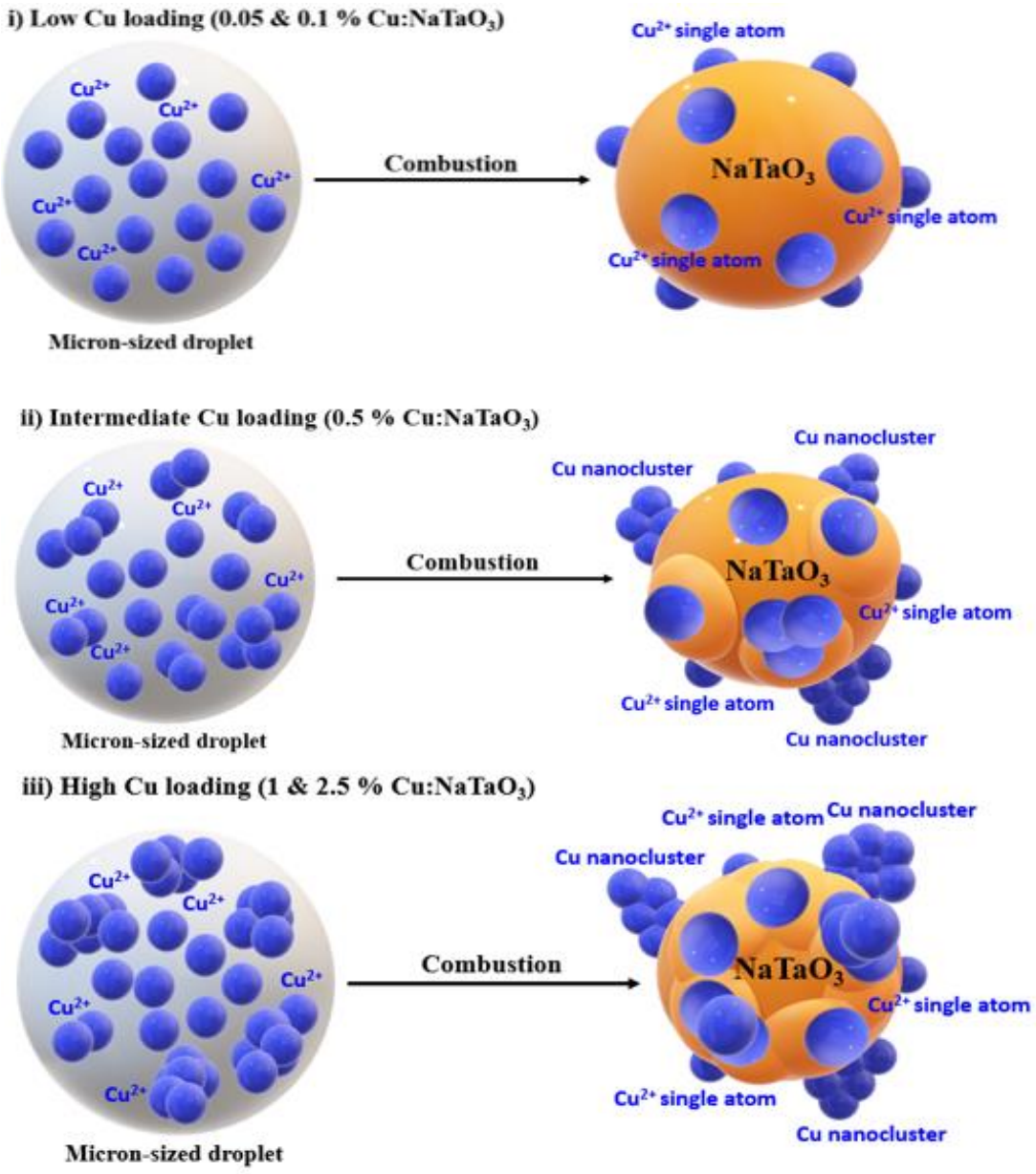

Figure 3.12: Schematic representation of the micron-sized droplet (left) and the flame-made nanoparticle for three categories in terms of copper loading: i) Low Cu loading (0.05 & 0.1% $Cu:NaTaO_3$) (top), ii) Intermediate Cu loading (0.5% $Cu:NaTaO_3$) (middle), and iii) High Cu loading (1 & 2.5% $Cu:NaTaO_3$) (bottom).

It should be noted at this point that the three systems formed in *Figure 3.12* in terms of Cu loading must also agree and be confirmed by Electron Paramagnetic Spectroscopy (EPR) spectra.

Color-wise, the flame-made nanoparticles are crispy white powders. The 1% & 2.5% Cu:$NaTaO_3$ powders have grey color (*Figure 3.1*). Upon increased Cu loading, copper particles are formed and thus, the color change intensifies. The band gap energy of the produced semiconductors was determined from the UV−Vis Diffuse Reflectance Spectroscopy (DRS) spectra, via the Tauc plot, using the Kubelka−Munk method [196] described in *Eq. 2.6*. It is known from the literature [197] that $NaTaO_3$ has direct and allowed transitions between the valance and conduction band of the n-type semiconductor and thus, the electronic transition-dependent exponent n equals with 1/2.

The UV-Vis Diffuse Reflectance Spectroscopy (DRS) spectra of the Cu:$NaTaO_3$ were obtained after converting the reflection coefficient R, to by Kubelka-Munk function as shown in *Figure 3.13*. Generally optical gap or band gap energy (E_g) values are derived from optical absorption spectra and diffuse reflectance spectra.

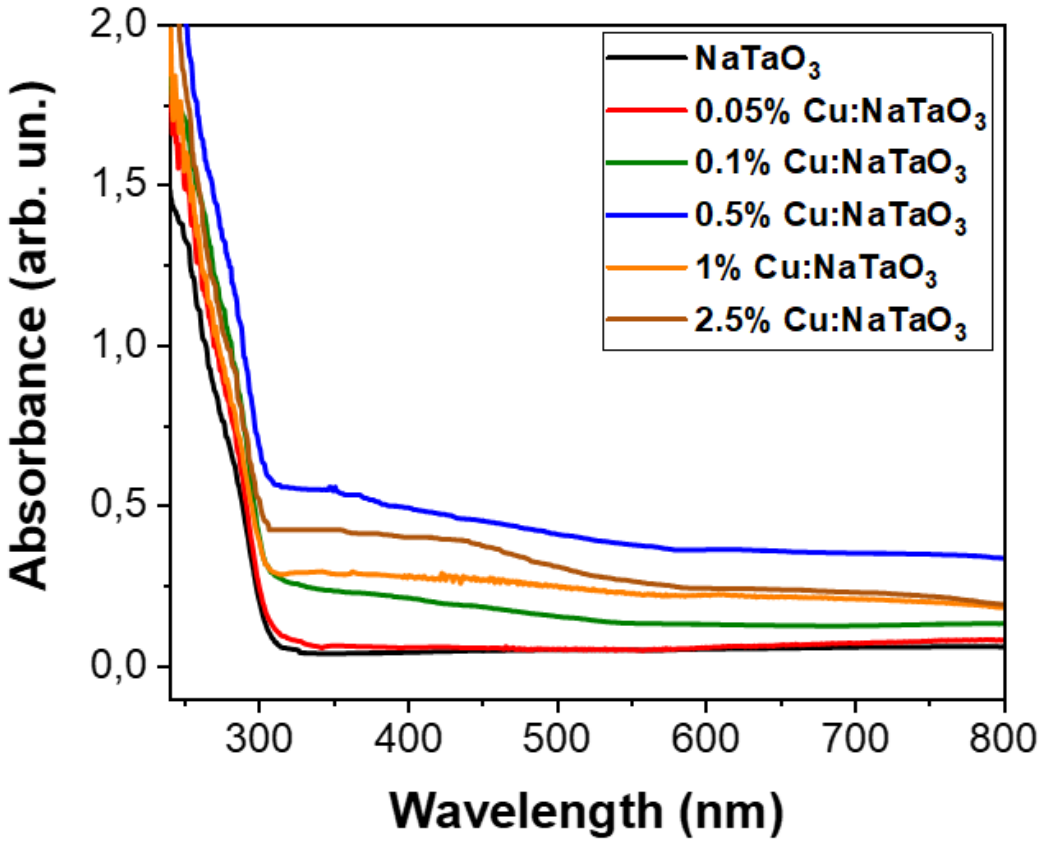

Figure 3.13: UV-Vis DRS spectra of the flame-made nanoparticles. The pristine $NaTaO_3$ spectrum corresponds to the black line and the 0.05%, 0.1%, 0.5%, 1% and 2.5% Cu:$NaTaO_3$ correspond to red, olive, blue, orange, and burgundy line, respectively.

Barium sulfate, $BaSO_4$, is used due to its high absolute reflectance ranging from 0.973 to 0.988. After the measurement of the standard reference sample in order to perform autozero, all background contributions are corrected. *Figure 3.13* shows the gradual rise of the background contribution as the concentration of copper increases. This observation accounts for the change in powder color as the structures absorb more radiation. It is also observed that in all cases the point of the crossing point of the tangents of the curves is approximately 320 nm. Therefore, it is predicted that the band gap energy values will have been in close proximity to each other.

The Tauc plot shown in *Figure 3.14* provides a quantitative calculation of bandgap energies. The crossing point between fit and abscissa will determine the bandgap energy. For precise calculation of the bandgap energy, the fitted line must always pass through the middle of the experimental line. Misuse of the Tauc Plot to determine the bandgap energy of the semiconductors may lead to erroneous estimates, especially in the case of modified semiconductors.

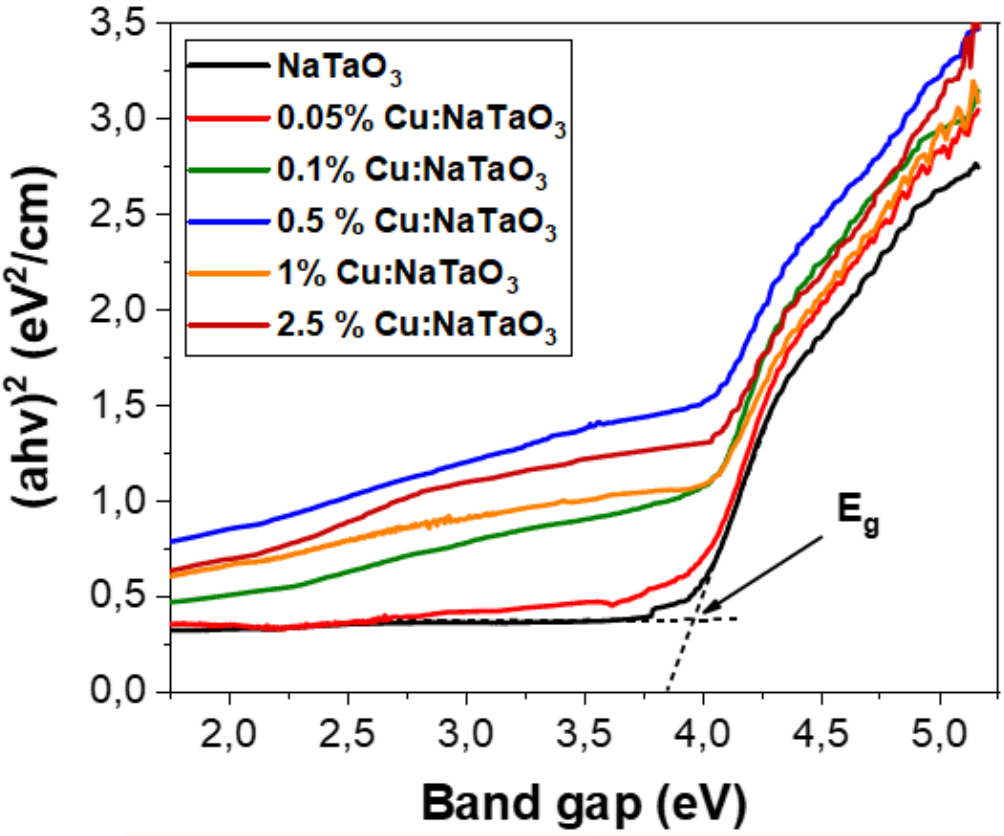

Figure 3.14: Tauc plots derived from UV−Vis DRS spectra in order to evaluate the band gap energy values of the semiconductors under study.

Makula addressed the aforementioned issue and proposed the correct way to determine the bandgap energy. An additional linear fit used as an abscissa must be applied for the slope below the fundamental absorption. The point where the two lines cross is the bandgap energy of the semiconductor. The evaluation of the band gap energy values in the current thesis was performed using Makula's method.

The crossing point between fit and abscissa will determine the bandgap energy. *Figure 3.14* shows that the crossing point in all cases is between 3.95 – 4.08 eV, as expected from the literature. The band gap energy values of the nanostructures are presented in *Table 3.4*. In the case of the highest concentration of copper (2.5% Cu:$NaTaO_3$, burgundy line) a change in the slope of the curve is observed at approximately 2.6 eV. According to the results of XRD, XPS, and Raman spectroscopy, copper atoms are deposited only on the perovskite surface and aren't embedded in the lattice. Thus, unexpected electronic states are localized on the surface of the nanomaterial. Surface states are defined as those located at the Fermi energy (or on the Fermi sphere) and are not necessarily geometrically surface. According to the Density of States (D.O.S) theory, the surface states are those of the Fermi band, and that mid-gap (forbidden) states can't be described by the model of the (almost) free electron and Tight Binding model. They don't predict D.O.S (normal modes of oscillation) in the Fermi band because the electron will escape to the conduction band. The *two-band model* is capable of describing the occurrence of states within the energy gap where the Fermi energy lies. The localized nature of the states can be described through this model by extending the bulk band structure to include imaginary wave vectors.

Table 3.4: Band gap energy evaluation of the semiconductors under study.

Sample	Band Gap (eV)
$NaTaO_3$	3.96 ± 0.02
0.05% Cu:$NaTaO_3$	3.96 ± 0.02
0.1% Cu:$NaTaO_3$	4.05 ± 0.02
0.5% Cu:$NaTaO_3$	4.08 ± 0.02
1% Cu:$NaTaO_3$	4.05 ± 0.02
2.5% Cu:$NaTaO_3$	4.05 ± 0.02

3.3 Electron Paramagnetic Resonance (EPR) analysis

EPR spectroscopy has been proven a valuable tool for the study of the coordination environment of Cu^{2+} at oxides or oxide–solution interface. EPR can also provide detailed information on the Cu^{2+} surface coordination, i.e., distances between neighboring Cu sites [198,199] in cases when weak Cu–Cu couplings do not result in signal alterations or loss. Thus, EPR can provide quantitative as well as coordination information on the Cu^{2+} interaction with surfaces. *Figure 3.15* shows the X-band EPR spectra for the allowed $\Delta m_s = 1$ transitions of the materials under study.

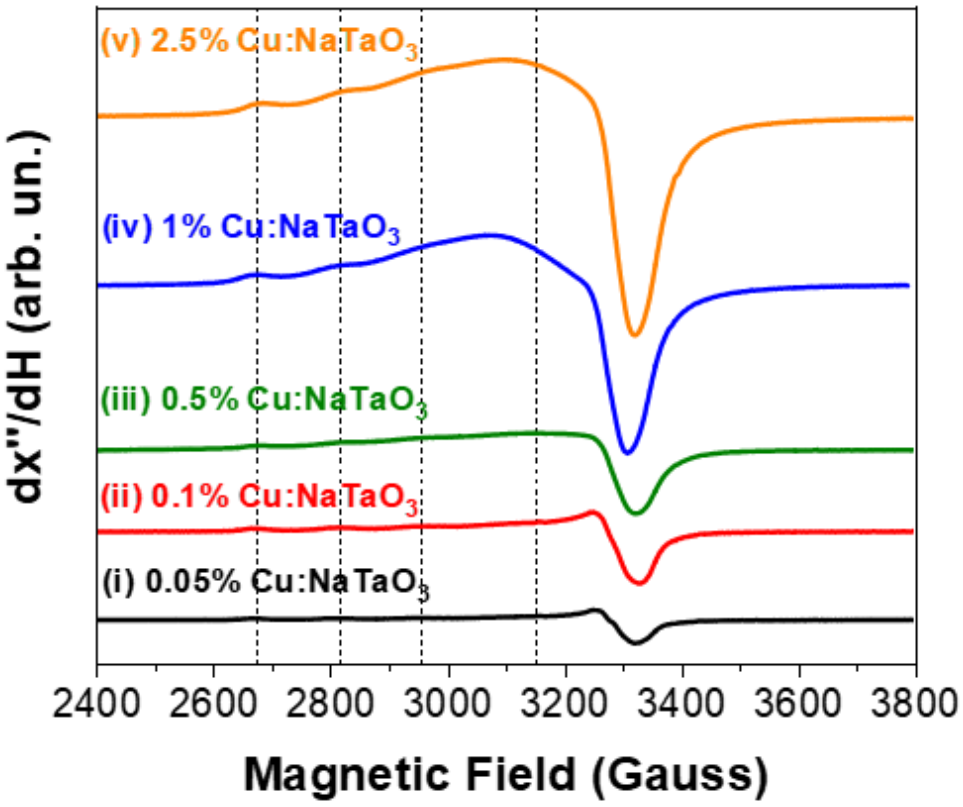

Figure 3.15: X-band EPR spectra of the materials under study. The black, red, olive, blue, and orange line correspond to 0.05%, 0.1%, 0.5%, 1%, and 2.5% Cu:$NaTaO_3$, respectively.

All spectra displayed in *Figure 3.15* have been plotted without any signal intensity correction. As discussed in the Raman analysis section, the samples can be divided into three categories based on the concentration of copper deposited on the perovskite surface. Small spectral changes are observed from the low to intermediate Cu loading.

The EPR of the low Cu concentration ((i) 0.05% & (ii) 0.1% Cu:$NaTaO_3$) are typical for mononuclear Cu^{2+} (electron spin $S = 1/2$, nuclear spin $I = 3/2$). From the first two spectra, the percentage of nanoclusters copper is much inferior to that of the mononuclear contribution. The third EPR spectrum ((iii) 0.5% Cu:$NaTaO_3$) corresponds to a transitional case where there is a significant part of mononuclear Cu^{2+} atoms as well as copper nanoclusters. The existence of the nanoclusters is indicated by the broadening (Lorentzian to Gaussian line shape) of the third (2950 Gauss) and fourth (3150 Gauss) hyperfine interactions to the extent that they overlap and increase in signal intensity. The last two spectra ((iv) 1% & (v) 2.5% Cu:$NaTaO_3$) correspond to the high Cu loading category, where the enhancement of the intensity of the nanoclusters is very substantial, affecting the behavior of the mononuclear copper atoms.

The EPR spectra for all materials studied here show weak EPR signals in the $g \sim 4$ region. In interacting Cu^{2+} spin pairs, the EPR spectral features depend on the spin-spin interaction [200]. Dipolar interactions result in 'semi-forbidden' $\Delta m_s = 2$ transitions which in X-band EPR spectra are detected at 'half-field' in the region 1500-1700 Gauss. In broad scan measurements, the contribution of these transitions is marginally distinguishable from the noise even in the case where the microwave power is amplified. In the case of the low Cu loading, no signals $g \sim 4$ were detected (data not shown). Therefore, one concludes that by increasing the concentration of copper, the dinuclear configuration of Cu atoms is not preferable and they will either be mononuclear on the perovskite surface or form nanoclusters with $n > 2$.

More generally, the nonzero intensity of the $\Delta m_s = 2$ signals indicate magnetic interaction, dipolar and exchange, between proximal Cu centers. A purely dipolar interaction is a through-space interaction that depends only on the Cu-Cu spin-spin distance. On the other hand, exchange interaction requires an orbital pathway connecting the two Cu atoms. Before any attempt for further interpretation of these signals, one has to have an estimate of the contribution of the exchange interaction vs the dipolar term. Typically, in non-crystalline Cu complexes, the exchange interaction occurs in cases of appropriate bridging molecules connecting two Cu atoms, which are usually located at a certain geometric proximity.

In the case of Cu complexes, literature data [201] show that considerable exchange interaction is usually operating at dinuclear Cu-Cu complexes with a Cu-Cu distance of ~ 3 Å or less, connected with appropriate bridging molecules. In such cases, the strong exchange and dipolar couplings lead to $S = 1$ effective spin states, characteristic of the dinuclear Cu complexes, which are not present in any of the spectra of the materials under investigation.

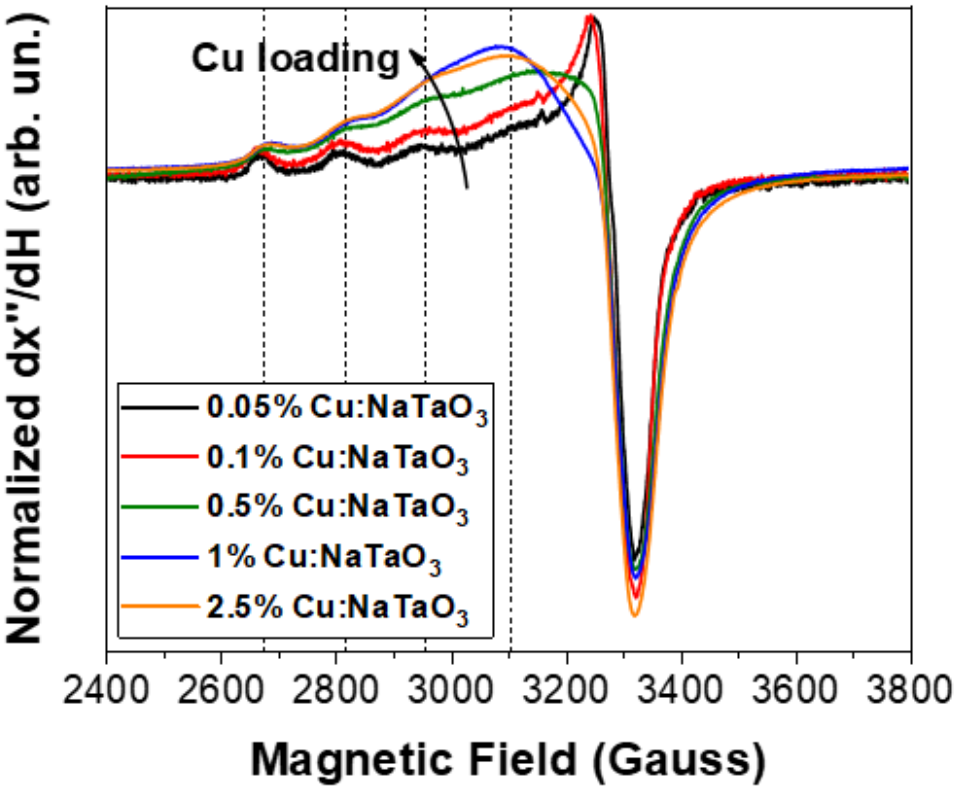

Figure 3.16: Normalized EPR spectra in terms of the signal intensity in order be directly comparable to each other.

Figure 3.16 has been normalized in terms of the signal intensity for the study of the spin-Hamiltonian parameters. As the copper concentration increases, the positions of the hyperfine interactions (g-values) do not drastically change. It is evident, as discussed above, that the nanocluster contribution is expressed as a broadening of the hyperfine interactions.

All EPR spectra can be simulated assuming a spin system with $S = 1/2, I = 3/2$, i.e., for Cu^{2+}. To facilitate the discussion, herein the spin-Hamiltonian parameters will be discussed in parallel with the number of tensors needed so as to achieve the simulation of the experimental spectra. The low Cu loading samples (0.05% & 0.1% Cu:$NaTaO_3$) can be simulated by assuming only one type of Cu^{2+} **g** and **A** tensor, herein called *tensor A*. Indicative for the 0.1% Cu:$NaTaO_3$ sample it appears that $(g_x, g_y, g_z) = (2.072, 2.062, 2.355)$ and $(A_x, A_y, A_z) = (13, 13, 166\ G)$. All values of **g** and **A** tensors are presented cumulatively in *Table 3.5*.

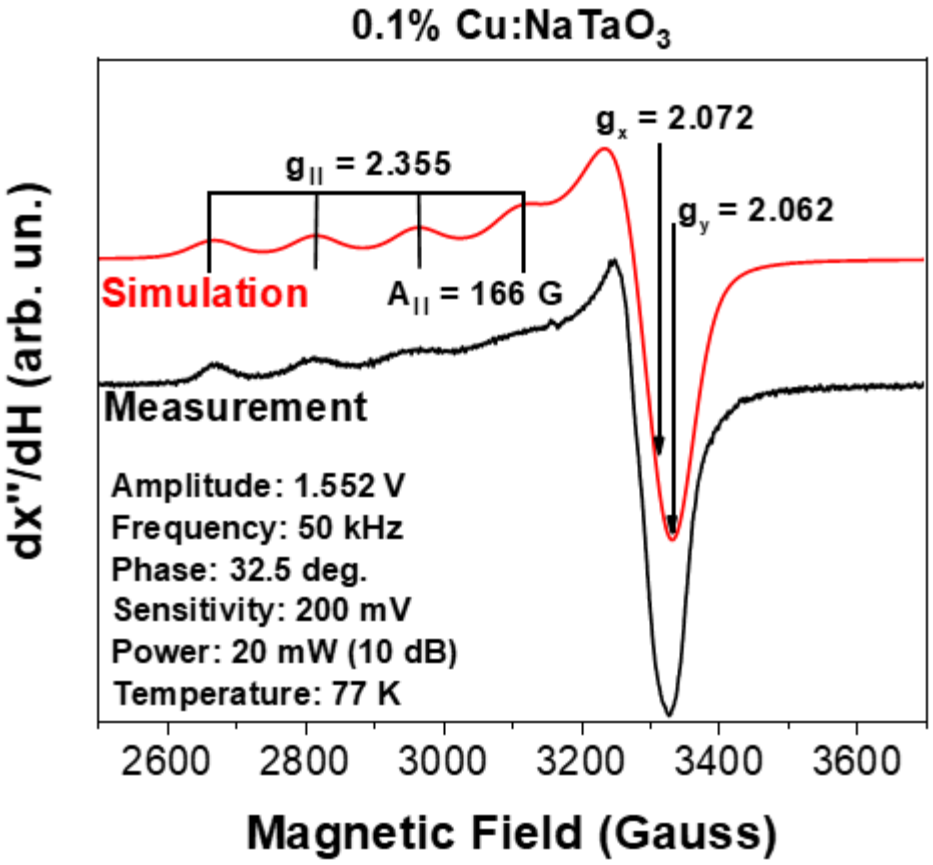

Figure 3.17: EPR spectrum of the measurement (black line) and the corresponding simulation spectrum (red line) indicative for the 0.1% Cu:$NaTaO_3$ sample.

In contrast, the EPR spectrum for the intermediate (0.5% Cu:$NaTaO_3$) and high Cu loading (1% & 2.5% Cu:$NaTaO_3$) can only be simulated using two Cu^{2+} tensors. One is tensor A, and the second one, herein termed *tensor B*, has the same **g** and **A** values with its corresponding tensor A, but the strain contribution has been added to the values of the hyperfine interactions, A, to simulate the contribution of the clusters as a background.

The increase in strain values broadens the linewidth of hyperfine interactions, transforming them from Lorentzian to Gaussian. It should be emphasized that the importance of the B tensor lies in the existence of clearly two different origins of the coppers (mononuclear and nanoclusters).

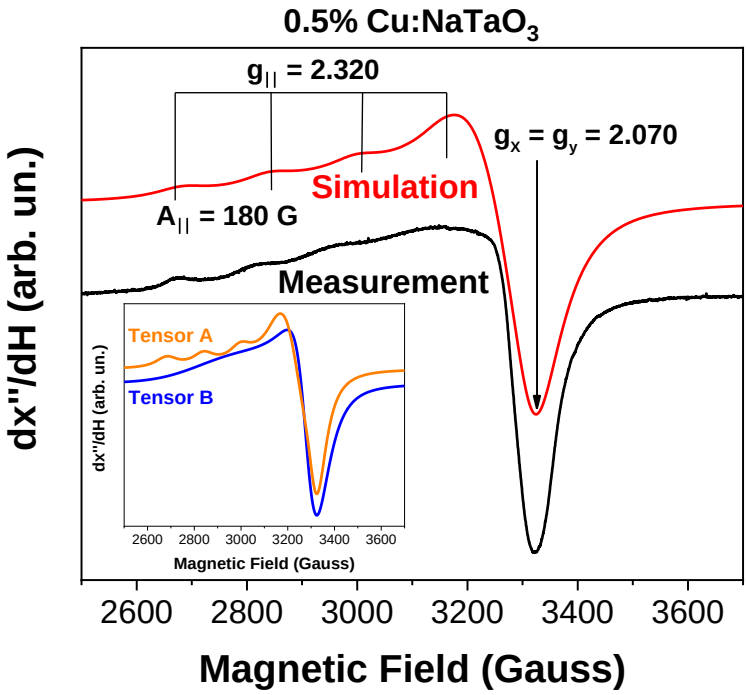

Figure 3.18: EPR spectrum of the measurement (black line) and the corresponding simulation spectrum (red line) indicative for the 0.5% Cu:$NaTaO_3$ sample. The inset shows the shape of the simulated curve for tensor A (orange line) and tensor B (blue line).

The values of the g and A tensors from the simulation spectrum for all samples are gathered in *Table 3.5*. It is observed that as the Cu loading increases, the values of the **g** tensor increase slightly, i.e., the spectra are shifted towards smaller magnetic field values. Moreover, the existence and amplification of the contribution of the nanoclusters are expressed as an increase in the values of the **A** tensor. Thus, the distance (in Gauss) of the hyperfine interactions increases resulting in the broadening of the linewidth. This observation will be very useful below, where the distance between Cu-Cu will be estimated.

Table 3.5: The g and A values from simulated spectra of the samples under study.

Sample ID	0.05% Cu	0.1% Cu	0.5% Cu	1% Cu	2.5% Cu
$g_x\ (\pm 0.002)$	2.070	2.072	2.085	2.083	2.080
$g_y(\pm 0.002)$	2.060	2.062	2.085	2.083	2.08
$g_z(\pm 0.002)$	2.365	2.355	2.380	2.395	2.388
$A_x(\pm 0.5)$	10	13	15	15	15
$A_y(\pm 0.5)$	10	13	15	15	15
$A_z(\pm 0.5)$	160	166	170	173	175

Quantitative EPR measurements using copper nitrate $(Cu(NO_3)_2)$ in ethanol, as spin standard, with the addition of 20% v/v glycerol, shown in *Figure 3.19*, were made in order to correlate the nominal concentration interfaced on the perovskite surface and the actual concentration detected by EPR spectroscopy. Small concentrations (500 to 50 μM) up to approximately the detection limit of the technique have been selected.

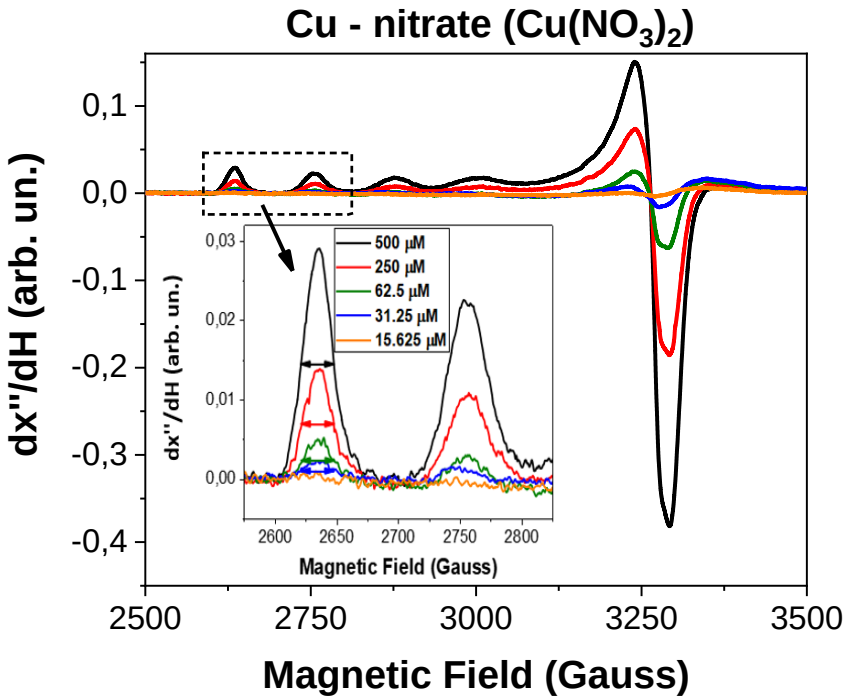

Figure 3.19: EPR spectra of Cu-nitrate in ethanol/glycerol solution as a function of the concentration. The inset shows the linewidth of the first two hyperfine interactions and the horizontal arrows correspond to the FWHM of each curve.

Due to the good dispersion of copper in ethanol, the hyperfine interactions of the recorded spectra are more resolved concerning the powder measurements above. The g and A values do not change at all with increasing concentration. A very important quantity is also the Full Width at Half Maximum (FWHM) of the linewidth. In this particular system, this value does not change and is constant and independent of the concentration at $\Delta H_{intr} = 27\ Gauss$. This constant value is an intrinsic property of the system as it relates to the Cu-Cu distance. Therefore, the minimum linewidth of 27 Gauss acts as a diagnostic tool for the identification of a completely weakly coordinated environment of Cu atoms and thus, the detection of purely mononuclear atoms.

Through double integration, one can calculate the area under the curve which is a quantity related to the concentration of copper detected. The area by double integration is calculated for both the spin standard system and the Cu:$NaTaO_3$ materials. Because the experimental measurement process of the spin standard system was done in solution (120 μl total volume), while the materials under study were measured in powder form (usage of the S.S.A, *Table 3.3*), the correlation of the results must be done by comparing the areas to moles and then converting to concentrations.

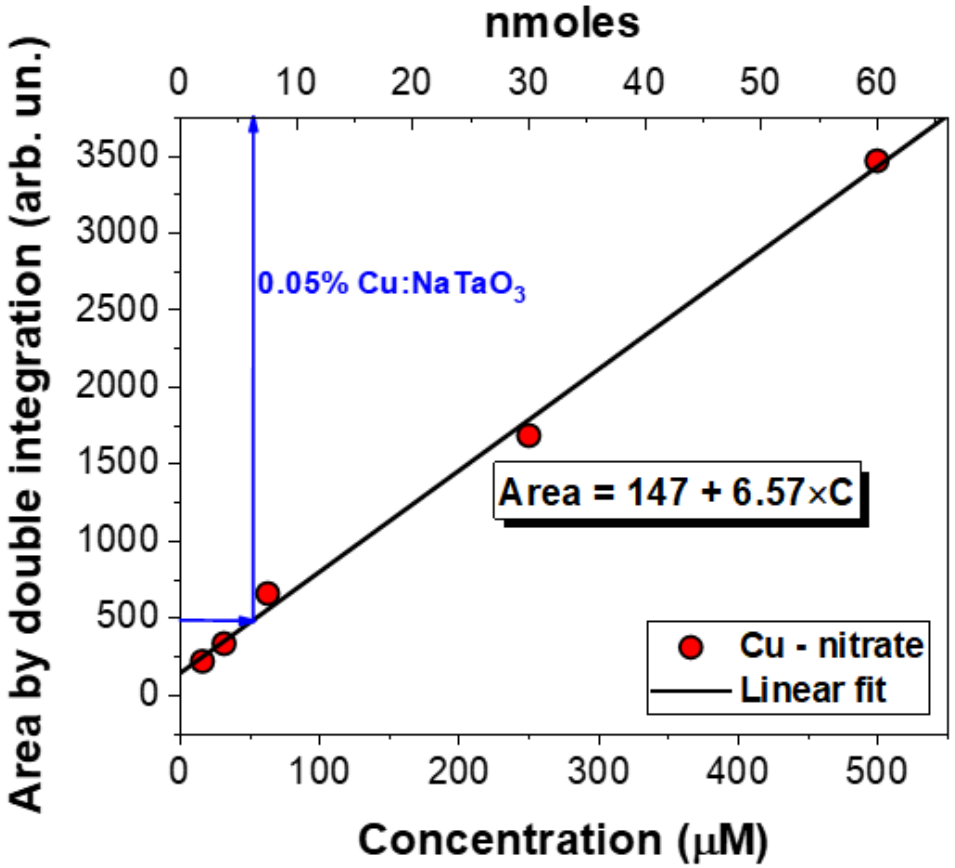

Figure 3.19: The protocol used in order to correlate the nominal Cu concentration interfaced on the nanoparticles surface to its actual detected by EPR value via the area by double integration.

The above procedure is as follows. First, the area for each of the nanoparticles is calculated. Then through the linear relationship obtained from the measurements of the spin standard system, the above calculates areas corresponding to the horizontal scale of nmoles. Then using the Specific Surface Area (S.S.A) values calculated through the B.E.T analysis, moles are converted to concentration once again. Finally, the concentration is compared to the initial concentration of the perovskite (0.6 M) so as to find the actual value of the percentage of copper that has been deposited on its surface. The results of the nominal value relative to the actual value detected through EPR spectroscopy are presented in column form in *Figure 3.20*.

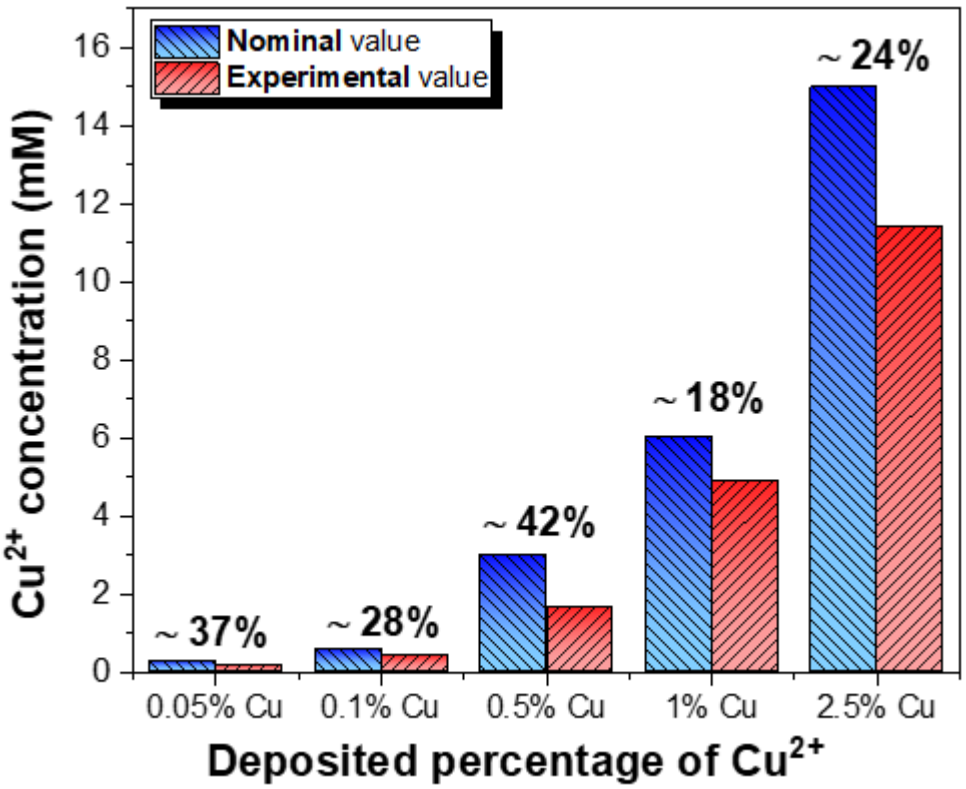

Figure 3.20: Correlation diagram between the nominal value of the deposited percentage of Cu^{2+} and the experimental value, derived from EPR spectroscopy. The percentage over the columns is the deviation in each case of the two values.

The deviations of the compared values are of the order of approximately $20 - 40\%$. The deviation is mainly due to the way the Cu^{2+} was atomically dispersed on the perovskite matrix. The possibility of inadequate signal detection is negligible, as the technique is due to *resonance* with enormous resolution (10^{-9} spins or nmoles). It is, also, observed that the deviation decreases as the Cu loading increases. Therefore, spectra that include nanocluster contribution are better detected.

Linewidth broadening

As explained above, in the spin standard system the linewidth is constant at $\Delta H_{intr} = 27\ Gauss$ regardless of concentration. This value is representative of loosely bounded Cu atoms on $NaTaO_3$ surface due to the FSP method used. In *Figure 3.21*, the broadening of the linewidth of the $Cu:NaTaO_3$ samples are presented. For the correct interpretation of the data, a baseline correction has been made without any changes in signal intensity.

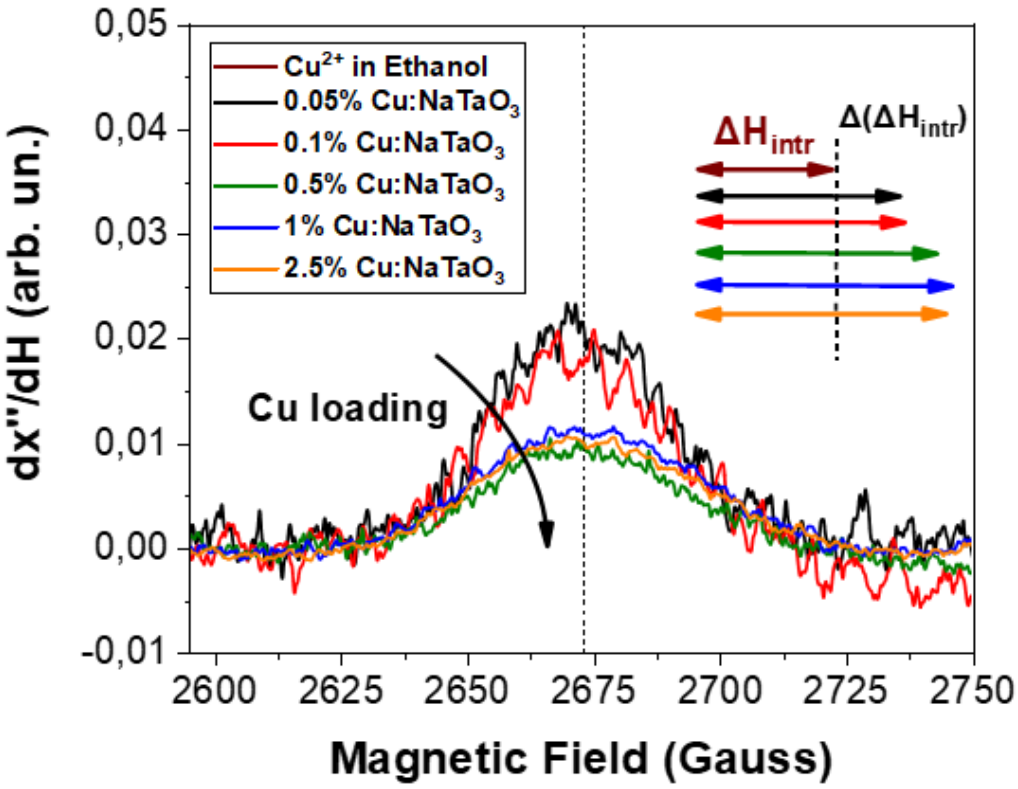

Figure 3.131: The first hyperfine interaction of all samples under investigation in order to study the broadening of the linewidth. The spin standard system (Cu2+ in ethanol/glycerol solution corresponds to burgundy line. The 0.05%, 0.1%, 0.5%, 1%, and 2.5% $Cu:NaTaO_3$ samples correspond to black, red, olive, blue, and orange line, respectively.

One immediately notices that as the Cu loading increases, the broadening becomes greater. In the first two spectra (0.05% & 0.1% $Cu:NaTaO_3$) in the case of low Cu loading the broadening is slightly larger than that of the spin standard system. Therefore, broadening occurs due to the change in the coordination environment of the Cu^{2+} atoms caused by interactions or *heterogeneities on the perovskite surface*.

In the cases of intermediate (0.5% Cu:$NaTaO_3$) and high Cu loading (1% & 2.5% Cu:$NaTaO_3$) the broadening of the linewidth becomes even greater. This result is due to two reasons. Firstly, due to the existence of surface heterogeneities and due to the broadening of the **A** tensor, as discussed above, through the contribution of the nanoclusters.

The intrinsic broadening (in Gauss) of the spin standard system has been assigned to the *Figure 3.21* inset with a burgundy arrow. There is direct color matching between the curve of the spectra and the arrow corresponding to the broadening of the linewidth. The difference concerning this value corresponding to the nanoparticle's spectra has been determined as $\Delta(\Delta H_{intr})$ and it follows the relationship:

$$\Delta(\Delta H_{intr}) = \Delta H - 27\ Gauss, \qquad (Eq.\ 3.1)$$

where ΔH is the measured linewidth broadening. The $\Delta(\Delta H_{intr})$ values for each sample are recorded in the *Table 3.6*.

Table 3.6: The difference in relation to the intrinsic linewidth broadening corresponding to the spin standard system.

Sample ID	$\Delta(\Delta H_{intr})$
0.05% Cu:$NaTaO_3$	13.5 Gauss
0.1% Cu:$NaTaO_3$	14 Gauss
0.5% Cu:$NaTaO_3$	24 Gauss
1% Cu:$NaTaO_3$	27 Gauss
2.5% Cu:$NaTaO_3$	26 Gauss

As explained above, there is a broadening of about 14 Gauss in the case of atomically dispersed Cu^{2+} atoms and about 25 Gauss due to the formation of Cu nanoclusters.

The coordination environment of Cu^{2+} atoms

Structural information can be obtained by spectroscopic methods. As explained in Chapter 2, Electron Paramagnetic Resonance (EPR) can be a valuable tool, providing information on the Cu coordination as well as on the Cu-Cu distance.

Peisach and Blumberg have developed a method that correlates spin-Hamiltonian parameters $g_{\parallel}$ and $A_{\parallel}$ with the number and type of coordinated atoms in Cu^{2+} complexes. In many cases, this method may be used to assign structural elements of the coordinating environments and the way Cu^{2+} atoms interact with other neighbors. In this particular case, one can find the way the atoms bind with the perovskite matrix (e.g., loose binding or strong binding). As a point of reference, the spin standard system (copper nitrate in ethanol/glycerol solution) has been taken into account, where there is only mononuclear distribution of Cu atoms and no clusters have been formed so as to shift the **g** and **A** tensors. *Table 3.7* lists the values of these tensors resulting from the simulation of the spectra.

Table 3.7: The g and A values for the spin standard system, resulting from the simulation of their spectra.

$Cu(NO_3)_2$	500 μM	250 μM	62.5 μM	31.25 μM
$g_x\ (\pm 0.002)$	2.082	2.082	2.082	2.082
$g_y(\pm 0.002)$	2.080	2.080	2.080	2.082
$g_z(\pm 0.002)$	2.415	2.415	2.415	2.417
$A_x(\pm 0.5)$	10	10	10	10
$A_y(\pm 0.5)$	10	10	10	10
$A_z(\pm 0.5)$	145	145	145	143

The tensor values do not change as the $Cu(NO_3)_2$ concentration decreases in the first three cases (500, 250, and 62.5 μM). Only in the latter (31.25 μM), where it is at the detection limit, is a very small shift of the $g_{\parallel}$ tensor towards smaller values of magnetic fields seen in association with a minimal decrease in of the $A_{\parallel}$ value.

In *Figure 3.22*, the so-called Peisach–Blumberg plot is presented for the surface species types (Mononuclear Cu atoms, nanocluster), using the $g_{\parallel}$ and $A_{\parallel}$ from *Tables 3.5 and 3.7*.

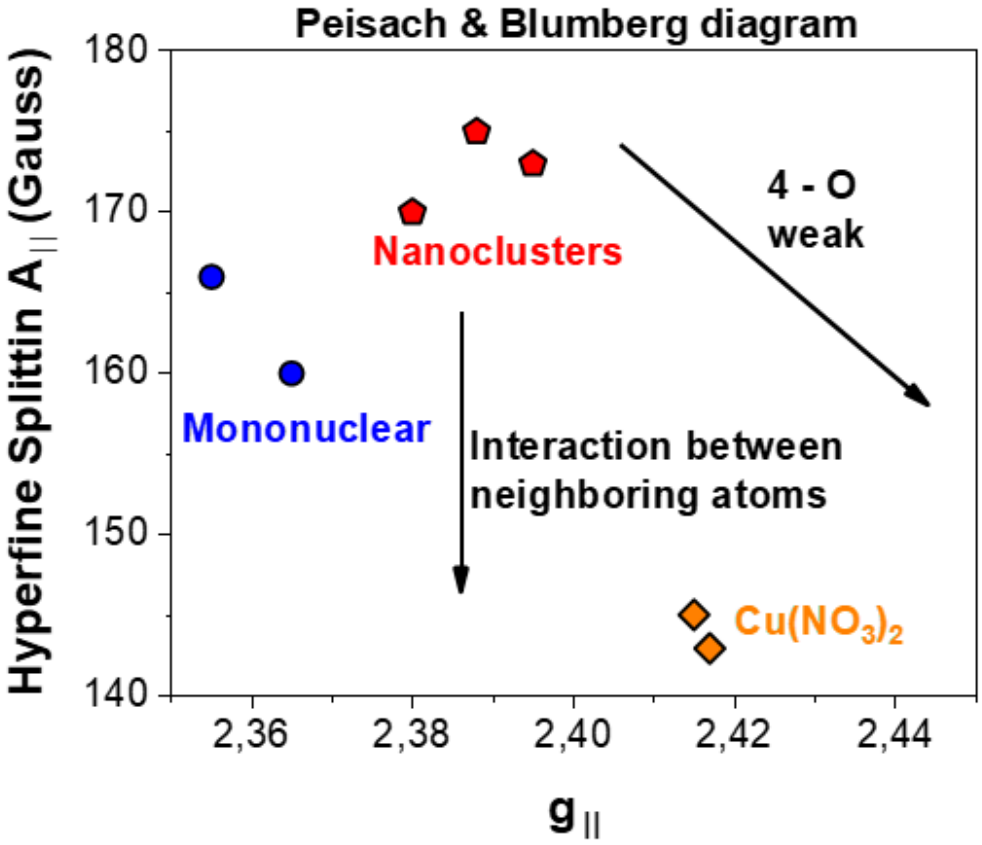

Figure 14.22: The relationship between $g_{\parallel}$ and $A_{\parallel}$ for the surface species of Cu^{2+} atoms.

The vertical downward shift observed on going from nanoclusters to mononuclear atoms indicates a progressive weakening of the neighboring interaction field around the Cu^{2+} atoms. Copper atoms in a cluster interact to a greater extent with neighboring atoms than in the case of single atoms. Therefore, the decrease in hyperfine splitting can be linked to the reduction of the interaction of neighboring copper atoms. Most importantly, the data in *Figure 3.22* for all species fall in the region where 4-oxygens are coordinating the Cu^{2+} cations. These oxygens may originate from the perovskite matrix ($NaTaO_3$). Thus, the EPR spectra provided detailed structural information.

Cu-Cu Distance Estimation

In interacting Cu^{2+} spin pairs, the EPR spectral features depend on the spin-spin interaction. Eaton et al [202] have demonstrated that in infinite diluted samples where intermolecular spin-spin interaction from neighboring complexes is negligible, the intensity of the half-field transition ($g \sim 4$) can be used for a relatively accurate estimate of the distance between the coupled spins:

$$R\,(\text{Å}) = \sqrt[6]{\frac{A}{I}\left(\frac{9.1}{v}\right)^2}, \qquad (Eq.\,3.2)$$

where

$$I = \frac{integrated\ intensity\ of\ the\ \Delta m_s = 2\ EPR\ signal}{integrated\ intensity\ of\ the\ \Delta m_s = 1\ EPR\ signal} \qquad (Eq.\,3.3)$$

Factor A is a fixed empirical constant [202], which has been shown to depend on the g-value anisotropy:

$$A = 19.5 + 10.9|g_{max} - g_{min}| \qquad (Eq.\,3.4)$$

For Cu^{2+} complexes $|g_{max} - g_{min}|$ is of the order of 0.2 or less. Therefore, factor A can be in the range of $20 - 21$. This method has proven to give accurate results in Cu-Cu complexes for distances in the range of approximately $4 - 6$ Å. The applicability of this method depends critically on the elimination of interferences from nonspecific spin-spin interactions from neighboring complexes. In this case, it cannot be used because the signal detection at the half-field region is negligible.

There is a more reliable distance estimation method but in order to be valid and respect the working geometrical scheme, extracted from Peisach and Blumberg correlation, several reasonable assumptions must be made.

First, the next neighbors are expected to contribute less to the dipole-dipole interaction than immediate neighbors. Each Cu-Cu interaction will have an effective geometrical radius R_{Cu} determined by its Van der Walls radius, i.e $R_{VDW} \approx 4$ Å for Cu atoms. Thus, in a limiting case of the closest packing scheme, the immediate neighboring Cu-Cu atoms will be at a distance R_{VDW} or greater, whereas the next neighbors will be located at least $2R_{VDW}$.

According to Eaton's formula (*Eq. 3.2*), due to the R^{-6} dependence of the $[\Delta m_s = 2]/[\Delta m_s = 1]$ intensity ratio, the contribution of the next neighbors to the intensity ratio will be scaled down by $1/2^6 = 1/128$ times relative to the immediate neighbors. Thus, only the immediate neighbors must be taken into account for every Cu-Cu interaction.

Second and most important, the spectra of pairs belong to the *weak exchange limit*, and more generally the isotropic and anisotropic interactions have comparable magnitude; the singlet and triplet states are no longer pure spin states. In the hypothesis that all the anisotropic interactions come from the dipolar interaction, the measured D_{AB} values can be used to estimate the distance between the spin centers, R_{AB}, using the relationship:

$$D_{AB}(cm^{-1}) = \frac{3g^2{}_{AB}\,\mu_B}{2R^3{}_{AB}} \overset{g\approx 2}{\Longrightarrow} D_{AB}(cm^{-1}) = \frac{1.732}{R^3{}_{AB}(\text{Å})}, \qquad (Eq.3.5)$$

where $R^3{}_{AB}(\text{Å})$ is the Cu-Cu distance and $D_{AB}(cm^{-1})$ is the dipolar tensor. In order to convert cm^{-1} to Gauss, the following relation is being used: $1\ cm^{-1} \approx 10.700\ Gauss$. As the isotropic and anisotropic interactions have comparable magnitude, the D_{AB} tensor can be expressed to a good approximation through the hyperfine **A** tensor to estimate the distance between the spin centers.

As discussed above, in the hypothesis of dipolar interaction the intensity of the $\Delta m_s = 2$ transitions depend on R^{-6}. The intensity of the signal in a polycrystalline sample or a frozen solution results from the spherical average of the single crystal intensities and it is therefore expected to depend also on R^{-6}. *Table 3.8* shows the values of $A_{\|}$ calculated above and the resulting distance between the spin centers.

Table 3.8: The Cu-Cu distance estimation based on the hyperfine splitting value.

Sample ID	$A_Z = A_{//}$ $(Gauss)$	Cu-Cu distance (Å)
Spin Standard	145	5.03 ± 0.03
0.05% Cu	160	4.87 ± 0.03
0.1% Cu	166	4.81 ± 0.03
0.5% Cu	170	4.78 ± 0.03
1% Cu	173	4.75 ± 0.03
2.5% Cu	175	4.73 ± 0.03

The Cu-Cu distance for the samples under study is between the values of $4.73 - 4.87$ Å. As the concentration of copper deposited on the perovskite surface increases, this distance decreases. Therefore, it correctly follows that in the case of the spin standard system, the spin centers should have a greater distance between them (5.03 Å).

These distances would be correct only for hypothetical homogeneous distributions of surface Cu atoms. However, the heterogeneity in distances and populations, as discussed above, introduces an error in this distance estimation. The error may be either an overestimate or an underestimate of the real distance, depending on the details of the distance and major population distribution. *Figure 2.33* shows the relationship between the hyperfine splitting as a function of the distance between the spin centers.

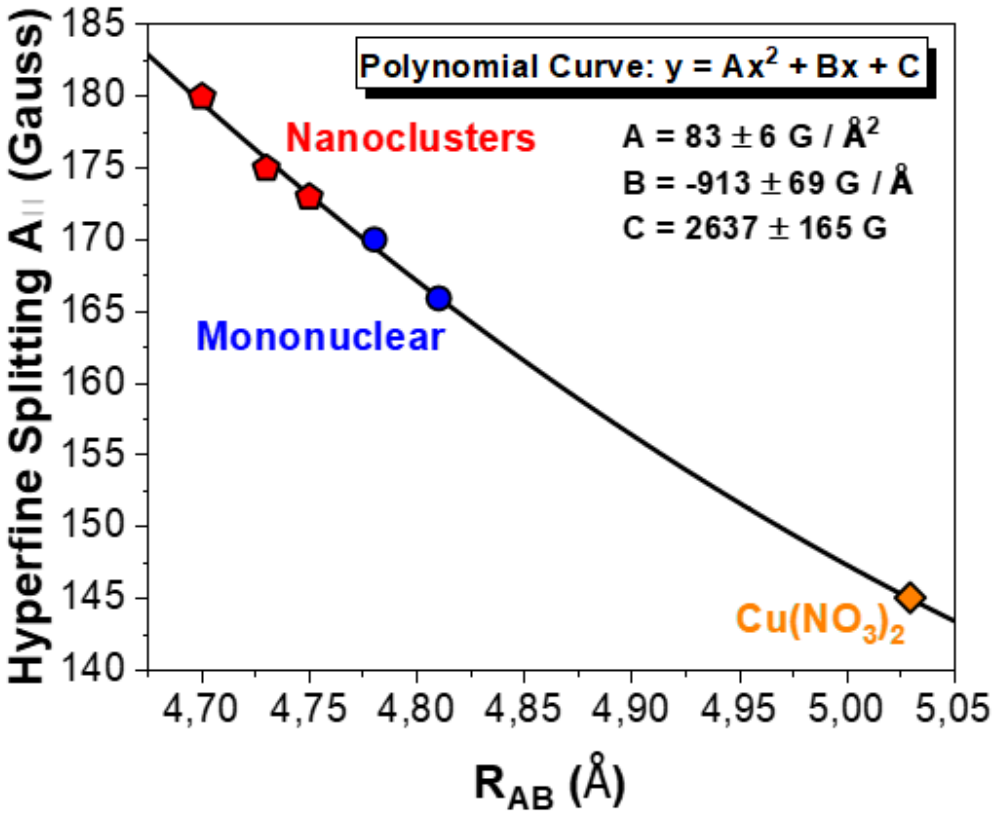

Figure 3.23: The relationship between Hyperfine splitting ($A_{\parallel}$) and distance of spin centers (R_{AB}).

The two quantities follow a polynomial relationship ($y = Ax^2 + Bx + C$). As the hyperfine interaction, i.e., the interaction between neighboring atoms, decreases, the distance between the spin centers increases. As a result, the large distance between the centers characterizes the mononuclear copper atoms.

3.4 Photocatalytic H_2 evolution from H_2O splitting

Experiments were performed in a double-walled photochemical reactor with a total reaction volume of 340 mL at room temperature (25 ℃), controlled by a circulation chiller cooling system. The light source was a 250 W Mercury lamp (UV irradiation) inserted at the geometrical center of the photoreactor inside the quartz immersion well. The irradiation power at an experimental mean distance of 3 cm was 0.34 W/cm^2, measured in situ with a power meter. In each experiment, 69 mg of the catalyst was suspended in 200 mL (or 220 mL) triple distilled H_2O and 50 mL (or 55 mL) methanol (20% v/v).

Figure 3.24 presents the photocatalytic H_2 production data from H_2O splitting for the pristine $NaTaO_3$ and the Cu:$NaTaO_3$ nanoparticles. It should be emphasized that in these experiments, there was *no inclusion of Pt* or other noble metals as cocatalysts.

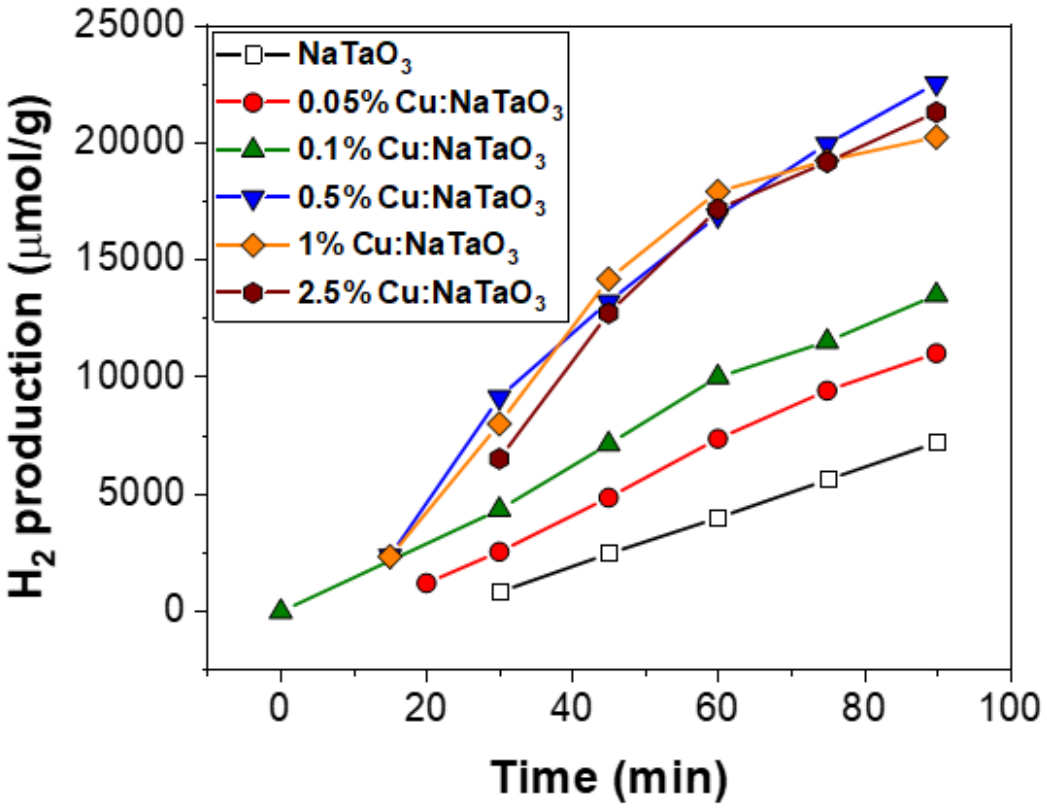

Figure 3.215: Kinetics of photocatalytic H_2 production under a Mercury lamp irradiation. The black line corresponds to $NaTaO_3$ nanoparticles. The red, olive, blue, orange, and burgundy lines correspond to 0.05%, 0.1%, 0.5%, 1% and 2.5% Cu:$NaTaO_3$, respectively.

The kinetics in *Figure 3.24* shows an initial delay of H_2 production in all materials, except 0.05% Cu:$NaTaO_3$. It seems that as the concentration of copper increases, which plays a co-catalyst role, the slope of the curves increases. Therefore, the rate of hydrogen production increases while increasing the cocatalyst. *Figure 3.25* presents the H_2 production yields for the photocatalysts.

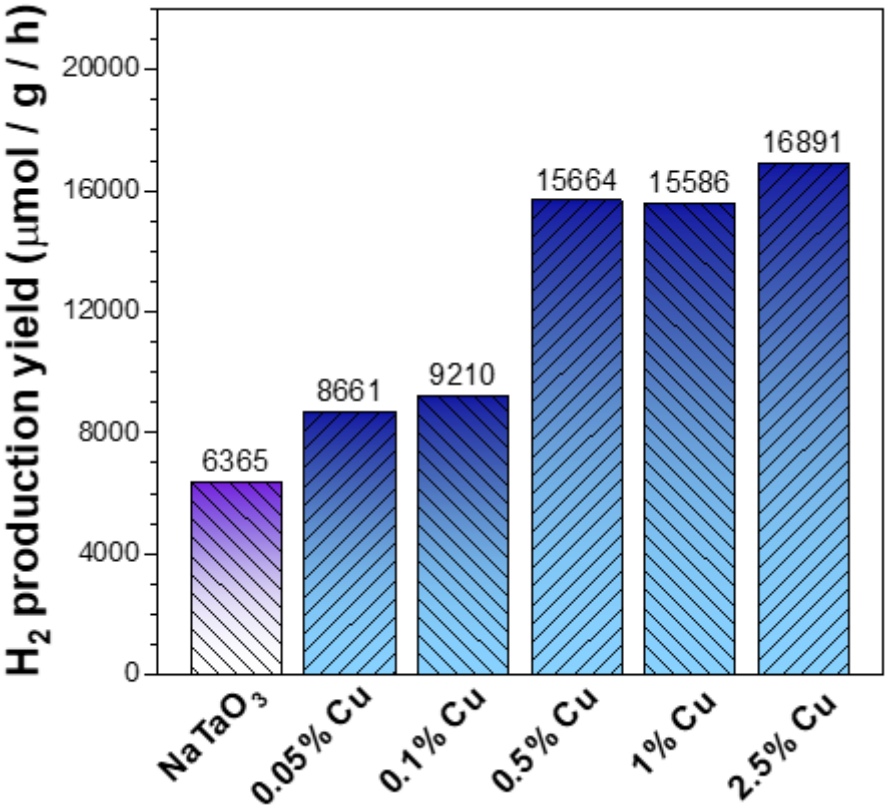

Figure 3.216: Comparison of the H_2 production yields for each sample.

The yield of pristine $NaTaO_3$ perovskite is about $6365\ \mu mol/g/h$. The samples with low Cu loading, 0.05%, and 0.1% Cu:$NaTaO_3$, increase the H_2 production yield by approximately 36% and 45%, respectively. The samples with intermediate, 0.5% Cu:$NaTaO_3$, and high Cu loading, 1%, and 2.5% Cu:$NaTaO_3$ further increase the production yield by 146%, 145%, and 165%, respectively. Overall the present data demonstrate that the enhancement of the catalytic activity, which is achieved by controlling the loading of the Cu^{2+} deposition, is not a simple subtractive effect. At higher loadings (2.5% Cu:$NaTaO_3$) a fundamentally beneficial mechanism takes place which increases the H_2 production yield.

Comparison with the Literature

Table 3.9 contains the literature summary of $NaTaO_3$ materials used as photocatalysts for H_2 production.

Table 3.9: Literature summary of $NaTaO_3$ photocatalysts.

Material ID	Composition	Preparation method	Surface Area (m^2/g)	H_2 production yield (μmol/g/h)	Ref.
$NaTaO_3$	Na/Ta (1/1)	Hydrothermal	7	2.800	81
$NaTaO_3$	Na/Ta (1/1)	Solid-state reactions	0.3	314	45
Cu/$NaTaO_3$	$NaTa_{0.92}Cu_{0.08}O_3$	Solid-state reactions	-	70	203
NiO/$NaTaO_3$	0.05 wt. % NiO	Solid-state reactions	1.6	3.340	74
NiO/$NaTaO_3$	0.05 wt. % NiO	Flame Spray Pyrolysis	37.3	390	83
La:$NaTaO_3$	2 mol%	Sol-gel process	4.54	2800	204
Mg:$NaTaO_3$	2 mol%	Solid-state reactions	0.5	242	205
Ca:$NaTaO_3$	2 mol%	Solid-state reactions	2.6	408	205
Sr:$NaTaO_3$	2 mol%	Solid-state reactions	3.4	1.060	205
Ba:$NaTaO_3$	2 mol%	Solid-state reactions	3.5	1.058	205

In principle, the crystallinity is an essential point for the efficiency of a photocatalyst, because it has been commonly accepted that the formation and separation of photoexcited electron–hole pairs benefit from high crystallinity. Therefore, the photocatalytic performance of amorphous materials mostly suffers from a relatively higher number of defects incorporated in the structure when compared with the crystalline counterparts. In addition to the crystallinity, heterojunctions resulting efficient charge carrier separation, thus boosting the photocatalytic activity of a material. Further, the activity of the photocatalyst is strongly affected by the size of the particles and thus correlates with the surface area and number of active sites on the surface.

The two directions (crystallinity and small particle size) are inherently difficult to combine with the conventional solid–state reactions since the procedures to obtain highly crystalline materials mostly involve high-temperature treatment leading to bulk materials with larger particle sizes. On the other hand, the synthetic approach via hydrothermal synthesis can be applied to produce nanosized crystalline materials with a high surface area at low temperatures. The only technique that achieves both factors and the synthesis of the materials is completed in one step process, having the advantage of industrial production is the *Flame Spray Pyrolysis*.

After the photocatalysis, the material was collected by centrifugation and, after careful drying, remeasured once more via Electron Paramagnetic Resonance. *Figure 3.26* shows the 1% Cu:$NaTaO_3$ sample as an example. It is noted that all samples had the same result.

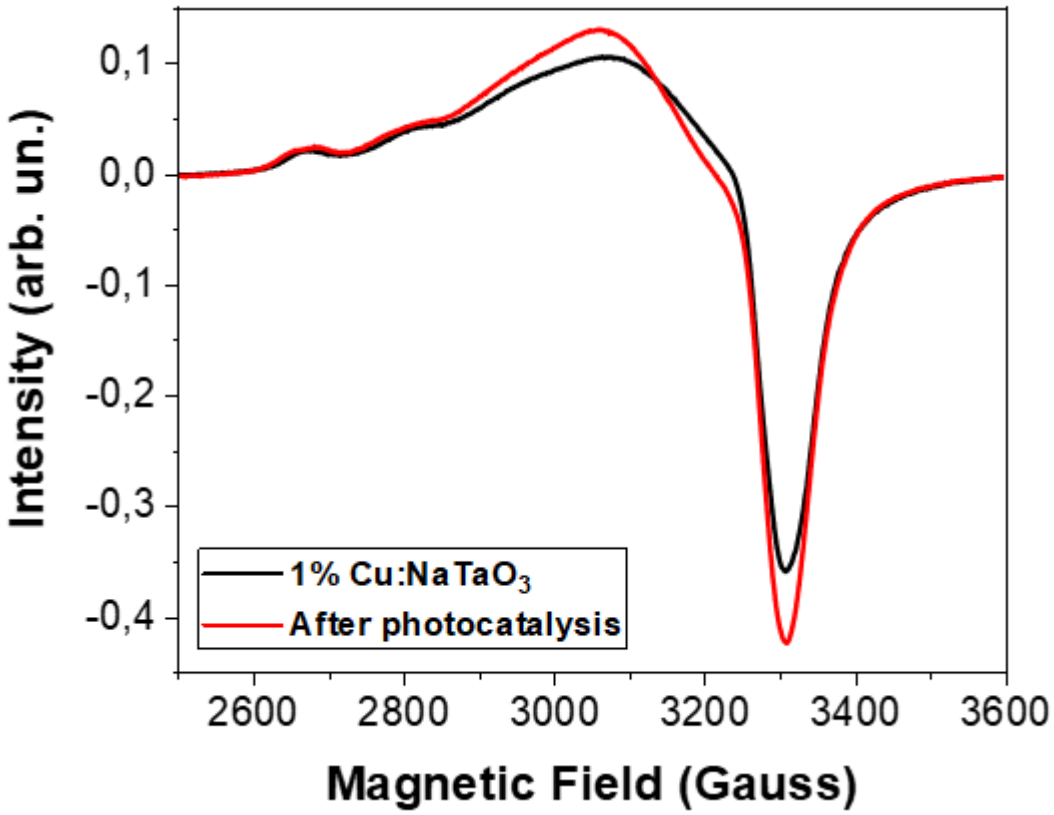

Figure 3.26: EPR spectra of 1% Cu:$NaTaO_3$ before photocatalysis (black line) and after photocatalysis (red line).

The intensity of the EPR signal from Cu^{2+} may be regarded as a measure of the oxidation degree. When a progressive reduction of Cu^{2+} to Cu $^{1+}$ or Cu^0 occurs, the intensity of the EPR signal must decrease to zero.

After approximately 2 hours of photocatalytic use, the Cu atoms on the $NaTaO_3$ surface remain almost intact, having a minimal percentage of Cu leaching. This shows that the Flame Spray Pyrolysis deposition method creates a *stable anchoring of Cu atoms on the $NaTaO_3$ particles*.

3.5 Electrochemical activity

The electrochemical activities of flame-made nanoparticles were analyzed using Linear Sweep Voltammetry (LSV), Cyclic Voltammetry (CV), and Electrochemical Impedance Spectroscopy (EIS). A potentiostat with a three-electrode electrochemical cell was used for the electrochemical analysis in 0.1 M NaOH solution as an electrolyte. Before each measurement, the electrolyte has been saturated with argon (Ar) gas for 20 min, to reduce the oxygen concentration (8 ppm) so that they do not contribute to the redox reactions.

A three-electrode cell consisting of a Pt-wire counter electrode, an Ag/AgCl (3 M saturated KCl) reference electrode, and a particle-coated FTO working electrode (25 cm^2) was used to carry out all electrochemical measurements. The conversion of the Ag/AgCl electrode to the Reversible Hydrogen Electrode (RHE) scale is done using the Nernst equation:

$$E_{RHE} = E_{Ag/AgCl} + 0.187 + 0.059 \cdot pH \qquad (Eq.3.6)$$

The electrical polarization curves of the current density against potential were measured for all samples to evaluate their electrocatalytic activity. LSV data, shown in *Figure 3.27* were obtained at the applied potential range $+0.2$ V to -0.8 V vs Ag/AgCl with a scan rate of $20\ mV/s$.

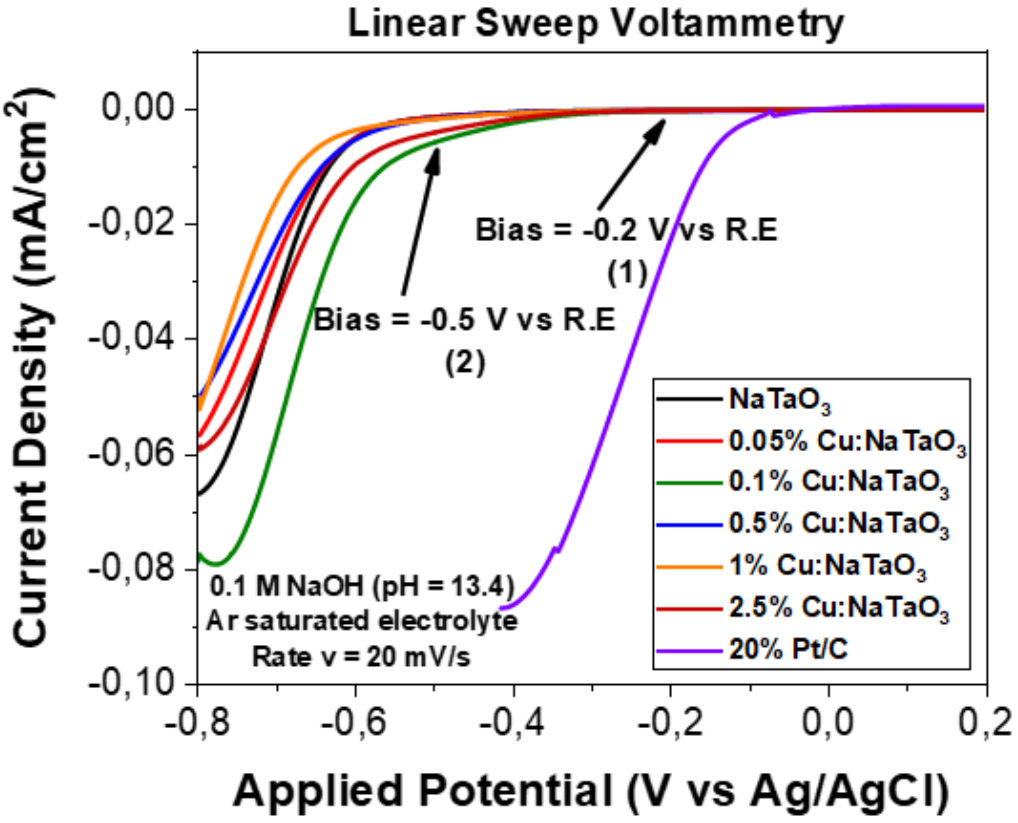

Figure 3.27: Linear Sweep Voltammetry curve of the flame-made materials in comparison with the 20% Pt/C reference sample. The black and violet lines correspond to $NaTaO_3$ and 20% Pt/C, respectively. The red, olive, blue, orange, and burgundy lines corresponds to 0.05%, 0.1%, 0.5%, 1%, and 2.5% Cu:$NaTaO_3$, respectively.

In the negative potential range, the reductive part of the reaction is seen. Up to about -0.3 V vs Ag/AgCl in all samples, the system is in equilibrium, without any current (or current density) being recorded. At potentials greater than this value, a negative current density is recorded, thus indicating the existence of a reduction reaction. At the limit of the measurement (-0.8 V vs Ag/AgCl), all samples have almost the same current density value, except for the 0.1% Cu:$NaTaO_3$ which has a higher one. The higher current density value always combined with the lower onset potential promotes the electrocatalytic activity of the sample under investigation. As a reference sample, with the best activity till now, 20% Pt/C has been chosen. *Table 3.10* lists the onset potential, the lowest potential value at which a reaction takes place, of all measured materials.

Table 3.10: Onset potential of the nanoparticles through LSV measurements.

Sample ID	Onset potential (V vs Ag/AgCl)
$NaTaO_3$	- 0.34 (±0.02)
0.05% Cu:$NaTaO_3$	- 0.38 (±0.02)
0.1% Cu:$NaTaO_3$	- 0.34 (±0.02)
0.5% Cu:$NaTaO_3$	- 0.38 (±0.02)
1% Cu:$NaTaO_3$	- 0.38 (±0.02)
2.5% Cu:$NaTaO_3$	- 0.34 (±0.02)

To understand the charge mobility across the electrode-electrolyte interface during electrochemical analysis, EIS measurements were also performed in the frequency range of 0.01 Hz to 10 kHz with an alternating AC voltage of 20 mV. The EIS spectra can be useful in analyzing the electrochemical performance of the samples as capacitors. *Figure 3.28* displays the Nyquist plots of the samples signifying that these samples are not considered typical capacitor electrode materials. However, a depressed curve in the low-frequency range depicts that samples have some capacitive behavior.

Specifically, the Nyquist plots of each electrode were recorded in a 0.1 M NaOH electrolyte (pH = 13.4) under open circuit potential conditions (0 V vs Ag/AgCl), but also by applying DC potential (bias) to $-0.2, -0.5, -0.65, -0.8\, V\ vs\ Ag/AgCl$. The selection of these values was based on polarization curves. One value corresponds to the equilibrium of the system, the next value is close to the onset potential and the following ones are already able to overcome the energy barrier to carry out the reduction reaction.

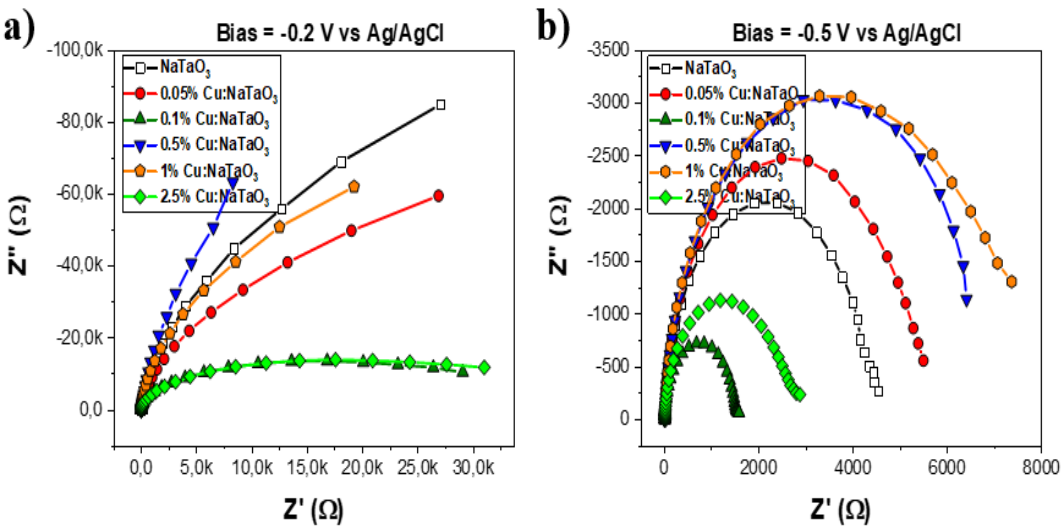

Figure 3.28: EIS vs frequency measurements. a) $-0.2\ V\ vs\ Ag/AgCl$ applied DC potential and b) $-0.5\ V\ vs\ Ag/AgCl$ applied DC potential. The black line corresponds to $NaTaO_3$. The red, olive, blue, orange, and green lines correspond to 0.05%, 0.1%, 0.5%, 1%, and 2.5% $Cu:NaTaO_3$, respectively.

In *Figure 3.28a*, $-0.2\ V\ vs\ Ag/AgCl$ has been applied to the system, which is not enough to start the reduction reaction. It is observed that all samples have huge impedance values in the order of 100 kΩ. The 0.1% and 2.5% $Cu:NaTaO_3$ seem, compared to the rest, to have better conductivity with the application of a small DC potential. When a larger bias is applied (*Figure 3.28b*), the carrier conductivity increases. In this particular case, the increase in charge mobility for the previous two samples is superior. Therefore, these two samples have the best electrocatalytic activity compared to the rest. It is worth noting that in the electrocatalytic evaluation of the materials, the mononuclear copper atoms as well as the case with the highest Cu loading, and thus the highest nanoclusters contribution show higher conductivities.

The CV plots of the samples at a sweep rate of 5 to 200 mV/s with the potential range of -0.2 to -0.8 V vs Ag/AgCl are shown in *Figure 3.29*. All curves exhibit quasi-rectangular shapes with slight distortion at these sweep rates, which is characteristic of faradaic reactions. CV measurements have been conducted for all samples, but for illustrative purposes, only the cases selected by EIS are shown.

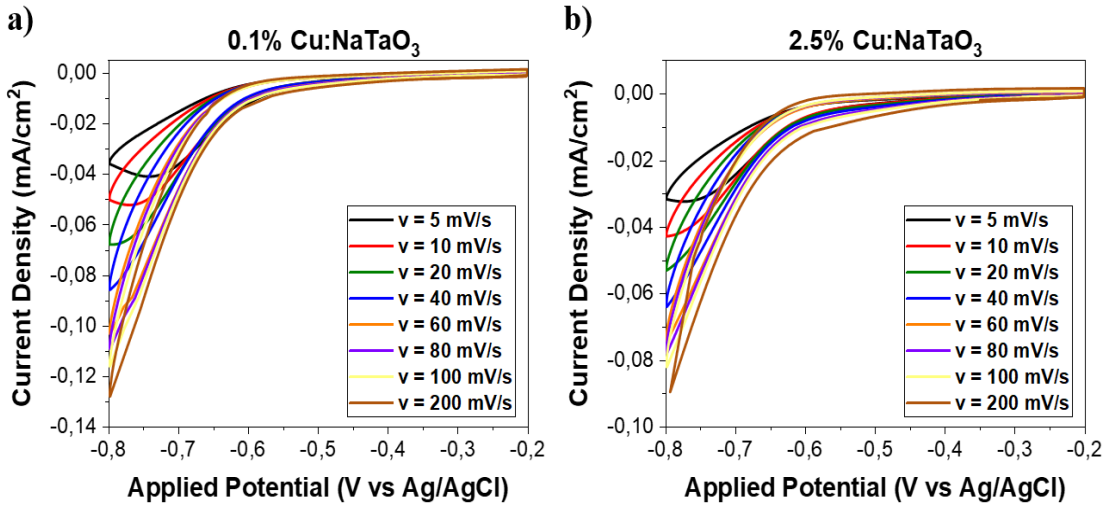

Figure 3.29: Cyclic Voltammetry plot of a) 0.1% Cu:$NaTaO_3$ and b) 2.5% Cu:$NaTaO_3$. The black, red, olive, blue, orange, violet, yellow, and brown lines correspond to 5, 10, 20, 40, 60, 80, 100 and 200 mV/s scan rate, respectively.

The symmetrical curve, indicative of reversible redox transitions, corresponding to the oxidative is not presented. The scan rates represent the reducing peak shift toward the greater and lower potentials in CV analysis. The current density, also, significantly improves as the scan rate goes from 5 to 200 mV/s, which denotes the interfacial properties of the electrode, the high ionic charge transport, and the cyclic stability at the electrode.

However, as the scan rate increases, most of the OH-ions diffuse to the outer surface rather than the inner surface of the samples, and therefore, the capacitance of the electrodes might depend upon amended interfacial activity due to effective ion transport over the surface of the samples.

Chapter 4

Conclusions

In this Master Thesis, we have developed high-conduction band photoactive nanostructures, interfaced with single atoms. Through Flame Spray Pyrolysis (FSP) technology we have synthesized, in a one-step process, sodium tantalate ($NaTaO_3$) perovskite structures, with a high degree of crystallinity, and high Specific Surface Area $(\sim 60\, m^2/g)$. Furthermore, these flame-made nanoparticles were in-situ interfaced with Copper (Cu) single atoms, using a novel deposition method.

The crystal phase composition (pure and stable perovskite nanostructures) and nanoparticles' size $(14\ nm)$ of the flame-made materials were evaluated by powder X-Ray Diffraction (pXRD). X-Ray Photoelectron Spectroscopy (XPS) was used to successfully detect Cu^{2+} atoms on the perovskite surface. Through Raman spectroscopy, we concluded that the particle formation process was not yet complete at the point of the interface of the nanoparticles with the copper atoms. As a result, as the Cu loading increases and nanoclusters are formed, the surface of the particles is distorted. Therefore, through the FSP process, it is achieved in *situ monitoring of Strong Metal-Support Interactions* (SMSI). UV-Vis Diffuse Reflectance Spectroscopy (DRS) was used to estimate the band gap energy of the semiconductors $\left(\mathrm{E_g} = 4\ eV\right)$. Electron Paramagnetic Resonance highlighted the materials where copper atoms have been successfully interfaced on the perovskite surface and those where Cu nanoclusters have been formed. It, also, provided detailed structural information, e.g., the coordination environment of Cu atoms ($4 - O$ region), and the estimation of the $\mathrm{Cu} - \mathrm{Cu}$ distance $\left(\sim 4.8\ \text{Å}\right)$.

The photocatalytic hydrogen production via water splitting showed an improved yield in the case of low Cu-loaded nanostructures and superior H_2 production yield in the case of formed Cu nanoclusters. The electrocatalytic activity obtained by Linear Sweep Voltammetry and Electrochemical Impedance Spectroscopy of the 0.1% & 2.5% Cu:$NaTaO_3$ samples was optimal compared to that of the rest of the investigated samples.

The present results set up the first FSP method for the controlled synthesis of nanostructures, interfaced with single atoms.

Chapter 5

Perspectives

In this Master Thesis, we have developed high-conduction band photoactive $NaTaO_3$ nanostructures, interfaced with single Cu atoms. Many alternations can modify the electronic and charge transfer properties of those materials studied in the current thesis. One of the next steps is the deposition of other single atoms, such as Bi or Sn atoms, but also organic molecules such as triphenylphosphine. The deposition of different atoms creates different surface interfaces which can aid or suppress redox reactions. Particular emphasis should be placed on Bi atoms, as it is known to have a high affinity to CO_2. The CO_2 reduction reaction, in any process, is one of the most widespread research fields today with thousands of researchers from different backgrounds engaged on a daily basis.

Another goal is to 'disrupt' the perovskite lattice. It is also known that oxygen vacancies in the lattice greatly aid hydrogen production as they contribute as active sites. The introduction of defects can be achieved in various ways through the FSP process. Additionally, two more direct studies can be made. First of all, the conditions should be expanded in order to overcome the thermodynamic limit of the size of the perovskite nanoparticles (12 nm), which until now has been achieved by our laboratory. Finally, the electrocatalytic Hydrogen Evolution Reaction (HER) is an immediate goal so as to achieve a complete relationship between the catalytic techniques.

References

(1) Feynman, R. P. There's Plenty of Room at the Bottom; 5; Engineering and Science, 1960; Vol. 23, pp 22–36.

(2) Durkan, C. *Size Really Does Matter: The Nanotechnology Revolution*; WORLD SCIENTIFIC (EUROPE), 2019. https://doi.org/10.1142/q0197.

(3) Pease, R. F. W.; Nixon, W. C. High Resolution Scanning Electron Microscopy. *J. Sci. Instrum.* **1965**, *42* (2), 81–85. https://doi.org/10.1088/0950-7671/42/2/305.

(4) Broers, A. N. A New High Resolution Reflection Scanning Electron Microscope. *Rev. Sci. Instrum.* **1969**, *40* (8), 1040–1045. https://doi.org/10.1063/1.1684146.

(5) Plows, G. S.; Nixon, W. C. Stroboscopic Scanning Electron Microscopy. *J. Phys. [E]* **1968**, *1* (6), 595–600. https://doi.org/10.1088/0022-3735/1/6/302.

(6) Cosslett, V. E. Scanning Microscopy with Electrons and X-Rays. *J. Electron Microsc. (Tokyo)* **1967**, *16* (1), 51–64.

(7) Žutić, I.; Fabian, J.; Das Sarma, S. Spintronics: Fundamentals and Applications. *Rev. Mod. Phys.* **2004**, *76* (2), 323–410. https://doi.org/10.1103/RevModPhys.76.323.

(8) Wolf, S. A.; Awschalom, D. D.; Buhrman, R. A.; Daughton, J. M.; Von Molnár, S.; Roukes, M. L.; Chtchelkanova, A. Y.; Treger, D. M. Spintronics: A Spin-Based Electronics Vision for the Future. *Science* **2001**, *294* (5546), 1488–1495. https://doi.org/10.1126/science.1065389.

(9) Tans, S. J.; Verschueren, A. R. M.; Dekker, C. Room-Temperature Transistor Based on a Single Carbon Nanotube. *Nature* **1998**, *393* (6680), 49–52. https://doi.org/10.1038/29954.

(10) Li, L.; Yu, Y.; Ye, G. J.; Ge, Q.; Ou, X.; Wu, H.; Feng, D.; Chen, X. H.; Zhang, Y. Black Phosphorus Field-Effect Transistors. *Nat. Nanotechnol.* **2014**, *9* (5), 372–377. https://doi.org/10.1038/nnano.2014.35.

(11) Luo, L.-W.; Ophir, N.; Chen, C. P.; Gabrielli, L. H.; Poitras, C. B.; Bergmen, K.; Lipson, M. WDM-Compatible Mode-Division Multiplexing on a Silicon Chip. *Nat. Commun.* **2014**, *5* (1), 3069. https://doi.org/10.1038/ncomms4069.

(12) Du, J.; Blanche, T. J.; Harrison, R. R.; Lester, H. A.; Masmanidis, S. C. Multiplexed, High Density Electrophysiology with Nanofabricated Neural Probes. *PLoS ONE* **2011**, *6* (10), e26204. https://doi.org/10.1371/journal.pone.0026204.

(13) Vlad, A.; Reddy, A. L. M.; Ajayan, A.; Singh, N.; Gohy, J.-F.; Melinte, S.; Ajayan, P. M. Roll up Nanowire Battery from Silicon Chips. *Proc. Natl. Acad. Sci.* **2012**, *109* (38), 15168–15173. https://doi.org/10.1073/pnas.1208638109.

(14) Langer, R.; Tirrell, D. A. Designing Materials for Biology and Medicine. *Nature* **2004**, *428* (6982), 487–492. https://doi.org/10.1038/nature02388.

(15) Hirsch, L. R.; Stafford, R. J.; Bankson, J. A.; Sershen, S. R.; Rivera, B.; Price, R. E.; Hazle, J. D.; Halas, N. J.; West, J. L. Nanoshell-Mediated near-Infrared Thermal Therapy of Tumors under Magnetic Resonance Guidance. *Proc. Natl. Acad. Sci.* **2003**, *100* (23), 13549–13554. https://doi.org/10.1073/pnas.2232479100.

(16) Shi, J.; Kantoff, P. W.; Wooster, R.; Farokhzad, O. C. Cancer Nanomedicine: Progress, Challenges and Opportunities. *Nat. Rev. Cancer* **2017**, *17* (1), 20–37. https://doi.org/10.1038/nrc.2016.108.

(17) Peppas, N. A.; Hilt, J. Z.; Khademhosseini, A.; Langer, R. Hydrogels in Biology and Medicine: From Molecular Principles to Bionanotechnology. *Adv. Mater.* **2006**, *18* (11), 1345–1360. https://doi.org/10.1002/adma.200501612.
(18) Nel, A.; Xia, T.; Mädler, L.; Li, N. Toxic Potential of Materials at the Nanolevel. *Science* **2006**, *311* (5761), 622–627. https://doi.org/10.1126/science.1114397.
(19) Simon, P.; Gogotsi, Y. Materials for Electrochemical Capacitors. *Nat. Mater.* **2008**, *7* (11), 845–854. https://doi.org/10.1038/nmat2297.
(20) Aricò, A. S.; Bruce, P.; Scrosati, B.; Tarascon, J.-M.; Van Schalkwijk, W. Nanostructured Materials for Advanced Energy Conversion and Storage Devices. *Nat. Mater.* **2005**, *4* (5), 366–377. https://doi.org/10.1038/nmat1368.
(21) Bruce, P. G.; Scrosati, B.; Tarascon, J.-M. Nanomaterials for Rechargeable Lithium Batteries. *Angew. Chem. Int. Ed.* **2008**, *47* (16), 2930–2946. https://doi.org/10.1002/anie.200702505.
(22) Dunn, B.; Kamath, H.; Tarascon, J.-M. Electrical Energy Storage for the Grid: A Battery of Choices. *Science* **2011**, *334* (6058), 928–935. https://doi.org/10.1126/science.1212741.
(23) Barnes, W. L.; Dereux, A.; Ebbesen, T. W. Surface Plasmon Subwavelength Optics. *Nature* **2003**, *424* (6950), 824–830. https://doi.org/10.1038/nature01937.
(24) Tong, H.; Ouyang, S.; Bi, Y.; Umezawa, N.; Oshikiri, M.; Ye, J. Nano-Photocatalytic Materials: Possibilities and Challenges. *Adv. Mater.* **2012**, *24* (2), 229–251. https://doi.org/10.1002/adma.201102752.
(25) Wang, Q. H.; Kalantar-Zadeh, K.; Kis, A.; Coleman, J. N.; Strano, M. S. Electronics and Optoelectronics of Two-Dimensional Transition Metal Dichalcogenides. *Nat. Nanotechnol.* **2012**, *7* (11), 699–712. https://doi.org/10.1038/nnano.2012.193.
(26) Balasubramaniam, S.; Kangasharju, J. Realizing the Internet of Nano Things: Challenges, Solutions, and Applications. *Computer* **2013**, *46* (2), 62–68. https://doi.org/10.1109/MC.2012.389.
(27) Afsana, F.; Asif-Ur-Rahman, Md.; Ahmed, M. R.; Mahmud, M.; Kaiser, M. S. An Energy Conserving Routing Scheme for Wireless Body Sensor Nanonetwork Communication. *IEEE Access* **2018**, *6*, 9186–9200. https://doi.org/10.1109/ACCESS.2018.2789437.
(28) Kuscu, M.; Akan, O. B. A Communication Theoretical Analysis of FRET-Based Mobile Ad Hoc Molecular Nanonetworks. *IEEE Trans. NanoBioscience* **2014**, *13* (3), 255–266. https://doi.org/10.1109/TNB.2014.2329178.
(29) Canovas-Carrasco, S.; Garcia-Sanchez, A.-J.; Garcia-Haro, J. On the Nature of Energy-Feasible Wireless Nanosensor Networks. *Sensors* **2018**, *18* (5), 1356. https://doi.org/10.3390/s18051356.
(30) Farokhzad, O. C.; Langer, R. Impact of Nanotechnology on Drug Delivery. *ACS Nano* **2009**, *3* (1), 16–20. https://doi.org/10.1021/nn900002m.
(31) De Jong, W. H.; Borm, P. J. A. Drug Delivery and Nanoparticles:Applications and Hazards. *Int. J. Nanomedicine* **2008**, *3* (2), 133–149. https://doi.org/10.2147/ijn.s596.
(32) Allen, T. M.; Cullis, P. R. Drug Delivery Systems: Entering the Mainstream. *Science* **2004**, *303* (5665), 1818–1822. https://doi.org/10.1126/science.1095833.
(33) Allen, T. M.; Cullis, P. R. Liposomal Drug Delivery Systems: From Concept to Clinical Applications. *Adv. Drug Deliv. Rev.* **2013**, *65* (1), 36–48. https://doi.org/10.1016/j.addr.2012.09.037.

(34) Schmaljohann, D. Thermo- and PH-Responsive Polymers in Drug Delivery☆. *Adv. Drug Deliv. Rev.* **2006**, *58* (15), 1655–1670. https://doi.org/10.1016/j.addr.2006.09.020.
(35) Kroto, H. W. C60B Buckminsterfullerene, Other Fullerenes and the Icospiral Shell. *Comput. Math. Appl.* **1989**, *17* (1–3), 417–423. https://doi.org/10.1016/0898-1221(89)90171-5.
(36) Kroto, H. C60, Fullerenes, Giant Fullerenes and Soot. *Pure Appl. Chem.* **1990**, *62* (3), 407–415. https://doi.org/10.1351/pac199062030407.
(37) Pradeep, T.; Rao, C. N. R. Preparation of Buckminsterfullerene, C60. *Mater. Res. Bull.* **1991**, *26* (10), 1101–1105. https://doi.org/10.1016/0025-5408(91)90094-3.
(38) Ebbesen, T. W.; Ajayan, P. M. Large-Scale Synthesis of Carbon Nanotubes. *Nature* **1992**, *358* (6383), 220–222. https://doi.org/10.1038/358220a0.
(39) Nasrollahzadeh, M.; Sajadi, S. M.; Sajjadi, M.; Issaabadi, Z. Applications of Nanotechnology in Daily Life. In *Interface Science and Technology*; Elsevier, 2019; Vol. 28, pp 113–143. https://doi.org/10.1016/B978-0-12-813586-0.00004-3.
(40) Ruoff, R. S.; Tersoff, J.; Lorents, D. C.; Subramoney, S.; Chan, B. Radial Deformation of Carbon Nanotubes by van Der Waals Forces. *Nature* **1993**, *364* (6437), 514–516. https://doi.org/10.1038/364514a0.
(41) Östling, D.; RosÉn, A.; Apell, P.; Mukhopadhyay, G. Plasmons in C $_{60}$, Carbon Onions and Carbon Tubes. *MRS Proc.* **1994**, *349*, 235. https://doi.org/10.1557/PROC-349-235.
(42) Alivisatos, A. P. Semiconductor Clusters, Nanocrystals, and Quantum Dots. *Science* **1996**, *271* (5251), 933–937. https://doi.org/10.1126/science.271.5251.933.
(43) Chan, W. C. W.; Nie, S. Quantum Dot Bioconjugates for Ultrasensitive Nonisotopic Detection. *Science* **1998**, *281* (5385), 2016–2018. https://doi.org/10.1126/science.281.5385.2016.
(44) Glazer, A. M. **Perovskites Modern and Ancient** . By Roger H. Mitchell.Thunder Bay, Ontario: AlmazPress, 2002. Price USD 70.00. ISBN0-9689411-0-9. *Acta Crystallogr. B* **2002**, *58* (6), 1075–1075. https://doi.org/10.1107/S0108768102020220.
(45) Dandia, A.; Saini, P.; Sharma, R.; Parewa, V. Visible Light Driven Perovskite-Based Photocatalysts: A New Candidate for Green Organic Synthesis by Photochemical Protocol. *Curr. Res. Green Sustain. Chem.* **2020**, *3*, 100031. https://doi.org/10.1016/j.crgsc.2020.100031.
(46) Zhao, X.-G.; Yang, D.; Ren, J.-C.; Sun, Y.; Xiao, Z.; Zhang, L. Rational Design of Halide Double Perovskites for Optoelectronic Applications. *Joule* **2018**, *2* (9), 1662–1673. https://doi.org/10.1016/j.joule.2018.06.017.
(47) Bati, A. S. R.; Zhong, Y. L.; Burn, P. L.; Nazeeruddin, M. K.; Shaw, P. E.; Batmunkh, M. Next-Generation Applications for Integrated Perovskite Solar Cells. *Commun. Mater.* **2023**, *4* (1), 2. https://doi.org/10.1038/s43246-022-00325-4.
(48) Millis, A. J. Lattice Effects in Magnetoresistive Manganese Perovskites. *Nature* **1998**, *392* (6672), 147–150. https://doi.org/10.1038/32348.
(49) Saparov, B.; Mitzi, D. B. Organic–Inorganic Perovskites: Structural Versatility for Functional Materials Design. *Chem. Rev.* **2016**, *116* (7), 4558–4596. https://doi.org/10.1021/acs.chemrev.5b00715.

(50) Eames, C.; Frost, J. M.; Barnes, P. R. F.; O'Regan, B. C.; Walsh, A.; Islam, M. S. Ionic Transport in Hybrid Lead Iodide Perovskite Solar Cells. *Nat. Commun.* **2015**, *6* (1), 7497. https://doi.org/10.1038/ncomms8497.
(51) Akkerman, Q. A.; D'Innocenzo, V.; Accornero, S.; Scarpellini, A.; Petrozza, A.; Prato, M.; Manna, L. Tuning the Optical Properties of Cesium Lead Halide Perovskite Nanocrystals by Anion Exchange Reactions. *J. Am. Chem. Soc.* **2015**, *137* (32), 10276–10281. https://doi.org/10.1021/jacs.5b05602.
(52) Kharton, V.; Marques, F.; Atkinson, A. Transport Properties of Solid Oxide Electrolyte Ceramics: A Brief Review. *Solid State Ion.* **2004**, *174* (1–4), 135–149. https://doi.org/10.1016/j.ssi.2004.06.015.
(53) Brenner, T. M.; Egger, D. A.; Kronik, L.; Hodes, G.; Cahen, D. Hybrid Organic—Inorganic Perovskites: Low-Cost Semiconductors with Intriguing Charge-Transport Properties. *Nat. Rev. Mater.* **2016**, *1* (1), 15007. https://doi.org/10.1038/natrevmats.2015.7.
(54) Yoo, J. J.; Seo, G.; Chua, M. R.; Park, T. G.; Lu, Y.; Rotermund, F.; Kim, Y.-K.; Moon, C. S.; Jeon, N. J.; Correa-Baena, J.-P.; Bulović, V.; Shin, S. S.; Bawendi, M. G.; Seo, J. Efficient Perovskite Solar Cells via Improved Carrier Management. *Nature* **2021**, *590* (7847), 587–593. https://doi.org/10.1038/s41586-021-03285-w.
(55) Junquera, J.; Ghosez, P. Critical Thickness for Ferroelectricity in Perovskite Ultrathin Films. *Nature* **2003**, *422* (6931), 506–509. https://doi.org/10.1038/nature01501.
(56) Kreuer, K. D. On the Development of Proton Conducting Materials for Technological Applications. *Solid State Ion.* **1997**, *97* (1–4), 1–15. https://doi.org/10.1016/S0167-2738(97)00082-9.
(57) Jung, H. S.; Park, N.-G. Perovskite Solar Cells: From Materials to Devices. *Small* **2015**, *11* (1), 10–25. https://doi.org/10.1002/smll.201402767.
(58) You, J.; Meng, L.; Song, T.-B.; Guo, T.-F.; Yang, Y. (Michael); Chang, W.-H.; Hong, Z.; Chen, H.; Zhou, H.; Chen, Q.; Liu, Y.; De Marco, N.; Yang, Y. Improved Air Stability of Perovskite Solar Cells via Solution-Processed Metal Oxide Transport Layers. *Nat. Nanotechnol.* **2016**, *11* (1), 75–81. https://doi.org/10.1038/nnano.2015.230.
(59) Yin, W.-J.; Yang, J.-H.; Kang, J.; Yan, Y.; Wei, S.-H. Halide Perovskite Materials for Solar Cells: A Theoretical Review. *J. Mater. Chem. A* **2015**, *3* (17), 8926–8942. https://doi.org/10.1039/C4TA05033A.
(60) Saha, S.; Sinha, T. P.; Mookerjee, A. Electronic Structure, Chemical Bonding, and Optical Properties of Paraelectric BaTiO 3. *Phys. Rev. B* **2000**, *62* (13), 8828–8834. https://doi.org/10.1103/PhysRevB.62.8828.
(61) Shamsi, J.; Urban, A. S.; Imran, M.; De Trizio, L.; Manna, L. Metal Halide Perovskite Nanocrystals: Synthesis, Post-Synthesis Modifications, and Their Optical Properties. *Chem. Rev.* **2019**, *119* (5), 3296–3348. https://doi.org/10.1021/acs.chemrev.8b00644.
(62) Homes, C. C.; Vogt, T.; Shapiro, S. M.; Wakimoto, S.; Ramirez, A. P. Optical Response of High-Dielectric-Constant Perovskite-Related Oxide. *Science* **2001**, *293* (5530), 673–676. https://doi.org/10.1126/science.1061655.
(63) Subramanian, M. A.; Li, D.; Duan, N.; Reisner, B. A.; Sleight, A. W. High Dielectric Constant in ACu3Ti4O12 and ACu3Ti3FeO12 Phases. *J. Solid State Chem.* **2000**, *151* (2), 323–325. https://doi.org/10.1006/jssc.2000.8703.

(64) Panda, P. K. Review: Environmental Friendly Lead-Free Piezoelectric Materials. *J. Mater. Sci.* **2009**, *44* (19), 5049–5062. https://doi.org/10.1007/s10853-009-3643-0.
(65) Cohen, R. E. Origin of Ferroelectricity in Perovskite Oxides. *Nature* **1992**, *358* (6382), 136–138. https://doi.org/10.1038/358136a0.
(66) Hwang, J.; Rao, R. R.; Giordano, L.; Katayama, Y.; Yu, Y.; Shao-Horn, Y. Perovskites in Catalysis and Electrocatalysis. *Science* **2017**, *358* (6364), 751–756. https://doi.org/10.1126/science.aam7092.
(67) Jeyalakshmi, V.; Mahalakshmy, R.; Ramesh, K.; Rao, P. V. C.; Choudary, N. V.; Thirunavukkarasu, K.; Krishnamurthy, K. R.; Viswanathan, B. Metal Oxides as Photo Catalysts: Modified Sodium Tantalate as Catalyst for Photo Reduction of Carbon Dioxide. *Mol. Catal.* **2018**, *451*, 105–113. https://doi.org/10.1016/j.mcat.2017.11.021.
(68) Lee, Y.-C.; Teng, H.; Hu, C.-C.; Hu, S.-Y. Temperature-Dependent Photoluminescence in NaTaO[Sub 3] with Different Crystalline Structures. *Electrochem. Solid-State Lett.* **2008**, *11* (2), P1. https://doi.org/10.1149/1.2817476.
(69) Uniyal, M.; Bhatt, S. C.; Kashyap, S. Dielectric Properties of Sodium Potassium Tantalate Mixed System; Bahal, India, 2019; p 040012. https://doi.org/10.1063/1.5122349.
(70) Farooq, U.; Ahmed, J.; Alshehri, S. M.; Ahmad, T. High-Surface-Area Sodium Tantalate Nanoparticles with Enhanced Photocatalytic and Electrical Properties Prepared through Polymeric Citrate Precursor Route. *ACS Omega* **2019**, *4* (21), 19408–19419. https://doi.org/10.1021/acsomega.9b02830.
(71) Shanker, V.; Samal, S. L.; Pradhan, G. K.; Narayana, C.; Ganguli, A. K. Nanocrystalline NaNbO3 and NaTaO3: Rietveld Studies, Raman Spectroscopy and Dielectric Properties. *Solid State Sci.* **2009**, *11* (2), 562–569. https://doi.org/10.1016/j.solidstatesciences.2008.08.001.
(72) Hu, C.-C.; Teng, H. Influence of Structural Features on the Photocatalytic Activity of NaTaO3 Powders from Different Synthesis Methods. *Appl. Catal. Gen.* **2007**, *331*, 44–50. https://doi.org/10.1016/j.apcata.2007.07.024.
(73) Porob, D. G.; Maggard, P. A. Flux Syntheses of La-Doped NaTaO3 and Its Photocatalytic Activity. *J. Solid State Chem.* **2006**, *179* (6), 1727–1732. https://doi.org/10.1016/j.jssc.2006.03.008.
(74) Kato, H.; Kudo, A. Water Splitting into H_2 and O_2 on Alkali Tantalate Photocatalysts $ATaO_3$ (A = Li, Na, and K). *J. Phys. Chem. B* **2001**, *105* (19), 4285–4292. https://doi.org/10.1021/jp004386b.
(75) Kudo, A.; Kato, H.; Nakagawa, S. Water Splitting into H_2 and O_2 on New $Sr_2M_2O_7$ (M = Nb and Ta) Photocatalysts with Layered Perovskite Structures: Factors Affecting the Photocatalytic Activity. *J. Phys. Chem. B* **2000**, *104* (3), 571–575. https://doi.org/10.1021/jp9919056.
(76) Kato, H.; Asakura, K.; Kudo, A. Highly Efficient Water Splitting into H_2 and O_2 over Lanthanum-Doped $NaTaO_3$ Photocatalysts with High Crystallinity and Surface Nanostructure. *J. Am. Chem. Soc.* **2003**, *125* (10), 3082–3089. https://doi.org/10.1021/ja027751g.
(77) Kudo, A.; Kato, H. Effect of Lanthanide-Doping into NaTaO3 Photocatalysts for Efficient Water Splitting. *Chem. Phys. Lett.* **2000**, *331* (5–6), 373–377. https://doi.org/10.1016/S0009-2614(00)01220-3.

(78) Aguas, M. D.; Parkin, I. P. Combined Combustion Sol-Gel Synthesis of LiNbO3, LiTaO3, NaNbO3 and NaTaO3. *J. Mater. Sci. Lett.* **2001**, *20* (1), 57–58. https://doi.org/10.1023/A:1006766816091.
(79) Torres-Martínez, L. M.; Cruz-López, A.; Juárez-Ramírez, I.; Meza-de La Rosa, Ma. E. Methylene Blue Degradation by NaTaO3 Sol–Gel Doped with Sm and La. *J. Hazard. Mater.* **2009**, *165* (1–3), 774–779. https://doi.org/10.1016/j.jhazmat.2008.10.060.
(80) Karna, S.; Saunders, C.; Karna, R.; Guragain, D.; Mishra, S.; Karna, P. Hydrothermal Synthesis of Carbon and Sulfur Mono-Doped Sodium Tantalates. *PeerJ Mater. Sci.* **2020**, *2*, e10. https://doi.org/10.7717/peerj-matsci.10.
(81) Li, X.; Zang, J. Facile Hydrothermal Synthesis of Sodium Tantalate ($NaTaO_3$) Nanocubes and High Photocatalytic Properties. *J. Phys. Chem. C* **2009**, *113* (45), 19411–19418. https://doi.org/10.1021/jp907334z.
(82) Xu, J.; Xue, D.; Yan, C. Chemical Synthesis of NaTaO3 Powder at Low-Temperature. *Mater. Lett.* **2005**, *59* (23), 2920–2922. https://doi.org/10.1016/j.matlet.2005.04.043.
(83) Psathas, P.; Moularas, C.; Smykała, S.; Deligiannakis, Y. Highly Crystalline Nanosized $NaTaO_3$ /NiO Heterojunctions Engineered by Double-Nozzle Flame Spray Pyrolysis for Solar-to-H_2 Conversion: Toward Industrial-Scale Synthesis. *ACS Appl. Nano Mater.* **2023**, *6* (4), 2658–2671. https://doi.org/10.1021/acsanm.2c05066.
(84) Kang, H. W.; Kim, E.-J.; Park, S. B. Preparation of NaTaO 3 by Spray Pyrolysis and Evaluation of Apparent Photocatalytic Activity for Hydrogen Production from Water. *Int. J. Photoenergy* **2008**, *2008*, 1–8. https://doi.org/10.1155/2008/519643.
(85) An, L.; Onishi, H. Electron–Hole Recombination Controlled by Metal Doping Sites in $NaTaO_3$ Photocatalysts. *ACS Catal.* **2015**, *5* (6), 3196–3206. https://doi.org/10.1021/acscatal.5b00484.
(86) Konstantinou, I. K.; Albanis, T. A. TiO2-Assisted Photocatalytic Degradation of Azo Dyes in Aqueous Solution: Kinetic and Mechanistic Investigations. *Appl. Catal. B Environ.* **2004**, *49* (1), 1–14. https://doi.org/10.1016/j.apcatb.2003.11.010.
(87) Liang, Y.; Li, Y.; Wang, H.; Zhou, J.; Wang, J.; Regier, T.; Dai, H. Co3O4 Nanocrystals on Graphene as a Synergistic Catalyst for Oxygen Reduction Reaction. *Nat. Mater.* **2011**, *10* (10), 780–786. https://doi.org/10.1038/nmat3087.
(88) Guo, S.; Zhang, S.; Sun, S. Tuning Nanoparticle Catalysis for the Oxygen Reduction Reaction. *Angew. Chem. Int. Ed.* **2013**, *52* (33), 8526–8544. https://doi.org/10.1002/anie.201207186.
(89) Nahar, S.; Zain, M.; Kadhum, A.; Hasan, H.; Hasan, Md. Advances in Photocatalytic CO2 Reduction with Water: A Review. *Materials* **2017**, *10* (6), 629. https://doi.org/10.3390/ma10060629.
(90) Li, Y.; Wang, H.; Xie, L.; Liang, Y.; Hong, G.; Dai, H. MoS_2 Nanoparticles Grown on Graphene: An Advanced Catalyst for the Hydrogen Evolution Reaction. *J. Am. Chem. Soc.* **2011**, *133* (19), 7296–7299. https://doi.org/10.1021/ja201269b.
(91) Sheng, W.; Gasteiger, H. A.; Shao-Horn, Y. Hydrogen Oxidation and Evolution Reaction Kinetics on Platinum: Acid vs Alkaline Electrolytes. *J. Electrochem. Soc.* **2010**, *157* (11), B1529. https://doi.org/10.1149/1.3483106.
(92) Nakanishi, H.; Iizuka, K.; Takayama, T.; Iwase, A.; Kudo, A. Highly Active $NaTaO_3$ -Based Photocatalysts for CO_2 Reduction to Form CO Using Water as

the Electron Donor. *ChemSusChem* **2017**, *10* (1), 112–118. https://doi.org/10.1002/cssc.201601360.
(93) Li, M.; Li, P.; Chang, K.; Wang, T.; Liu, L.; Kang, Q.; Ouyang, S.; Ye, J. Highly Efficient and Stable Photocatalytic Reduction of CO_2 to CH_4 over Ru Loaded $NaTaO_3$. *Chem. Commun.* **2015**, *51* (36), 7645–7648. https://doi.org/10.1039/C5CC01124H.
(94) Edalati, K.; Fujiwara, K.; Takechi, S.; Wang, Q.; Arita, M.; Watanabe, M.; Sauvage, X.; Ishihara, T.; Horita, Z. Improved Photocatalytic Hydrogen Evolution on Tantalate Perovskites $CsTaO_3$ and $LiTaO_3$ by Strain-Induced Vacancies. *ACS Appl. Energy Mater.* **2020**, *3* (2), 1710–1718. https://doi.org/10.1021/acsaem.9b02197.
(95) George, S. M. Atomic Layer Deposition: An Overview. *Chem. Rev.* **2010**, *110* (1), 111–131. https://doi.org/10.1021/cr900056b.
(96) Li, X.; Cai, W.; An, J.; Kim, S.; Nah, J.; Yang, D.; Piner, R.; Velamakanni, A.; Jung, I.; Tutuc, E.; Banerjee, S. K.; Colombo, L.; Ruoff, R. S. Large-Area Synthesis of High-Quality and Uniform Graphene Films on Copper Foils. *Science* **2009**, *324* (5932), 1312–1314. https://doi.org/10.1126/science.1171245.
(97) Harman, T. C.; Taylor, P. J.; Walsh, M. P.; LaForge, B. E. Quantum Dot Superlattice Thermoelectric Materials and Devices. *Science* **2002**, *297* (5590), 2229–2232. https://doi.org/10.1126/science.1072886.
(98) Zhao, Y.; Jiang, W.; Zhang, J.; Lovell, E. C.; Amal, R.; Han, Z.; Lu, X. Anchoring Sites Engineering in Single-Atom Catalysts for Highly Efficient Electrochemical Energy Conversion Reactions. *Adv. Mater.* **2021**, *33* (41), 2102801. https://doi.org/10.1002/adma.202102801.
(99) Zindrou, A.; Belles, L.; Deligiannakis, Y. Cu-Based Materials as Photocatalysts for Solar Light Artificial Photosynthesis: Aspects of Engineering Performance, Stability, Selectivity. *Solar* **2023**, *3* (1), 87–112. https://doi.org/10.3390/solar3010008.
(100) Cai, J.; Zhang, Y.; Dong, H.; Zhou, X. First-Principles Investigation on Electronic Properties and Surface Reactions of $NaTaO_3$ Adsorbed with Single-Metal Atoms. *J. Phys. Chem. C* **2023**, *127* (14), 6702–6713. https://doi.org/10.1021/acs.jpcc.3c00008.
(101) Vallero, D. A. Pollution Revisited. In *Paradigms Lost*; Elsevier, 2006; pp 55–94. https://doi.org/10.1016/B978-075067888-9/50003-X.
(102) Lejano, R. P. Urban Environmental Quality: Perceptions and Measures. In *Encyclopedia of Environmental Health*; Elsevier, 2011; pp 541–548. https://doi.org/10.1016/B978-0-444-52272-6.00227-0.
(103) Ashcroft, N. W.; Mermin, N. D. *Solid State Physics*; Holt, Rinehart and Winston: New York, 1976.
(104) Hisatomi, T.; Kubota, J.; Domen, K. Recent Advances in Semiconductors for Photocatalytic and Photoelectrochemical Water Splitting. *Chem Soc Rev* **2014**, *43* (22), 7520–7535. https://doi.org/10.1039/C3CS60378D.
(105) Grabowska, E. Selected Perovskite Oxides: Characterization, Preparation and Photocatalytic Properties—A Review. *Appl. Catal. B Environ.* **2016**, *186*, 97–126. https://doi.org/10.1016/j.apcatb.2015.12.035.
(106) Chen, S.; Takata, T.; Domen, K. Particulate Photocatalysts for Overall Water Splitting. *Nat. Rev. Mater.* **2017**, *2* (10), 17050. https://doi.org/10.1038/natrevmats.2017.50.

(107) Pratsinis, S. E. Flame Aerosol Synthesis of Ceramic Powders. *Prog. Energy Combust. Sci.* **1998**, *24* (3), 197–219. https://doi.org/10.1016/S0360-1285(97)00028-2.
(108) Teoh, W. Y.; Amal, R.; Mädler, L. Flame Spray Pyrolysis: An Enabling Technology for Nanoparticles Design and Fabrication. *Nanoscale* **2010**, *2* (8), 1324. https://doi.org/10.1039/c0nr00017e.
(109) Mueller, R.; Mädler, L.; Pratsinis, S. E. Nanoparticle Synthesis at High Production Rates by Flame Spray Pyrolysis. *Chem. Eng. Sci.* **2003**, *58* (10), 1969–1976. https://doi.org/10.1016/S0009-2509(03)00022-8.
(110) Mädler, L.; Kammler, H. K.; Mueller, R.; Pratsinis, S. E. Controlled Synthesis of Nanostructured Particles by Flame Spray Pyrolysis. *J. Aerosol Sci.* **2002**, *33* (2), 369–389. https://doi.org/10.1016/S0021-8502(01)00159-8.
(111) *Handbook of Atomization and Sprays: Theory and Applications*; Ashgriz, N., Ed.; Springer US: Boston, MA, 2011. https://doi.org/10.1007/978-1-4419-7264-4.
(112) Donnelly, T. D.; Hogan, J.; Mugler, A.; Schommer, N.; Schubmehl, M.; Bernoff, A. J.; Forrest, B. An Experimental Study of Micron-Scale Droplet Aerosols Produced via Ultrasonic Atomization. *Phys. Fluids* **2004**, *16* (8), 2843–2851. https://doi.org/10.1063/1.1759271.
(113) Gañán-Calvo, A. M.; Dávila, J.; Barrero, A. Current and Droplet Size in the Electrospraying of Liquids. Scaling Laws. *J. Aerosol Sci.* **1997**, *28* (2), 249–275. https://doi.org/10.1016/S0021-8502(96)00433-8.
(114) Liu, H.-F.; Gong, X.; Li, W.-F.; Wang, F.-C.; Yu, Z.-H. Prediction of Droplet Size Distribution in Sprays of Prefilming Air-Blast Atomizers. *Chem. Eng. Sci.* **2006**, *61* (6), 1741–1747. https://doi.org/10.1016/j.ces.2005.10.012.
(115) Koirala, R.; Pratsinis, S. E.; Baiker, A. Synthesis of Catalytic Materials in Flames: Opportunities and Challenges. *Chem. Soc. Rev.* **2016**, *45* (11), 3053–3068. https://doi.org/10.1039/C5CS00011D.
(116) Rader, D. J.; McMurry, P. H. Application of the Tandem Differential Mobility Analyzer to Studies of Droplet Growth or Evaporation. *J. Aerosol Sci.* **1986**, *17* (5), 771–787. https://doi.org/10.1016/0021-8502(86)90031-5.
(117) Lu, Y.; Fan, H.; Stump, A.; Ward, T. L.; Rieker, T.; Brinker, C. J. Aerosol-Assisted Self-Assembly of Mesostructured Spherical Nanoparticles. *Nature* **1999**, *398* (6724), 223–226. https://doi.org/10.1038/18410.
(118) Vehring, R.; Foss, W. R.; Lechuga-Ballesteros, D. Particle Formation in Spray Drying. *J. Aerosol Sci.* **2007**, *38* (7), 728–746. https://doi.org/10.1016/j.jaerosci.2007.04.005.
(119) McGraw, R. Description of Aerosol Dynamics by the Quadrature Method of Moments. *Aerosol Sci. Technol.* **1997**, *27* (2), 255–265. https://doi.org/10.1080/02786829708965471.
(120) Ervens, B.; Turpin, B. J.; Weber, R. J. Secondary Organic Aerosol Formation in Cloud Droplets and Aqueous Particles (AqSOA): A Review of Laboratory, Field and Model Studies. *Atmospheric Chem. Phys.* **2011**, *11* (21), 11069–11102. https://doi.org/10.5194/acp-11-11069-2011.
(121) Jossen, R.; Pratsinis, S. E.; Stark, W. J.; Madler, L. Criteria for Flame-Spray Synthesis of Hollow, Shell-Like, or Inhomogeneous Oxides. *J. Am. Ceram. Soc.* **2005**, *88* (6), 1388–1393. https://doi.org/10.1111/j.1551-2916.2005.00249.x.
(122) Buesser, B.; Gröhn, A. J. Multiscale Aspects of Modeling Gas-Phase Nanoparticle Synthesis. *Chem. Eng. Technol.* **2012**, *35* (7), 1133–1143. https://doi.org/10.1002/ceat.201100723.

(123) Ferri, D.; Heel, A.; Burnat, D. Aerosol Spray Synthesis of Powder Perovskite-Type Oxides. In *Perovskites and Related Mixed Oxides*; Granger, P., Parvulescu, V. I., Parvulescu, V. I., Prellier, W., Eds.; Wiley-VCH Verlag GmbH & Co. KGaA: Weinheim, Germany, 2015; pp 69–90. https://doi.org/10.1002/9783527686605.ch04.
(124) Strobel, R.; Pratsinis, S. E. Flame Aerosol Synthesis of Smart Nanostructured Materials. *J. Mater. Chem.* **2007**, *17* (45), 4743. https://doi.org/10.1039/b711652g.
(125) Trommer, R. M.; Bergmann, C. P. *Flame Spray Technology: Method for Production of Nanopowders*; Topics in Mining, Metallurgy and Materials Engineering; Springer Berlin Heidelberg: Berlin, Heidelberg, 2015. https://doi.org/10.1007/978-3-662-47162-3.
(126) Ulrich, G. D. Theory of Particle Formation and Growth in Oxide Synthesis Flames. *Combust. Sci. Technol.* **1971**, *4* (1), 47–57. https://doi.org/10.1080/00102207108952471.
(127) Okuyama, K.; Kousaka, Y.; Tohge, N.; Yamamoto, S.; Wu, J. J.; Flagan, R. C.; Seinfeld, J. H. Production of Ultrafine Metal Oxide Aerosol Particles by Thermal Decomposition of Metal Alkoxide Vapors. *AIChE J.* **1986**, *32* (12), 2010–2019. https://doi.org/10.1002/aic.690321211.
(128) Pratsinis, S. E. Aerosol-Based Technologies in Nanoscale Manufacturing: From Functional Materials to Devices through Core Chemical Engineering. *AIChE J.* **2010**, *56* (12), 3028–3035. https://doi.org/10.1002/aic.12478.
(129) Kruis, F. E.; Kusters, K. A.; Pratsinis, S. E.; Scarlett, B. A Simple Model for the Evolution of the Characteristics of Aggregate Particles Undergoing Coagulation and Sintering. *Aerosol Sci. Technol.* **1993**, *19* (4), 514–526. https://doi.org/10.1080/02786829308959656.
(130) Sreethawong, T.; Ngamsinlapasathian, S.; Suzuki, Y.; Yoshikawa, S. Nanocrystalline Mesoporous Ta2O5-Based Photocatalysts Prepared by Surfactant-Assisted Templating Sol–Gel Process for Photocatalytic H2 Evolution. *J. Mol. Catal. Chem.* **2005**, *235* (1–2), 1–11. https://doi.org/10.1016/j.molcata.2005.03.021.
(131) Hu, C.-C.; Teng, H. Influence of Structural Features on the Photocatalytic Activity of NaTaO3 Powders from Different Synthesis Methods. *Appl. Catal. Gen.* **2007**, *331*, 44–50. https://doi.org/10.1016/j.apcata.2007.07.024.
(132) Duan, J.; Shi, W.; Xu, L.; Mou, G.; Xin, Q.; Guan, J. Hierarchical Nanostructures of Fluorinated and Naked Ta2O5 Single Crystalline Nanorods: Hydrothermal Preparation, Formation Mechanism and Photocatalytic Activity for H2 Production. *Chem. Commun.* **2012**, *48* (58), 7301. https://doi.org/10.1039/c2cc33211f.
(133) Liu, J.; Chen, G.; Li, Z.; Zhang, Z. Hydrothermal Synthesis and Photocatalytic Properties of ATaO3ATaO3 and ANbO3ANbO3 (A=NaA=Na and K). *Int. J. Hydrog. Energy* **2007**, *32* (13), 2269–2272. https://doi.org/10.1016/j.ijhydene.2006.10.005.
(134) Li, X.; Zang, J. Facile Hydrothermal Synthesis of Sodium Tantalate ($NaTaO_3$) Nanocubes and High Photocatalytic Properties. *J. Phys. Chem. C* **2009**, *113* (45), 19411–19418. https://doi.org/10.1021/jp907334z.
(135) An, L.; Kitta, M.; Iwase, A.; Kudo, A.; Ichikuni, N.; Onishi, H. Photoexcited Electrons Driven by Doping Concentration Gradient: Flux-Prepared $NaTaO_3$ Photocatalysts Doped with Strontium Cations. *ACS Catal.* **2018**, *8* (10), 9334–9341. https://doi.org/10.1021/acscatal.8b02437.

(136) Xu, J.; Xue, D.; Yan, C. Chemical Synthesis of NaTaO3 Powder at Low-Temperature. *Mater. Lett.* **2005**, *59* (23), 2920–2922. https://doi.org/10.1016/j.matlet.2005.04.043.
(137) Chaneliere, C.; Autran, J. L.; Devine, R. A. B.; Balland, B. Tantalum Pentoxide (Ta2O5) Thin Films for Advanced Dielectric Applications. *Mater. Sci. Eng. R Rep.* **1998**, *22* (6), 269–322. https://doi.org/10.1016/S0927-796X(97)00023-5.
(138) Gröhn, A. J.; Pratsinis, S. E.; Sánchez-Ferrer, A.; Mezzenga, R.; Wegner, K. Scale-up of Nanoparticle Synthesis by Flame Spray Pyrolysis: The High-Temperature Particle Residence Time. *Ind. Eng. Chem. Res.* **2014**, *53* (26), 10734–10742. https://doi.org/10.1021/ie501709s.
(139) Ding, S.; Chen, H.-A.; Mekasuwandumrong, O.; Hülsey, M. J.; Fu, X.; He, Q.; Panpranot, J.; Yang, C.-M.; Yan, N. High-Temperature Flame Spray Pyrolysis Induced Stabilization of Pt Single-Atom Catalysts. *Appl. Catal. B Environ.* **2021**, *281*, 119471. https://doi.org/10.1016/j.apcatb.2020.119471.
(140) Guinebretière, R. *X-Ray Diffraction by Polycrystalline Materials: Guinebretière/X-Ray*; ISTE: London, UK, 2007. https://doi.org/10.1002/9780470612408.
(141) Hammond, C. X-Ray Diffraction of Polycrystalline Materials. In *The Basics of Crystallography and Diffraction*; Oxford University PressOxford, 2015; pp 252–282. https://doi.org/10.1093/acprof:oso/9780198738671.003.0010.
(142) Gopalakrishna, G.; Ramchander, R. B. Magnification in X-Ray Diffraction Patterns of Polycrystalline Materials. *Int. J. Rock Mech. Min. Sci. Geomech. Abstr.* **1973**, *10* (4), 285–289. https://doi.org/10.1016/0148-9062(73)90039-9.
(143) Bunaciu, A. A.; Udriştioiu, E. G.; Aboul-Enein, H. Y. X-Ray Diffraction: Instrumentation and Applications. *Crit. Rev. Anal. Chem.* **2015**, *45* (4), 289–299. https://doi.org/10.1080/10408347.2014.949616.
(144) Patterson, A. L. The Scherrer Formula for X-Ray Particle Size Determination. *Phys. Rev.* **1939**, *56* (10), 978–982. https://doi.org/10.1103/PhysRev.56.978.
(145) Holzwarth, U.; Gibson, N. The Scherrer Equation versus the "Debye-Scherrer Equation." *Nat. Nanotechnol.* **2011**, *6* (9), 534–534. https://doi.org/10.1038/nnano.2011.145.
(146) McCusker, L. B.; Von Dreele, R. B.; Cox, D. E.; Louër, D.; Scardi, P. Rietveld Refinement Guidelines. *J. Appl. Crystallogr.* **1999**, *32* (1), 36–50. https://doi.org/10.1107/S0021889898009856.
(147) Einstein, A. Über einen die Erzeugung und Verwandlung des Lichtes betreffenden heuristischen Gesichtspunkt. *Ann. Phys.* **1905**, *322* (6), 132–148. https://doi.org/10.1002/andp.19053220607.
(148) Brunauer, S.; Emmett, P. H.; Teller, E. Adsorption of Gases in Multimolecular Layers. *J. Am. Chem. Soc.* **1938**, *60* (2), 309–319. https://doi.org/10.1021/ja01269a023.
(149) Medeiros-Costa, I. C.; Laroche, C.; Pérez-Pellitero, J.; Coasne, B. Characterization of Hierarchical Zeolites: Combining Adsorption/Intrusion, Electron Microscopy, Diffraction and Spectroscopic Techniques. *Microporous Mesoporous Mater.* **2019**, *287*, 167–176. https://doi.org/10.1016/j.micromeso.2019.05.057.
(150) Raman, C. V.; Krishnan, K. S. A New Type of Secondary Radiation. *Nature* **1928**, *121* (3048), 501–502. https://doi.org/10.1038/121501c0.
(151) Smith, E.; Dent, G. *Modern Raman Spectroscopy – A Practical Approach*, 1st ed.; Wiley, 2004. https://doi.org/10.1002/0470011831.

(152) *Modern Techniques in Applied Molecular Spectroscopy*; Mirabella, F. M., Ed.; Techniques in analytical chemistry series; Wiley: New York, 1998.
(153) Alivisatos, A. P. Semiconductor Clusters, Nanocrystals, and Quantum Dots. *Science* **1996**, *271* (5251), 933–937. https://doi.org/10.1126/science.271.5251.933.
(154) Kubelka, P.; Munk, F. An Article on Optics of Paint Layers. *Fuer Tekn Phys.* **1931**, *12*, 593–609.
(155) Bock, S.; Kijatkin, C.; Berben, D.; Imlau, M. Absorption and Remission Characterization of Pure, Dielectric (Nano-)Powders Using Diffuse Reflectance Spectroscopy: An End-To-End Instruction. *Appl. Sci.* **2019**, *9* (22), 4933. https://doi.org/10.3390/app9224933.
(156) Tauc, J.; Grigorovici, R.; Vancu, A. Optical Properties and Electronic Structure of Amorphous Germanium. *Phys. Status Solidi B* **1966**, *15* (2), 627–637. https://doi.org/10.1002/pssb.19660150224.
(157) Makuła, P.; Pacia, M.; Macyk, W. How To Correctly Determine the Band Gap Energy of Modified Semiconductor Photocatalysts Based on UV–Vis Spectra. *J. Phys. Chem. Lett.* **2018**, *9* (23), 6814–6817. https://doi.org/10.1021/acs.jpclett.8b02892.
(158) *Electron Paramagnetic Resonance: A Practitioner's Toolkit*, 1st ed.; Brustolon, M., Giamello, E., Eds.; Wiley, 2009. https://doi.org/10.1002/9780470432235.
(159) Zeeman, P. The Effect of Magnetisation on the Nature of Light Emitted by a Substance. *Nature* **1897**, *55* (1424), 347–347. https://doi.org/10.1038/055347a0.
(160) Planck, M. *The Theory of Heat Radiation*; Dover Publications: New York, 1991.
(161) Eaton, G. R.; Eaton, S. S.; Barr, D. P.; Weber, R. T. *Quantitative EPR*; Springer Vienna: Vienna, 2010. https://doi.org/10.1007/978-3-211-92948-3.
(162) Albrecht, T. R.; Grütter, P.; Horne, D.; Rugar, D. Frequency Modulation Detection Using High- *Q* Cantilevers for Enhanced Force Microscope Sensitivity. *J. Appl. Phys.* **1991**, *69* (2), 668–673. https://doi.org/10.1063/1.347347.
(163) Aasa, R.; Vänngård, T. EPR Signal Intensity and Powder Shapes: A Reexamination. *J. Magn. Reson. 1969* **1975**, *19* (3), 308–315. https://doi.org/10.1016/0022-2364(75)90045-1.
(164) Junk, M. J. N. Electron Paramagnetic Resonance Theory. In *Assessing the Functional Structure of Molecular Transporters by EPR Spectroscopy*; Springer Berlin Heidelberg: Berlin, Heidelberg, 2012; pp 7–52. https://doi.org/10.1007/978-3-642-25135-1_2.
(165) Peisach, J.; Blumberg, W. E. Structural Implications Derived from the Analysis of Electron Paramagnetic Resonance Spectra of Natural and Artificial Copper Proteins. *Arch. Biochem. Biophys.* **1974**, *165* (2), 691–708. https://doi.org/10.1016/0003-9861(74)90298-7.
(166) Lada, Z. G.; Sanakis, Y.; Raptopoulou, C. P.; Psycharis, V.; Perlepes, S. P.; Mitrikas, G. Probing the Electronic Structure of a Copper(II) Complex by CW- and Pulse-EPR Spectroscopy. *Dalton Trans.* **2017**, *46* (26), 8458–8475. https://doi.org/10.1039/C7DT01785E.
(167) Walger, E.; Marlin, N.; Molton, F.; Mortha, G. Study of the Direct Red 81 Dye/Copper(II)-Phenanthroline System. *Molecules* **2018**, *23* (2), 242. https://doi.org/10.3390/molecules23020242.
(168) Stoll, S.; Schweiger, A. EasySpin, a Comprehensive Software Package for Spectral Simulation and Analysis in EPR. *J. Magn. Reson.* **2006**, *178* (1), 42–55. https://doi.org/10.1016/j.jmr.2005.08.013.

(169) Prasai, D.; Tuberquia, J. C.; Harl, R. R.; Jennings, G. K.; Bolotin, K. I. Graphene: Corrosion-Inhibiting Coating. *ACS Nano* **2012**, *6* (2), 1102–1108. https://doi.org/10.1021/nn203507y.
(170) Jüttner, K. Electrochemical Impedance Spectroscopy (EIS) of Corrosion Processes on Inhomogeneous Surfaces. *Electrochimica Acta* **1990**, *35* (10), 1501–1508. https://doi.org/10.1016/0013-4686(90)80004-8.
(171) Mai, L.-Q.; Minhas-Khan, A.; Tian, X.; Hercule, K. M.; Zhao, Y.-L.; Lin, X.; Xu, X. Synergistic Interaction between Redox-Active Electrolyte and Binder-Free Functionalized Carbon for Ultrahigh Supercapacitor Performance. *Nat. Commun.* **2013**, *4* (1), 2923. https://doi.org/10.1038/ncomms3923.
(172) Yum, J.-H.; Baranoff, E.; Kessler, F.; Moehl, T.; Ahmad, S.; Bessho, T.; Marchioro, A.; Ghadiri, E.; Moser, J.-E.; Yi, C.; Nazeeruddin, Md. K.; Grätzel, M. A Cobalt Complex Redox Shuttle for Dye-Sensitized Solar Cells with High Open-Circuit Potentials. *Nat. Commun.* **2012**, *3* (1), 631. https://doi.org/10.1038/ncomms1655.
(173) Frackowiak, E.; Béguin, F. Carbon Materials for the Electrochemical Storage of Energy in Capacitors. *Carbon* **2001**, *39* (6), 937–950. https://doi.org/10.1016/S0008-6223(00)00183-4.
(174) Taberna, P. L.; Simon, P.; Fauvarque, J. F. Electrochemical Characteristics and Impedance Spectroscopy Studies of Carbon-Carbon Supercapacitors. *J. Electrochem. Soc.* **2003**, *150* (3), A292. https://doi.org/10.1149/1.1543948.
(175) Wang, Q.; Moser, J.-E.; Grätzel, M. Electrochemical Impedance Spectroscopic Analysis of Dye-Sensitized Solar Cells. *J. Phys. Chem. B* **2005**, *109* (31), 14945–14953. https://doi.org/10.1021/jp052768h.
(176) Grieshaber, D.; MacKenzie, R.; Vörös, J.; Reimhult, E. Electrochemical Biosensors - Sensor Principles and Architectures. *Sensors* **2008**, *8* (3), 1400–1458. https://doi.org/10.3390/s80314000.
(177) Katz, E.; Willner, I. Probing Biomolecular Interactions at Conductive and Semiconductive Surfaces by Impedance Spectroscopy: Routes to Impedimetric Immunosensors, DNA-Sensors, and Enzyme Biosensors. *Electroanalysis* **2003**, *15* (11), 913–947. https://doi.org/10.1002/elan.200390114.
(178) Orazem, M. E.; Tribollet, B. *Electrochemical Impedance Spectroscopy: Orazem/Electrochemical*; John Wiley & Sons, Inc.: Hoboken, NJ, USA, 2008. https://doi.org/10.1002/9780470381588.
(179) *Impedance Spectroscopy: Theory, Experiment, and Applications*, 1st ed.; Barsoukov, E., Macdonald, J. R., Eds.; Wiley, 2005. https://doi.org/10.1002/0471716243.
(180) Chang, B.-Y.; Park, S.-M. Electrochemical Impedance Spectroscopy. *Annu. Rev. Anal. Chem.* **2010**, *3* (1), 207–229. https://doi.org/10.1146/annurev.anchem.012809.102211.
(181) Macdonald, J. R. Impedance Spectroscopy. *Ann. Biomed. Eng.* **1992**, *20* (3), 289–305. https://doi.org/10.1007/BF02368532.
(182) Nicholson, R. S. Theory and Application of Cyclic Voltammetry for Measurement of Electrode Reaction Kinetics. *Anal. Chem.* **1965**, *37* (11), 1351–1355. https://doi.org/10.1021/ac60230a016.
(183) Bredar, A. R. C.; Chown, A. L.; Burton, A. R.; Farnum, B. H. Electrochemical Impedance Spectroscopy of Metal Oxide Electrodes for Energy Applications. *ACS Appl. Energy Mater.* **2020**, *3* (1), 66–98. https://doi.org/10.1021/acsaem.9b01965.

(184) Mayrhofer, K. J. J.; Strmcnik, D.; Blizanac, B. B.; Stamenkovic, V.; Arenz, M.; Markovic, N. M. Measurement of Oxygen Reduction Activities via the Rotating Disc Electrode Method: From Pt Model Surfaces to Carbon-Supported High Surface Area Catalysts. *Electrochimica Acta* **2008**, *53* (7), 3181–3188. https://doi.org/10.1016/j.electacta.2007.11.057.
(185) Panagiotopoulou, P. Effect of Morphological Characteristics of TiO2-Supported Noble Metal Catalysts on Their Activity for the Water?Gas Shift Reaction. *J. Catal.* **2004**, *225* (2), 327–336. https://doi.org/10.1016/j.jcat.2004.04.030.
(186) Molina Concha, B.; Chatenet, M. Direct Oxidation of Sodium Borohydride on Pt, Ag and Alloyed Pt–Ag Electrodes in Basic Media. Part I: Bulk Electrodes. *Electrochimica Acta* **2009**, *54* (26), 6119–6129. https://doi.org/10.1016/j.electacta.2009.05.027.
(187) Simpson, R.; White, R. G.; Watts, J. F.; Baker, M. A. XPS Investigation of Monatomic and Cluster Argon Ion Sputtering of Tantalum Pentoxide. *Appl. Surf. Sci.* **2017**, *405*, 79–87. https://doi.org/10.1016/j.apsusc.2017.02.006.
(188) Cui, E.; Hou, G.; Chen, X.; Zhang, F.; Deng, Y.; Yu, G.; Li, B.; Wu, Y. In-Situ Hydrothermal Fabrication of Sr2FeTaO6/NaTaO3 Heterojunction Photocatalyst Aimed at the Effective Promotion of Electron-Hole Separation and Visible-Light Absorption. *Appl. Catal. B Environ.* **2019**, *241*, 52–65. https://doi.org/10.1016/j.apcatb.2018.09.006.
(189) Swadźba-Kwaśny, M.; Chancelier, L.; Ng, S.; Manyar, H. G.; Hardacre, C.; Nockemann, P. Facile in Situ Synthesis of Nanofluids Based on Ionic Liquids and Copper Oxide Clusters and Nanoparticles. *Dalton Trans* **2012**, *41* (1), 219–227. https://doi.org/10.1039/C1DT11578B.
(190) Joseph, C.; Bourson, P.; Fontana, M. D. Amorphous to Crystalline Transformation in Ta2O5 Studied by Raman Spectroscopy: Amorphous to Crystalline Transformation in Ta2O5 Studied by Raman Spectroscopy. *J. Raman Spectrosc.* **2012**, *43* (8), 1146–1150. https://doi.org/10.1002/jrs.3142.
(191) Dobal, P. S.; Katiyar, R. S.; Jiang, Y.; Guo, R.; Bhalla, A. S. Raman Scattering Study of a Phase Transition in Tantalum Pentoxide. *J. Raman Spectrosc.* **2000**, *31* (12), 1061–1065. https://doi.org/10.1002/1097-4555(200012)31:12<1061::AID-JRS644>3.0.CO;2-G.
(192) An, L.; Park, Y.; Sohn, Y.; Onishi, H. Effect of Etching on Electron–Hole Recombination in Sr-Doped $NaTaO_3$ Photocatalysts. *J. Phys. Chem. C* **2015**, *119* (51), 28440–28447. https://doi.org/10.1021/acs.jpcc.5b09638.
(193) Teixeira, N. G.; Dias, A.; Moreira, R. L. Raman Scattering Study of the High Temperature Phase Transitions of NaTaO3. *J. Eur. Ceram. Soc.* **2007**, *27* (13–15), 3683–3686. https://doi.org/10.1016/j.jeurceramsoc.2007.02.015.
(194) Schwan, J.; Ulrich, S.; Batori, V.; Ehrhardt, H.; Silva, S. R. P. Raman Spectroscopy on Amorphous Carbon Films. *J. Appl. Phys.* **1996**, *80* (1), 440–447. https://doi.org/10.1063/1.362745.
(195) Tauster, S. J.; Fung, S. C.; Garten, R. L. Strong Metal-Support Interactions. Group 8 Noble Metals Supported on Titanium Dioxide. *J. Am. Chem. Soc.* **1978**, *100* (1), 170–175. https://doi.org/10.1021/ja00469a029.
(196) Tauc, J.; Grigorovici, R.; Vancu, A. Optical Properties and Electronic Structure of Amorphous Germanium. *Phys. Status Solidi B* **1966**, *15* (2), 627–637. https://doi.org/10.1002/pssb.19660150224.
(197) Knausenberger, W. H.; Tauber, R. N. Selected Properties of Pyrolytic Ta[Sub 2]O[Sub 5] Films. *J. Electrochem. Soc.* **1973**, *120* (7), 927. https://doi.org/10.1149/1.2403602.

(198) Grigoropoulou, G.; Christoforidis, K. C.; Louloudi, M.; Deligiannakis, Y. Structure-Catalytic Function Relationship of SiO_2 -Immobilized Mononuclear Cu Complexes: An EPR Study. *Langmuir* **2007**, *23* (20), 10407–10418. https://doi.org/10.1021/la700815d.
(199) Zois, D.; Vartzouma, C.; Deligiannakis, Y.; Hadjiliadis, N.; Casella, L.; Monzani, E.; Louloudi, M. Active Catalytic Centers in Silica-Supported Cu(II) and Mn(II) Biomimetic Complexes: Correlation between Catalytic and EPR Data. *J. Mol. Catal. Chem.* **2007**, *261* (2), 306–317. https://doi.org/10.1016/j.molcata.2006.11.023.
(200) Bencini, A.; Bertini, I.; Gatteschi, D.; Scozzafava, A. Single-Crystal ESR Spectra of Copper(II) Complexes with Geometries Intermediate between a Square Pyramid and a Trigonal Bipyramid. *Inorg. Chem.* **1978**, *17* (11), 3194–3197. https://doi.org/10.1021/ic50189a047.
(201) Bencini, A.; Gatteschi, D. *Electron Paramagnetic Resonance of Exchange Coupled Systems*; Springer Berlin Heidelberg: Berlin, Heidelberg, 1990. https://doi.org/10.1007/978-3-642-74599-7.
(202) Eaton, S. S.; More, K. M.; Sawant, B. M.; Eaton, G. R. Use of the ESR Half-Field Transition to Determine the Interspin Distance and the Orientation of the Interspin Vector in Systems with Two Unpaired Electrons. *J. Am. Chem. Soc.* **1983**, *105* (22), 6560–6567. https://doi.org/10.1021/ja00360a005.
(203) Xu, L.; Li, C.; Shi, W.; Guan, J.; Sun, Z. Visible Light-Response NaTa1−xCuxO3 Photocatalysts for Hydrogen Production from Methanol Aqueous Solution. *J. Mol. Catal. Chem.* **2012**, *360*, 42–47. https://doi.org/10.1016/j.molcata.2012.04.006.
(204) Husin, H.; Chen, H.-M.; Su, W.-N.; Pan, C.-J.; Chuang, W.-T.; Sheu, H.-S.; Hwang, B.-J. Green Fabrication of La-Doped NaTaO3 via H2O2 Assisted Sol–Gel Route for Photocatalytic Hydrogen Production. *Appl. Catal. B Environ.* **2011**, *102* (1–2), 343–351. https://doi.org/10.1016/j.apcatb.2010.12.024.
(205) Iwase, A.; Kato, H.; Okutomi, H.; Kudo, A. Formation of Surface Nano-Step Structures and Improvement of Photocatalytic Activities of $NaTaO_3$ by Doping of Alkaline Earth Metal Ions. *Chem. Lett.* **2004**, *33* (10), 1260–1261. https://doi.org/10.1246/cl.2004.1260.